Metallorganic Chemical Vapor Deposition of Lead Oxide and Lead Titanate

by

Warren Charles Hendricks

Thesis submitted to the Faculty of the

Virginia Polytechnic Institute & State University

in partial fulfillment of the requirements for the degree of

Master of Science

in

Materials Science and Engineering

APPROVED:

S. B. Desu, Chairman

A. O. Aning

G. Q. Lu

September, 1993

Blacksburg, Virginia

c.2

LD
5655
V855
1993
H462
c.2

Metallorganic Chemical Vapor Deposition of Lead Oxide and Lead Titanate

by

Warren Charles Hendricks

S. B. Desu, Chairman

Materials Science and Engineering

(ABSTRACT)

The purpose of this study was two-fold: firstly, the MOCVD deposition behavior of $Pb(thd)_2$ was studied in detail and a one-dimensional kinetic model was proposed to successfully predict the effect of processing conditions on the deposition rate profile for PbO. Assuming the surface reaction is the rate-limiting step in the process, the effective activation energy for the process, E_a, was found to be 82 kJ/mol while the preexponential rate constant was found to be 33 g/cm^2/min (0.15 mol/cm^2/min). The process was found to consistently produce a combination of the high temperature, orthorhombic modification of lead monoxide with randomly oriented plates of tetragonal lead monoxide. TEM electron diffraction was used to investigate the crystal orientation of the individual plates which was found to be in the plane normal to the <201> zone.

Secondly, the deposition behavior of $PbTiO_3$ and the resulting film structure and properties were investigated. $Pb(thd)_2$ was used in conjunction with titanium ethoxide ($Ti(OEt)_4$) as a titanium source. Stoichiometric lead titanate films which were found to be smooth, specular and transparent, and well-adhered were deposited on a variety of substrates by careful control of the experimental conditions. Film structure, composition, and thickness were studied and correlated to changes in various experimental parameters. Additionally, a high temperature regime at which the film stoichiometry is relatively insensitive to experimental conditions was found to occur. The effects of post-annealing on the as-deposited films including compositional changes, morphological changes and crystal structure was also studied. Some problems were obtained with film peeling on the

ruthenium oxide (RuO_2)-coated substrates which could be alleviated somewhat by the use of (100) oriented silicon wafer rather than (111) oriented silicon; a possible mechanism to explain this behavior is also suggested. Optical properties were obtained using UV-VIS-NIR transmission and reflectance spectroscopy; the ferroelectric hysteresis behavior of the films was observed using standard RT-66 A test equipment.

ACKNOWLEDGEMENTS

Dr. Chien H. Peng deserves special acknowledgements for working closely with me during the initial stages of setting up the CVD equipment and troubleshooting the equipment once it was up and running. He was also extremely helpful in providing theoretical discussion as well as instrumental in helping me interpret the optical data. I am thankful for Dr. Ching Y. Tsai who was responsible for the FORTRAN computer code used in the PbO deposition rate simulation program (Appendix A) which required many hours of help on his part. Jie Si and Chen C. Li deserve great recognition for their many hours spent performing EDS analysis of the lead titanate samples. I would like to give special thanks to Steve Mc Cartney and Chien Chiu and for help in taking the SEM photographs and in interpreting the TEM electron diffraction patterns. I would like to thank Dilip Vijay, Jimmy Xing, and Wei Pan for preparing the ruthenium oxide electrode material used in this study as well as sputtering top electrodes for the determination of electrical properties. Ashraf Khan deserves my thanks for help in using the UV-VIS-NIR spectrophotometer and also In Yoo for his help with the electrical measurements. I would also like to thank and acknowledge Gang Chen and Jhewn-Kuang Chen for their help in the TEM work and Prof. G. V. Gibbs for the use of his program, XTALDRAW, for generating the crystal structure images. Finally, I am indebted to my faculty advisor, Dr. Seshu B. Desu, for providing hours of helpful guidance along the way, along with each of the other members of the thin film lab for providing helpful and interesting discussions.

TABLE OF CONTENTS

Chapter 1: Introduction

1.1 Chemical Vapor Deposition (CVD) Process

1.1.1 Gas Transport

1.1.2 Thermodynamics

1.1.3 Growth Kinetics

1.1.4 Metallorganic CVD (MOCVD) and Other Variations

1.2 Properties and Applications of Lead Oxide (PbO) Thin Films

1.3 Background Information on Lead Titanate ($PbTiO_3$)

1.3.1 Properties and Applications of Lead Titanate

1.3.2 Brief Literature Review of MOCVD Lead Titanate

1.4 Objectives of Research

Chapter 2: Kinetics and Growth Behavior of the MOCVD of PbO

2.1 Introduction

2.2 Precursor Properties and Selection

2.3 MOCVD Experimental Procedure

2.4 Discussion and Results

2.4.1 FEM Modeling of the MOCVD Process

2.4.2 Determining Precursor Partial Pressures

2.4.3 Comparison of Experimental Data and Simulated Behavior

2.4.4 Crystal Structure and Morphology

2.4.4.1 X-Ray Diffraction Study

2.4.4.2 Surface Morphology using SEM

2.4.4.3 Transmission Electron Microscopy (TEM) Study

2.5 Summary and Conclusions

Chapter 3: Metallorganic Chemical Vapor Deposition (MOCVD) of $PbTiO_3$

3.1 Introduction

3.2 Equipment and Experimental Procedure

3.2.1 Precursors

3.2.2 Substrate Materials

3.2.3 MOCVD Equipment

3.2.4 MOCVD Experimental Procedure

3.3 Results and Discussion

3.3.1 Effect of Process Parameters on Film Structure, Thickness and Composition

3.3.1.1 Thickness, Composition and XRD Results

3.3.1.2 Study of Surface Morphology Using SEM

3.3.1.3 Use of High Temperature Deposition Regime for Improved Composition Control

3.3.2 Effect of Post-Annealing Heat Treatment

3.3.2.1 Crystal Structure (XRD)

3.3.2.2 Surface Morphology (SEM)

3.3.2.3 Composition (EDS)

3.3.3 Stability of RuO_2-coated Substrates During Deposition Process

3.3.3.1 Morphology Using Optical Microscopy

3.3.3.2 Influence of Silicon Substrate Orientation

3.3.4 Optical Properties Using UV-VIS-NIR Spectrometry

3.3.5 Ferroelectric Properties

3.4 Summary and Conclusions

Appendix A: FORTRAN Code for Simulation of PbO Deposition Process

Chapter 3: Metallorganic Chemical Vapor Deposition (MOCVD) of $PbTiO_3$

3.1 Introduction

3.2 Equipment and Experimental Procedure

3.2.1 Precursors

3.2.2 Substrate Materials

3.2.3 MOCVD Equipment

3.2.4 MOCVD Experimental Procedure

3.3 Results and Discussion

3.3.1 Effect of Process Parameters on Film Structure, Thickness and Composition

3.3.1.1 Thickness, Composition and XRD Results

3.3.1.2 Study of Surface Morphology Using SEM

3.3.1.3 Use of High Temperature Deposition Regime for Improved Composition Control

3.3.2 Effect of Post-Annealing Heat Treatment

3.3.2.1 Crystal Structure (XRD)

3.3.2.2 Surface Morphology (SEM)

3.3.2.3 Composition (EDS)

3.3.3 Stability of RuO_2-coated Substrates During Deposition Process

3.3.3.1 Morphology Using Optical Microscopy

3.3.3.2 Influence of Silicon Substrate Orientation

3.3.4 Optical Properties Using UV-VIS-NIR Spectrometry

3.3.5 Ferroelectric Properties

3.4 Summary and Conclusions

Appendix A: FORTRAN Code for Simulation of PbO Deposition Process

References

Additional Bibliography

Vita

FIGURE LIST

Figure 1.1: (a) Unit cell of the perovskite phase of $PbTiO_3$; (b) Tetragonality (c/a) for the perovskite $PbTiO_3$ unit cell

Figure 2.1: Structure of the $Pb(thd)_2$ molecule

Figure 2.2: Vapor pressure of $Pb(thd)_2$ vs. temperature from which the enthalpies of sublimation and evaporation were calculated

Figure 2.3: MOCVD Apparatus for the deposition of PbO from $Pb(thd)_2$

Figure 2.4: Temperature profiles in the reactor for T_d = 550 ^{0}C, 500 ^{0}C, and 450 ^{0}C

Figure 2.5: Effect of deposition temperature on deposition rate for experimental data (points) and simulated data (curves) for various reactor positions

Figure 2.6: Effect of total flow rate on deposition rate for experimental data (points) and simulated data (curves) for various reactor positions

Figure 2.7: Effect of total pressure on deposition rate for experimental data (points) and simulated data (curves) for various reactor positions

Figure 2.8: XRD results for PbO on polycrystalline alumina deposited at T_d = 450 ^{0}C

Figure 2.9: XRD results for PbO on polycrystalline alumina deposited at T_d = 500 ^{0}C

Figure 2.10: XRD results for PbO on polycrystalline alumina deposited at T_d = 550 ^{0}C

Figure 2.11: XRD results for PbO on sapphire deposited at T_d = 550 ^{0}C

Figure 2.12: XRD results of PbO from Fig. 2.11 before and after 2 hr. anneal at 450 ^{0}C

Figure 2.13: SEM micrographs of PbO on sapphire for four different positions of the same run shown in Fig. 2.11

Figure 2.14: Simulated crystal structure of α-PbO looking down the a-axis

Figure 2.15: (a) Bright-field TEM micrograph of α-PbO platelets; (b) SADP of <201> zone of same platelet viewed normal to the plane of platelet; (c) Dark-field micrograph

Figure 2.16: SADP of <100> zone of platelet in Fig. 2.15 obtained by rotating the stage

Figure 2.17: Simulated crystal structure of α-PbO looking in the direction of the <201> zone axis

Figure 3.1: MOCVD apparatus and thermal profile for the deposition of $PbTiO_3$

Figure 3.2: Variation in the composition profile with the lead bubbler temperature; the titanium bubbler temperature is fixed at 98 ^{0}C

Figure 3.3: Variation in the thickness profile with the lead bubbler temperature; the titanium bubbler temperature is fixed at 98 ^{0}C

Figure 3.4: XRD pattern for $T_{b,\ Pb}$ = 136 ^{0}C in Figs. 3.2 and 3.3

Figure 3.5: XRD pattern for $T_{b,\ Pb}$ = 140 ^{0}C in Figs. 3.2 and 3.3

Figure 3.6: Variation in the composition profile with the titanium bubbler temperature; the lead bubbler temperature is fixed at 140 ^{0}C

Figure 3.7: Variation in the thickness profile with the titanium bubbler temperature; the lead bubbler temperature is fixed at 140 ^{0}C

Figure 3.8: XRD pattern for $T_{b,\ Ti}$ = 110 ^{0}C in Figs. 3.6 and 3.7

Figure 3.9: XRD pattern for $T_{b,\ Ti}$ = 112 ^{0}C in Figs. 3.6 and 3.7

Figure 3.10: XRD pattern for $T_{b,\ Ti}$ = 114 ^{0}C in Figs. 3.6 and 3.7

Figure 3.11: XRD pattern for $T_{b,\ Ti}$ = 116 ^{0}C in Figs. 3.6 and 3.7

Figure 3.12: Variation in the composition profile with the deposition pressure

Figure 3.13: Variation in the thickness profile with the deposition pressure

Figure 3.14: XRD pattern for p = 4 torr in Figs. 3.12 and 3.13

Figure 3.15: XRD pattern for p = 8 torr in Figs. 3.12 and 3.13

Figure 3.16: SEM micrographs of $PbTiO_3$ on sapphire for T_d = 550 ^{0}C

Figure 3.17: SEM micrographs of $PbTiO_3$ on RuO_2 for T_d = 550 ^{0}C

Figure 3.18: Variation in the composition profile at the high temperature regime

Figure 3.19: Variation in the thickness profile at the high temperature regime

Figure 3.20: XRD pattern for $T_{b,\ Ti}$ = 115 ^{0}C, $T_{b,\ Pb}$ = 150 ^{0}C deposited at T_d = 650 ^{0}C on sapphire

Figure 3.21: XRD pattern for $T_{b,\ Ti}$ = 120 ^{0}C, $T_{b,\ Pb}$ = 150 ^{0}C deposited at T_d = 650 ^{0}C on RuO_2 and Pt

Figure 3.22: XRD pattern for $T_{b,\ Ti}$ = 120 ^{0}C, $T_{b,\ Pb}$ = 150 ^{0}C deposited at T_d = 650 ^{0}C on RuO_2

Figure 3.23: SEM micrograph of $PbTiO_3$ films deposited on Pt at 650 ^{0}C

Figure 3.24: (a) Specular transmittance spectrum and (b) specular reflectance spectrum for $PbTiO_3$ deposited at 650 ^{0}C

Figure 3.25: Vapor pressure of PbO over PbO and over $PbTiO_3$

Figure 3.26: SEM micrographs of $PbTiO_3$ deposited on Pt at 500 ^{0}C in cross-section for (a) as-deposited film; (b) annealed at 500 ^{0}C for 1 hr. and (c) annealed at 600 ^{0}C for 1 hr.

Figure 3.27: SEM micrographs of $PbTiO_3$ deposited on Pt at 500 ^{0}C for (a) as-deposited film; (b) annealed at 500 ^{0}C for 1 hr. and (c) annealed at 600 ^{0}C for 1 hr.

Figure 3.28: SEM micrographs of $PbTiO_3$ deposited on RuO_2 at 550 ^{0}C and annealed at 600 ^{0}C for 1 hr.

Figure 3.29: Effect of post-deposition annealing on composition of Pb-rich $PbTiO_3$

Figure 3.30: XRD of $PbTiO_3$ on RuO_2 at 550 ^{0}C (As Deposited)

Figure 3.31: XRD of $PbTiO_3$ on RuO_2 at 550 ^{0}C (After 600 ^{0}C Anneal)

Figure 3.32: XRD of $PbTiO_3$ on RuO_2 at 550 ^{0}C (As Deposited)

Figure 3.33: XRD of $PbTiO_3$ on RuO_2 at 550 ^{0}C (After 600 ^{0}C Anneal)

Figure 3.34: Optical micrograph (reflected polarized light) of (a) RuO_2 on (111) Si after being deposited with $PbTiO_3$ film at 550 ^{0}C and (b) RuO_2 on (111) Si after being annealed in 6 torr of N_2 at 600 ^{0}C

Figure 3.35: Optical transmission and reflectance spectra for $PbTiO_3$ film deposited at 550 ^{0}C on sapphire

Figure 3.36: Optical properties of film determined from results in Fig. 3.35

Figure 3.37: Ferroelectric hysteresis loop for $PbTiO_3$ on platinum deposited at 550 ^{0}C

TABLE LIST

Table 2.1: $Pb(thd)_2$ Partial Pressures

Table 3.1: Optimum $PbTiO_3$ MOCVD Parameters for $T_d = 550\ ^0C$

CHAPTER 1: INTRODUCTION

1.1 The Chemical Vapor Deposition (CVD) Process

Chemical Vapor Deposition (CVD) is a process for synthesizing thin solid films on a solid substrate material by the adsorption and chemical reaction of precursor species from the gas phase onto the surface of the material to be coated. CVD is an indispensable process in the microelectronic industry for the production of high quality semiconductor, insulating and metallic thin films for a variety of applications [1]. CVD films find uses in applications as diverse as high quality epitaxial semiconductor thin films for Si bipolar and MOS transistors to protective coatings for rocket engines and nuclear reactor components [1].

Some of the advantages that make the CVD process superior to other thin film deposition techniques include flexible composition control, excellent step coverage for complex thin film transistor geometry, and the ease of applying the process to large-scale industrial processing [2]. Although the physical equipment necessary to perform CVD is relatively simple compared to other deposition techniques, understanding the CVD process is complicated considerably due to the complex interaction among the many individual processes occurring in the overall process.

A simple system for performing thermal CVD (i. e., CVD in which the reaction of the precursor is initiated by the relatively high temperature in the reactor) may be considered as consisting of four main regions according to their respective functions. The first region consists of the equipment which is used for the storage of precursors and the generation of precursor vapors. The second region is defined as the vapor transport region and consists of the tubes for transporting the precursor vapors and possibly the related

heating arrangements to prevent the precursor vapors from condensing before reaching the reactor. Finally these vapors will enter the heated zone of the reactor, the third zone, where the actual CVD reaction occurs. The fourth zone consists of the vacuum pump and/or cold trap and associated equipment and hardware for removing the by-products of the CVD reaction and any excess precursor that has not fully reacted. The successfully reproducible CVD process requires that each of these constituent processes be controlled simultaneously; the processes and reactions which occur in the first three zone leading up to the deposition process are especially important. Even assuming we can measure and control the composition and flow rate of the gas mixture entering the reactor, a mathematical model concerned only with the CVD process occurring in the reactor must consider such complications as gas transport phenomena (fluid flow), heat transfer, diffusion of multiple species in both the gaseous and solid states, as well as the thermodynamics and chemical kinetics of various species in the gas phase as well as in the solid state. Generally, the three most important considerations in characterizing the behavior of a given CVD system are gas transport phenomena, thermodynamics, and growth kinetics. These are considered in each of the three sections that follow.

1.1.1 Gas Transport

Gas transport involves the movement of gaseous precursor species through the reactor. Since the deposition rate at a given location on a substrate is highly dependent on the flux of reactant molecules which impinge on the surface at that location, the careful control of the gas transport behavior of the system is very important in insuring a uniform deposition rate as well as in maximizing the overall deposition rate efficiency.

In most CVD reactors it is desirable to be in the viscous flow regime as opposed to the turbulent regime in order to ensure a uniform, time independent flux of precursor molecules to the substrate surface. This is usually easily obtained under the normal operating conditions of most CVD reactions. Generally, viscous flow can be obtained for systems with Reynolds numbers below 2100 [3].Most hot-walled reactors are cylindrical in shape with the flow parallel to the long axis; for such a configuration, the Reynolds number, Re, is defined as given below [1]:

$$Re = v_0 D\rho/\eta \quad \text{[Eqn. 1.1]}$$

In the above expression, v_0 represents the average flow velocity, ρ is the gas density, and D is the tube diameter. During viscous flow, a boundary layer which is essentially static develops around the walls of the reactor as well as around any substrate placed in the reactor. Since any gaseous species which approaches the substrate must diffuse through the boundary layer, the thickness of the boundary layer over a given point on a plate (such as at the substrate susceptor) placed inside the reactor affects the flux of precursor species coming to that point. The boundary layer thickness, δ, is given by the following expression valid for a plate placed parallel to the flow of the gas stream [1]:

$$\delta = 5\sqrt{\frac{x\eta}{v_0\rho}} \quad \text{[Eqn. 1.2]}$$

Here x is the distance from the edge of the susceptor where the gas stream first impinges on the plate; it can be seen that the boundary layer thickness increases as the square root of the distance from the leading edge of the susceptor placed parallel to the gas stream. The dependence of the boundary layer on distance is much less severe if the

susceptor is tilted at a small angle so that the near edge of the susceptor is closer to the edge of the wall while the far edge is closer to the center of the reactor tube. Thus most substrate susceptors are tilted somewhat in order to improve the deposition rate uniformity as a function of distance along the length of the reactor.

1.1.2 Thermodynamics

Thermodynamics is useful to consider, especially when deciding whether or not a given reaction is feasible or not. Often, however, the individual chemical reactions and the necessary thermodynamic data for a given system are not available. Even still, thermodynamics can often be used successfully to predict the temperature regime over which a given film structure is stable and whether or not the overall reaction is feasible; but it is often the case that the film growth kinetics generally dominate the process and will consequently determine the ultimate structure.

1.1.3 Growth Kinetics

The area of growth kinetics is probably the most complex part of the CVD process because it depends on such a large number of processes, which may or may not operate independent of one another. In an extremely simplified approach, we can consider the following seven processes to be the necessary minimum in any CVD reaction [1]:

1) Transport of reactant species to the substrate surface through the boundary layer
2) Adsorption of reactant species on the substrate or film surface
3) Atomic and/or molecular diffusion of species on the surface

4) Reaction of precursor species

5) Incorporation of reacted species into lattice

6) Desorption of reaction by-products

7) Transport of by-products away from substrate through the boundary layer

Any given one of these steps may proceed at a rate that limits the rate of any subsequent step. Such a step is termed the rate-limiting or rate-controlling step of the reaction. If step 1 is the rate-limiting step, for example, then the reaction is diffusion controlled; diffusion controlled CVD reactions generally result in poor film structure, often forming large dendrites or columnar microstructures. The rate of steps 2 through 5 are usually not known in any detail and so are generally lumped together under the name of "surface reaction" since each occurs on the surface of the film and/or substrate. A surface reaction controlled process is generally most desirable. If the last two steps involving the removal of by-products does not occur at least as fast as the accumulation of by-products as a result of the surface reaction, then by-products will be left behind in the film resulting in contamination problems. The rate controlling step in any CVD reaction often depends on the experimental conditions which, consequently, must sometimes be adjusted accordingly in order to assure that the surface reaction is controlling the deposition rate.

1.1.4 Metallorganic CVD (MOCVD) and Other Variations

Metallorganic Chemical Vapor Deposition (MOCVD) is fundamentally identical to the traditional CVD process except that the precursors used are volatile metallorganic compounds such as β-diketonates or alkoxides as opposed to liquid metals, metal hydrides or metal halide species which have traditionally been used in CVD. Metallorganic precursors offer the advantages of high vapor at relatively low temperatures compared

with the liquid metal precursors and they are also considerably less toxic than the halide and hydride compounds [2]. Additionally, because there are such a wide variety of ligands which are capable of forming metallorganic compounds, the volatility and decomposition behavior of metallorganic compounds can be customized to suit a specific requirement [15]. Nearly all the recent literature on the CVD of both semiconductors and metal oxides involves the use of metallorganic precursors. In this study, I have chosen to use the metallorganic compounds, lead tetramethylheptadionate ($Pb(thd)_2$) , and titanium ethoxide, $(TiOEt)_4$, as the lead and titanium sources, respectively.

1.2 Properties and Applications of Lead Oxide (PbO)

Lead monoxide is the stable form of lead oxide at ordinary temperatures and pressures and exists in two polymorphs, a high temperature orthorhombic phase known as massicot, yellow lead oxide or β-PbO and a low temperature tetragonal form known as litharge, red lead oxide or α-PbO. The equilibrium transformation temperature varies in the literature but is generally reported to be about 550 ^{0}C [4]. The transformation of the α to the β phase is generally rapid while the reverse transformation of β to α is generally sluggish and requires a catalyst in the form of a water vapor atmosphere or by the introduction of small amounts of impurities in the material [4].

While the emphasis of this study on lead oxide was concerned more with the deposition kinetics and behavior of the material rather than on the physical properties of the resulting films, lead oxide thin films themselves exhibit photoconductive properties over broad regions of the X-ray and visible regions of the electromagnetic spectrum which allows them to find applications in laser optics and color television [5]. Generally these films are deposited by sputtering or evaporation, however, rather than CVD. There are

also reports of the synthesis of bulk single crystal plates by hydrothermal techniques [5, 6, 7].

1.3 Background Information on Lead Titanate ($PbTiO_3$)

1.3.1 Properties and Applications of Lead Titanate

Lead titanate is the parent compound for a large family of materials including PZT, PLZT, etc. which exhibit ferroelectric hysteresis behavior; in other words, the material retains some "spontaneous" electrical polarization after an applied electric field is removed. Each of the previously mentioned materials exists in the perovskite structure with the generic formula of ABO_3. For lead titanate, the unit cell is tetragonal; lead ions are at the corners, or A-sites of the unit cell while oxygen ions are at the faces (see Fig. 1.1). The titanium ion is displaced a small distance from the center of the unit cell in either direction along the c-axis giving rise to two possible stable configurations referred to as the "up" and "down" states. This displacement gives rise to a permanent local dipole moment. The polarization of a given material is defined as the total dipole moment per unit volume and is usually measured in $\mu C/cm^2$.

Since adjacent unit cells are most stable when their polarization directions are the same, individual grains or crystals will generally be composed of several domains or regions which exhibit the same polarization direction. When the material is placed in an electric field, the favorably oriented domains grow at the expense of the less favorably oriented domains, resulting in a net total dipole moment. As the electric field increases in strength the polarization will increase up to the saturated polarization, P_{sat}, at which no further domain growth occurs. Even after the removal of the electric field, these domains

(a)

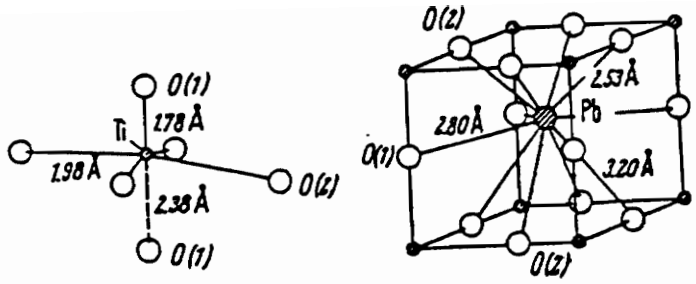

(b)

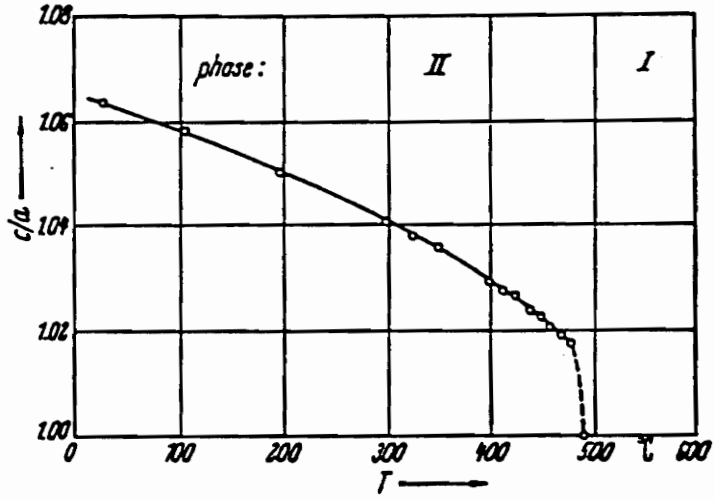

Figure 1.1: (a) Unit cell for perovskite lead titanate; (b) c/a ratio vs. temperature

remain in the material and contribute to the remnant polarization, P_r, defined as the polarization remaining at zero applied field after having poled the material. The magnitude of the field necessary to return the material to the unpolarized state is called the coercive field, E_c. For nonvolatile ferroelectric memory devices such as FRAMs, it is generally desired to have a large remnant polarization, P_r and a low coercive field, E_c [2].

The bistable nature of ferroelectric materials gives rise to many other interesting properties including pyroelectricity, piezoelectricity, and the electro-optic effect [8]. Pyroelectric materials exhibit a proportional change in polarization due to a change in temperature; all ferroelectric materials are also pyroelectric. These materials are useful for detecting infrared radiation in such devices as intruder alarms and thermal imaging [8]. Piezoelectric materials exhibit a linear change in polarization due to a change in applied stress and include the pyroelectric as well as the ferroelectric materials. The number of applications using piezoelectric materials is many, the most common applications being sonic and ultrasonic transducers, actuators, accelerometers and surface acoustic wave (SAW) filters [8, 35].

1.3.2 Brief Literature Review of CVD $PbTiO_3$

$PbTiO_3$ films were the first successful oxide ferroelectric materials to be deposited by CVD by Nakagawa et al. in 1982 [9]. They used conventional chloride precursor, lead chloride and titanium chloride with a reactive atmosphere of oxygen and water vapor. However, the resulting films were found to contain water inclusions and chlorine contamination which resulted in relatively poor ferroelectric properties compared to the sputtered films which were also being synthesized at about the same time. Also, the high temperatures (700 ^{0}C) necessary to vaporize the lead chloride ($PbCl_2$) make this technique

inconvenient. Since that time, many additional studies of the MOCVD of $PbTiO_3$ have been undertaken with the development of suitable metallorganic precursors which have much higher vapor pressures than their chloride counterparts and also readily decompose at the deposition temperatures used without the addition of water vapor.

Nearly all of the recently available literature on the MOCVD of $PbTiO_3$ use the combination of tetraethyl-lead and titanium isopropoxide as precursors [10, 11, 12, 13, and 14]. Several investigators have used $Pb(thd)_2$ [30,31] in place of tetraethyl-lead; lead acetylacetonate has also been used [32]. These precursors are commonly available and have been reported to produce high quality $PbTiO_3$ films. In all cases, however, ferroelectric properties are generally quite poor, probably as a result of high film conductivity. Typical values reported in the literature for pure $PbTiO_3$ are about 0.1 to 0.2 $\mu C/cm^2$ compared to 75 $\mu C/cm^2$ for the bulk ceramic [33]. However, we have chosen to use lead tetramethylheptadionate and titanium ethoxide as precursor sources for reasons that will be explained in section 2.2 and 3.2.1, respectively.

1.4 Objectives of Research

The objective of this study was two-fold: firstly, the MOCVD deposition behavior of PbO from the most promising lead precursor, namely $Pb(thd)_2$, was studied in detail and a one-dimensional kinetic model was proposed to successfully predict the effect of processing conditions on the deposition rate profile for PbO. Such a study provides a foundation for future investigations into the kinetics of more complicated systems such as PZT and doped forms of PZT.

Secondly, the deposition behavior of $PbTiO_3$ and the resulting film structure and properties were investigated. $Pb(thd)_2$ was used in conjunction with titanium ethoxide

($Ti(OEt)_4$) as a titanium source to deposit lead titanate. Film structure, composition, and thickness were studied and correlated to changes in various experimental parameters. Some important issues concerning the CVD processing of lead titanate based thin films were also addressed such as the reproducibility of stoichiometric films, film/substrate interactions and the effects of annealing on the CVD films after deposition.

CHAPTER 2: KINETICS AND GROWTH BEHAVIOR OF THE MOCVD OF PbO

2.1 Introduction

Metallorganic Chemical Vapor Deposition (MOCVD) is an important technique for the synthesis of thin films for the microelectronic industry. The MOCVD process offers several advantages over competing processes such as sputtering, evaporation and the sol-gel technique including the unique combinations of flexible composition control, excellent step coverage, and amenability to large-scale industrial processing. Many of the materials with potential applications as ferroelectric, pyroelectric, piezoelectric and optoelectronic devices are members of the lead-based perovskites including lead titanate, PZT, PLZT, etc. and require a precursor as a lead source for the synthesis of these materials. The tetragonal form of PbO, by itself, exhibits useful photoconductive properties as well [4]. Thus, a knowledge of the kinetics and deposition characteristics of PbO is extremely useful for these applications.

2. 2 Precursor Properties and Selection

Lead bis-tetramethylheptadionate ($Pb(thd)_2$) has been found to be one of the best candidates for a lead-based metallorganic precursor for the CVD process [2, 15]. Some of the important properties considered in selecting a precursor include volatility, thermal and environmental stability, decomposition behavior, ease of handling, and safety considerations [2]; $Pb(thd)_2$ is adequate or superior to other existing lead precursors in all

of these categories. Use of $Pb(thd)_2$ results in no film contamination problems and this precursor also has superior volatility compared to the other existing lead β-diketonates [16] and for these reasons was chosen for our study.

$Pb(thd)_2$ belongs to a class of chelating metallorganic compounds known as metal β-diketonates [16]. These compounds consist of a metal ion with an n^+ oxidation state at the center of the molecule to which are bonded 'n' chelating β-diketonate ligands [15]. β-diketonates are of interest in the design of MOCVD precursors because they are capable of forming volatile chelates with almost any metal [15]. Also, by varying the R-groups attached to each of the ligands, their volatility and chemical stability can be controlled. Most organic ligands become less volatile as their molecular weight is increased by attaching larger R-groups. For β-diketonates, however, the opposite is sometimes true; volatility actually increases with larger R-groups [15, 17]. It is generally agreed that these larger R-groups allow more effective shielding of the metal center, thus reducing potentially harmful molecular interactions such as oligimerization that will considerably reduce their volatility [15, 17]. Fluorinated R-groups can also significantly increase the volatility of these ligands but precursors containing these volatile groups are known to produce fluorine contaminated films [16].

The $Pb(thd)_2$ complex consists of a lead ion at the center of the two β-diketonate ligands. Bulky t-butyl groups are at each of the R-sites on the ligands. The structure of this molecule is shown schematically in Fig. 2.1 [16].

$Pb(thd)_2$ was successfully synthesized in our lab by the reaction of PbO powder with purified H-thd; toluene was used as the solvent and an ultrasonic bath was used to enhance the reaction [16]. Thermogravimetric analysis (TGA) was used to determine the rate of weight loss as a function of temperature and was used to determine the vapor pressure of the precursor as a function of temperature given in Fig. 2.2 [16]. From the

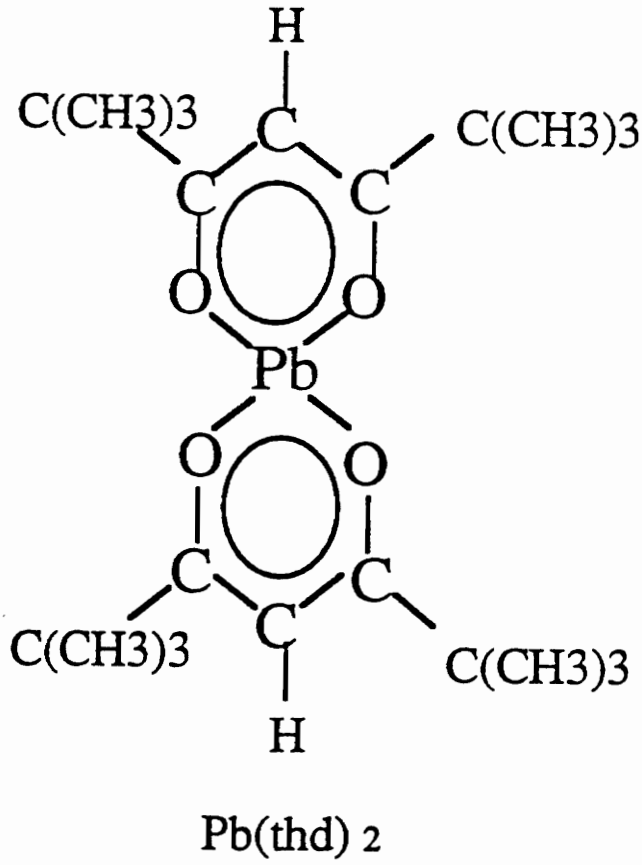

Figure 2.1: Structure of the $Pb(thd)_2$ molecule

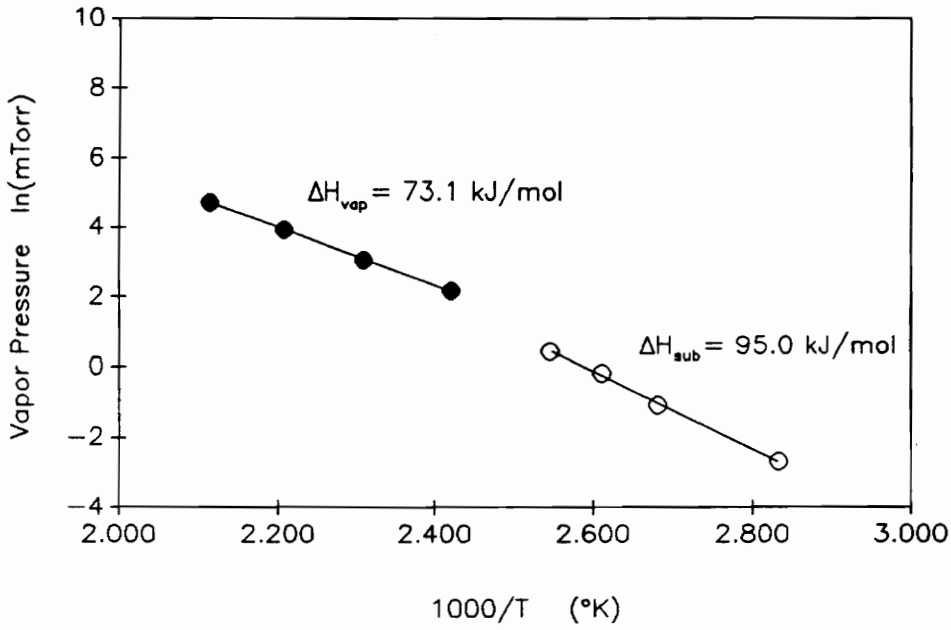

Figure 2.2: Vapor pressure vs. temperature for $Pb(thd)_2$

vapor pressure behavior it was possible to determine the enthalpies for the evaporation and sublimation of $Pb(thd)_2$ which were found to be 73.1 kJ/mol and 95.0 kJ/mol, respectively [16]. Further details of the synthesis and characterization of $Pb(thd)_2$ may be found in Ref. 16 (Nyman, 1992).

2.3 MOCVD Experimental Procedure

The application of $Pb(thd)_2$ in a hot-walled MOCVD reactor for the deposition of PbO was studied experimentally. A schematic diagram of the system is given in Fig. 2.3. The reactor consists of a 2" diameter stainless steel tube which is evacuated by means of a mechanical vacuum pump and liquid nitrogen cold trap; it is heated resistively using a tube furnace. The temperature profile across the length of this reactor for each of the three temperature settings used is given in Fig 2.4. Reactor temperature was set using a temperature controller equipped with a thermocouple positioned between the furnace and the reactor tube midway along the length where the temperature is maximum. Using a thermocouple placed at various locations inside the furnace, the temperature profile inside the reactor was obtained for each position and temperature setpoint used.

Approximately 1.0 g of fresh $Pb(thd)_2$ precursor was placed inside a stainless steel bubbler at the start of each deposition. Using customized heaters, the bubbler and its contents were heated to the bubbler temperature, T_B, by means of a microprocessor controlled temperature controller within $\pm 1^0C$; in order to ensure sufficiently high vapor pressure without significant decomposition of the precursor, the bubbler temperature was fixed at 165 ^0C, it has been shown that significant oligimerization occurs beyond this temperature [16]. Oxygen serves as both the diluent and reactive species, which was varied between 250 and 750 sccm; nitrogen was sent

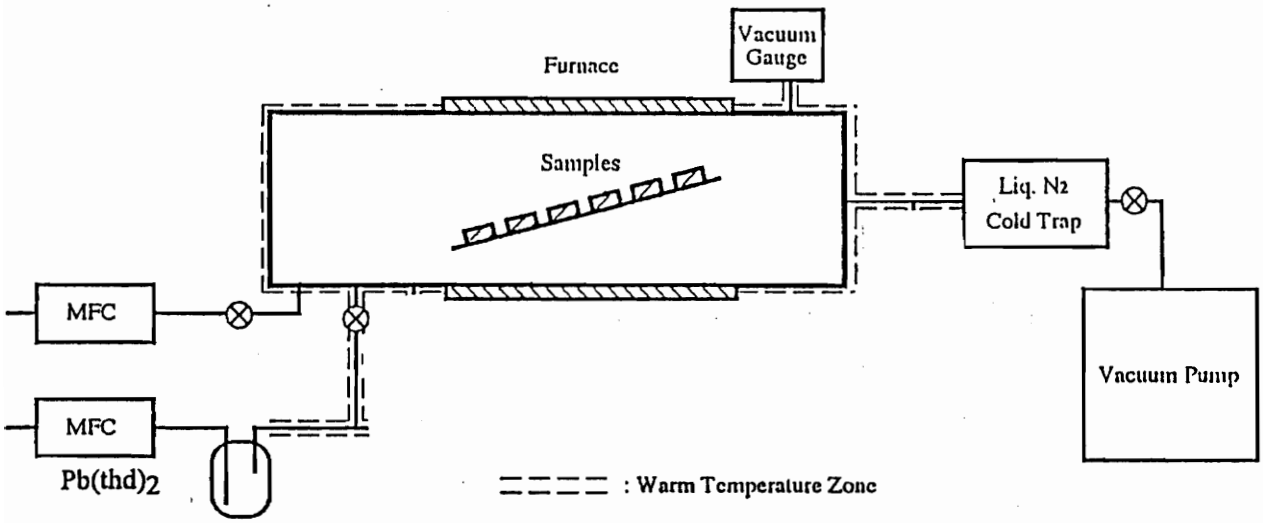

Figure 2.3: MOCVD apparatus for the deposition of PbO from $Pb(thd)_2$

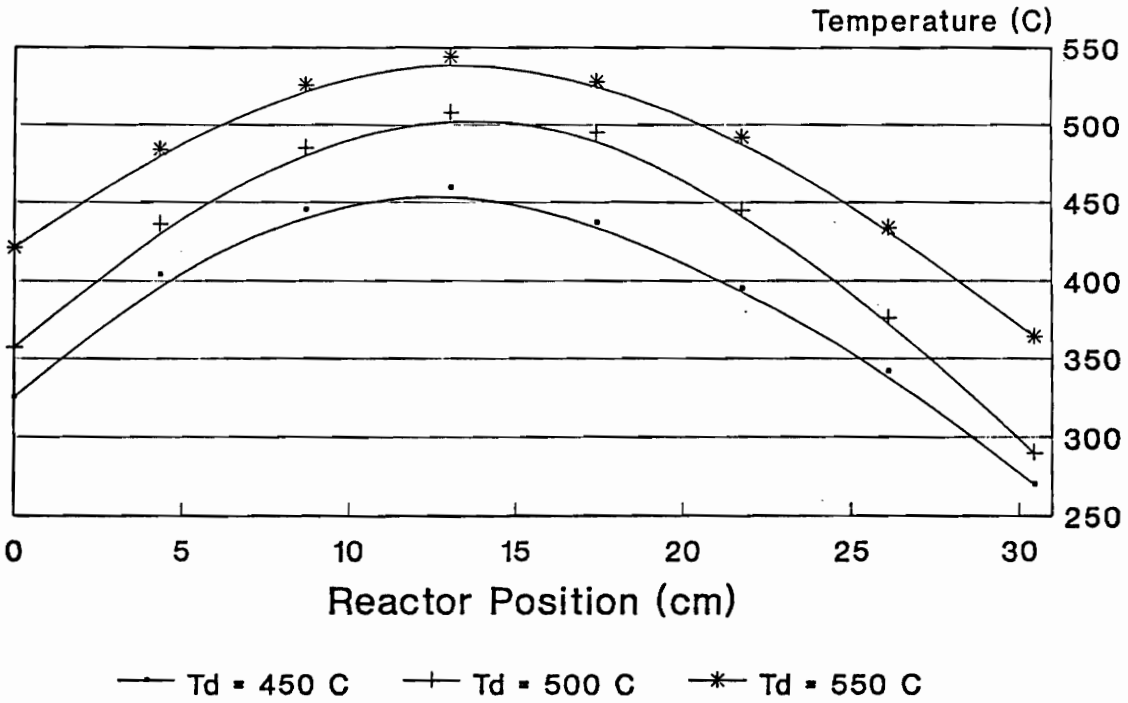

Figure 2.4: Temperature profiles in CVD reactor for $T_d^* = 550\ ^0C$, $500\ ^0C$, and $450\ ^0C$

through the bubbler as the carrier gas and was fixed at 75 sccm. For each deposition experiment, eight polycrystalline alumina wafer pieces or sapphire disks were placed at equal intervals along a 30 cm length centered about the hot zone of the reactor; each data point shown in the temperature profiles corresponds to a location and temperature where a substrate was placed.

Deposition rates were determined by weighing the substrates before and after deposition. The mass flux deposition rate was then calculated from the known substrate area; the deposition rate was found to vary smoothly over the length of the reactor for total flow rates below 1000 sccm and pressures below 8 torr. At higher pressures and flow rates, the substrates appeared to have small spots and streaks of nonuniform thickness, probably as a result of turbulence in the gas flow. Consequently, in this analysis, these flow regimes were avoided. Deposition was continued for 30 minutes before closing off the bubbler and allowing the furnace to cool. The reactor was then evacuated following each deposition.

2.4 RESULTS AND DISCUSSION

2.4.1 FEM Modeling of the MOCVD Process

After determining the film thicknesses resulting from each deposition it was possible to construct deposition profiles showing the effect of reactor position on deposition rate; these profiles are given in Figs 2.5, 2.6, and 2.7 along with the corresponding simulated profile for a variety of conditions. Upon examining the deposition profiles for several different conditions it becomes obvious that no meaningful study can be conducted by examining the deposition rate at a single point, even if that

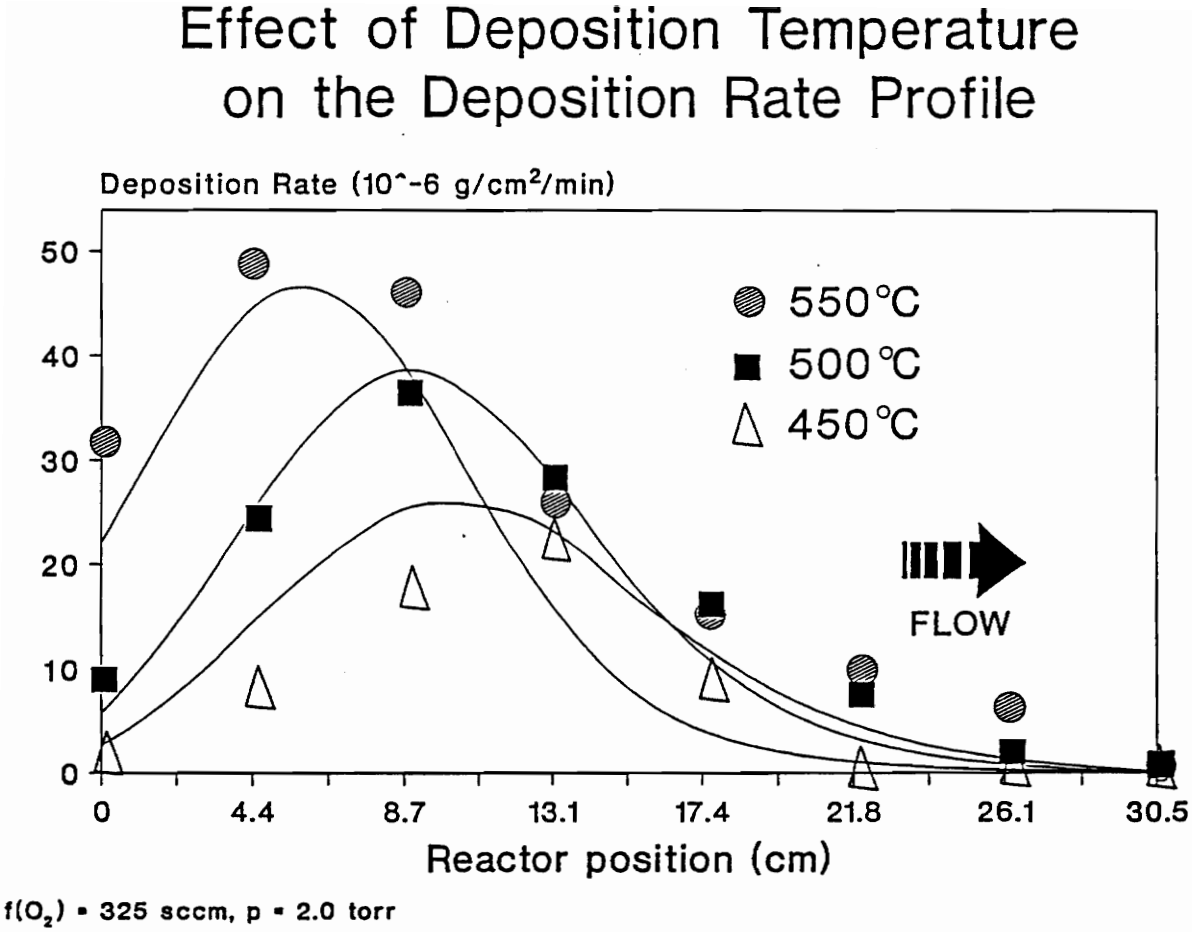

Figure 2.5: Effect of deposition temperature on deposition rate for experimental data (points) and simulated data (curves) for various reactor positions

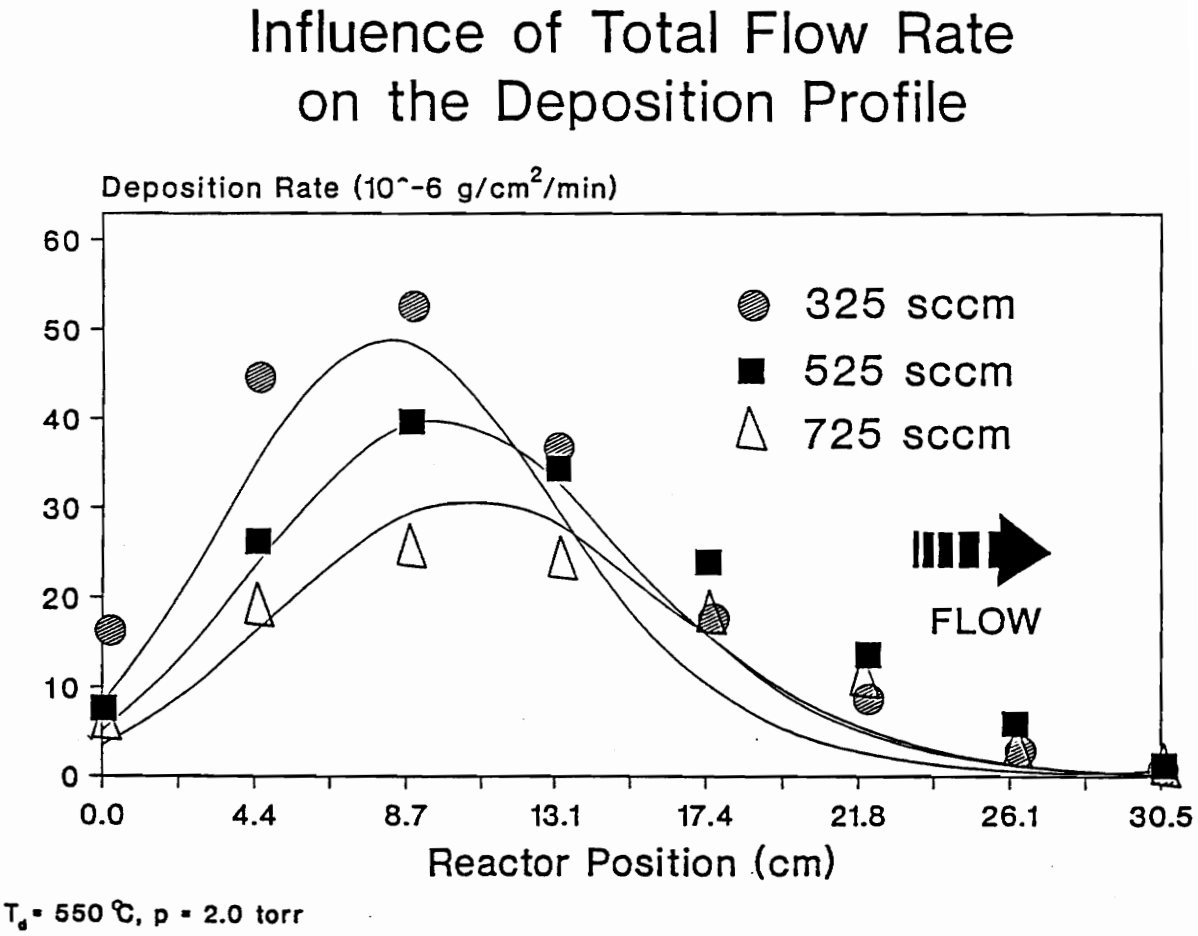

Figure 2.6: Effect of total flow rate on deposition rate for experimental data (points) and simulated data (curves) for various reactor positions

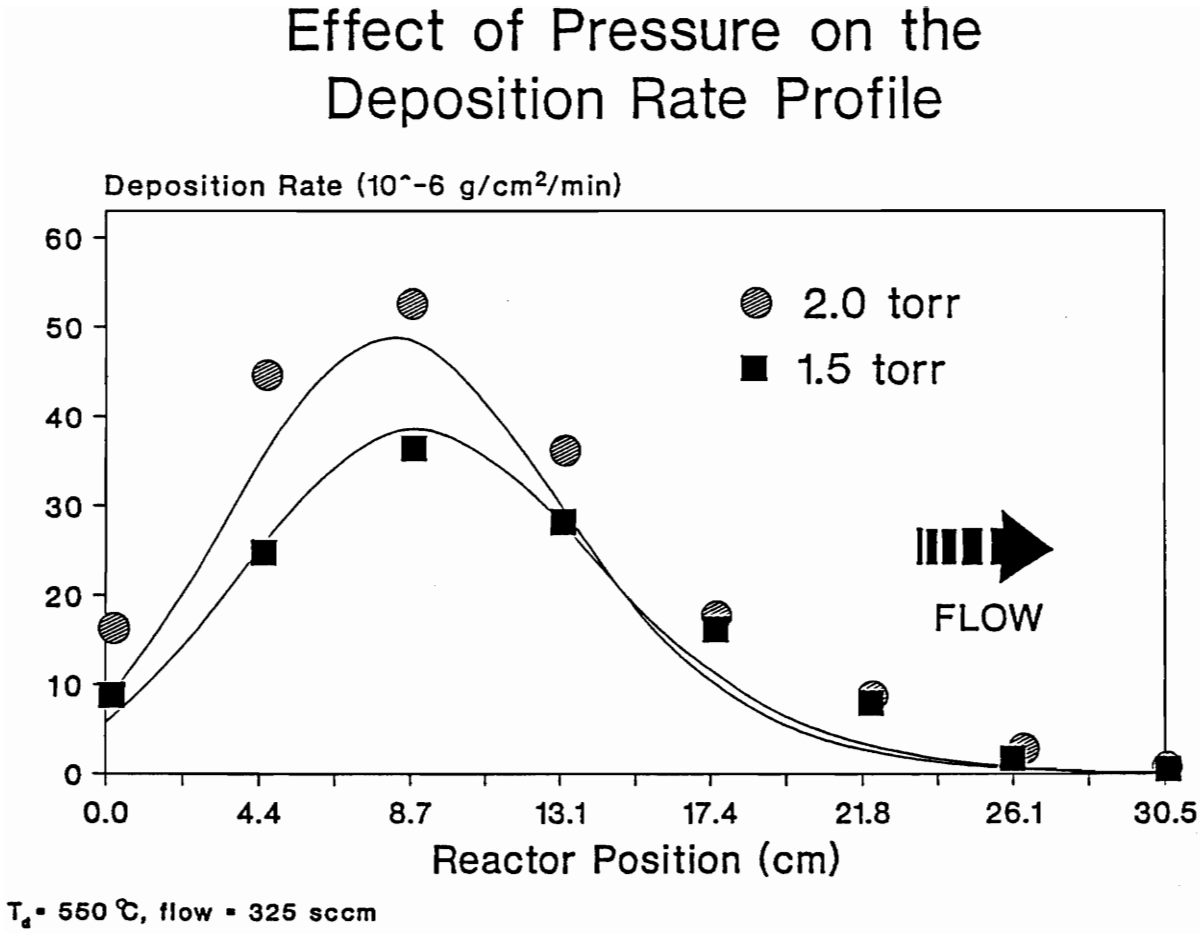

Figure 2.7: Effect of total pressure on experimental data (points) and simulated data (curves) for various reactor positions

exact point is examined repeatedly for each consecutive deposition. This is because the deposition rate for a given point depends not only on the temperature and pressure in the immediate vicinity but also on the flux of reactant to that point. The precursor reactant flux, in turn, depends on the overall amount of depletion occurring in earlier parts of the reactor as a result of the deposition process; this is complicated considerably by the nonuniform temperature profile. Because of this inherent nonlinearity it is impossible to propose a single equation which will describe the deposition rate as a function of position, temperature, pressure, etc. Thus, it becomes necessary to introduce a model using the Finite Element Method (FEM) which can be solved by an appropriate computer program. The FORTRAN code for this program appears in Appendix A.

Although there are many possible side reactions that occur during the CVD process, the model used here assumes that the final surface reaction occurring on the substrate is the rate limiting step in the overall process. This assumption may be justified both on the success of the predictions of the resulting model and on the structure of the resulting films which will be discussed in Section 2.4.4.2. Thus, the reaction rate constant, k, is identical to the surface reaction rate constant, k_s, which can be expressed as follows:

$$k = k_s = k_0 \exp\left(\frac{-E_a}{RT}\right) \qquad \text{[Eqn. 2.1]}$$

In eqn. 2.1 above, k_0 is the preexponential constant which is independent of temperature and E_a is the effective activation energy for the process. It is not known which of the reactions comprising the surface reaction is actually the rate-limiting process; however it is reasonable to assume that there is a single rate-limiting step that corresponds to the activation energy used here, E_a. First order reaction kinetics are being assumed in this model.

For each given point in the reactor the total mass entering and leaving that point by diffusion, convective transport and surface reaction must be accounted for; we will assume the concentration profile is essentially one-dimensional and hence the following steady-state continuity equation is employed [3]:

$$\frac{dP}{dt}\Big|_x = -D\frac{d^2P}{dx^2} + U\frac{dP}{dx} + \left(\frac{k_s}{2\pi r}\right)P = 0 \qquad \text{[Eqn. 2.2]}$$

In eqn. 2.2, above, P represents the partial pressure of $Pb(thd)_2$, x represents the distance along the length of the reactor (cm), D is the diffusion coefficient of the precursor molecule (cm/s^2), T is the temperature (^0K) , U is the convective transport coefficient (cm/s) and $2\pi r$ is the circumference of the reactor (cm). The deposition rate, D. R. ($g/cm^2/s$), at any given point in the reactor is the product of the local reaction rate constant (cm/s) and reactant (precursor) concentration (g/cm^3). Since oxygen is sent in considerable excess of the $Pb(thd)_2$, it can be assumed that the oxygen concentration is supersaturated and thus only the concentration of the $Pb(thd)_2$ precursor need be considered in determining the expression for the deposition rate, D.R.:

$$D.R. = k_s\, C_{Pb(thd)2} = k_0 \exp\left(\frac{-E_a}{RT}\right)\left(\frac{P_{Pb(thd)2}}{RT}\right) \qquad \text{[Eqn. 2.3]}$$

Since typical precursor concentrations are very dilute, the ideal gas approximation was used above to write the deposition rate in terms of the precursor partial pressure. With the two equations above, one relating the pressure, P, and position, x [Eqn. 2.2], while the other relating the deposition rate, D.R. and pressure, P [Eqn. 2.3], it is possible to

combine the results of these equations simultaneously by an iterative technique to determine D.R. as a function of x once we have the appropriate kinetic parameters, k_0 and E_a. Alternatively, the kinetic parameters can be obtained using several experimentally determined deposition profiles; this was the approach taken here. The equations can not be solved explicitly, as mentioned earlier, because of the nonuniform temperature profile. Consequently, a 16 element finite element grid was used with each substrate position representing a node in the grid. For each experiment, we can find the temperature and deposition rate at each node. These data can be entered into the finite element program which will determine the deposition profile for the specified kinetic parameters. By choosing suitable kinetic parameters which are fixed for all experiments once chosen, deposition profiles can be obtained which fit all of the experimental data quite well. The simulated data was found to agree well for all experimental conditions when the preexponential rate constant, k_0, was chosen to be 33 g/cm^2/min (0.15 mol/cm^2/min) while the effective activation energy was chosen to be 82 kJ/mol. As was seen in Figs. 2.5, 2.6, and 2.7 the simulated data agrees very well over a range of temperatures, pressures and total flow rates. By substituting these kinetic parameters into eqn. 2.3 it is possible to obtain an expression for the deposition rate dependent on only the local partial pressure of precursor and the local temperature.

2.4.2 Determination of Entrance Precursor Partial Pressures

The entrance vapor pressure depends on the following experimental parameters: bubbler temperature, total reactor pressure, carrier gas flow rate and total gas flow rate (carrier gas and dilute gas flow rates combined). Each of these parameters was observed to have the following intuitive effects:

Raising the bubbler temperature increases the equilibrium vapor pressure of the precursor thus increasing the precursor partial pressure both in the bubbler and in the reactor. The vapor pressure of any given precursor is generally very sensitive to temperature due to the exponential dependence of the vapor pressure on temperature.

Changes in the total reactor pressure have a more complex effect; the obvious main effect of increasing the total reactor pressure is a parallel and proportional increase in the precursor partial pressure. A lesser effect, however, is to increase the total pressure in the bubbler which reduces the evaporation rate of the precursor and its corresponding partial pressure. The net effect, in all cases, however, was to increase the precursor partial pressure but generally not to the extent that would be expected without considering the effect of the pressure on the vaporization rate.

Increasing the carrier gas flow rate reduces the boundary layer thickness in the bubbler above the precursor and hence enhances the vaporization rate and increases the precursor partial pressure in the reactor.

Increasing the total gas flow rate effectively dilutes the precursor concentration in the reactor and consequently reduces the precursor partial pressure proportional to the amount of dilution. There is also a proportional increase in the flow velocity in the reactor.

Since we are interested mainly in the kinetics of the CVD reaction itself and less on vapor transport considerations, all depositions that were used as experimental data in the simulation were obtained using a bubbler temperature of 165 ^{0}C and a carrier gas flow rate of 75 sccm. Since the total flow rate only serves to dilute the precursor vapor and has no effect on the actual vaporization rate in the bubbler, the only remaining variable which has an effect on the vaporization rate is the total pressure. Consequently, the actual precursor vapor pressures were obtained for each of the pressures used in the simulation, holding all other factors constant. Precursor vapor pressures were obtained by setting up the reactor

as if conducting a deposition (the furnace was heated as well as were the bubbler and heating cords). The desired amount of dilute gas was sent and allowed to stabilize, then the desired pressure was obtained by adjusting the pump valve. The carrier gas is now sent in the absence of precursor and, after reaching a steady state, the change in pressure is recorded. The same experiment is now repeated exactly but the precursor is placed in the bubbler. The difference in the pressure change observed while using the precursor is due to the additional vapor pressure of the precursor. The vapor pressures were measured at a total gas flow rate of 325 sccm (250 sccm dilute gas, 75 sccm carrier gas) at 1.6 torr and 2.0 torr and found to be 0.003 torr and 0.004 torr, respectively. Because of random pressure fluctuations on the order of 0.0005 torr when conducting the measurements, it is not possible to obtain more precise values. In order to find the vapor pressure at a total gas flow rate other than 325 sccm, we simply multiply by a dilution factor:

$$P_{vap}(@f_{tot}) = \frac{325}{f_{tot}} P_{vap}(@325\ \text{sccm})$$

where f_{tot} is expressed in sccm. Thus, for the simulated experiments used in this paper, the following vapor pressures were used:

TABLE 2.1: $Pb(thd)_2$ Partial Pressures

	TOTAL FLOW		
TOTAL PRESSURE	**325 sccm**	**525 sccm**	**725 sccm**
1.6 torr	0.003 torr	0.0020 torr*	0.0014 torr*
2.0 torr	0.004 torr	0.0027 torr*	0.0018 torr*

*Calculated based on value measured at 325 sccm total flow rate

2.4.3 Comparison of Experimental Data and Simulated Behavior

Experiments were conducted over a range of experimental conditions. In order to get an intuitive feel for the change in the deposition rate profile with experimental conditions, three sets of experimental data are presented. The first set, Fig. 2.5, shows the effect on the deposition profile of increasing the temperature through 450, 500 and finally 550 ^{0}C. As the temperature was increased, in all experiments the maximum deposition rate was found to increase; also, the position at which this maximum occurs was found to move closer to the entrance due to the more rapid depletion of precursor from the gas phase. Thus it is seen that it is possible to increase the temperature profile for a given experiment and yet have a decrease in deposition rate for a substrate positioned near the center simply due to the decrease in the flux of precursor as a result of earlier depletion.

The second set of data, Fig. 2.6 shows the effect of increasing the diluent gas flow rate at a constant total pressure. The main effect is to decrease the overall profile due to a reduction of the precursor partial pressure; the reduction in overall deposition rate also limits the depletion effect and tends to move the maxima closer to the center.

The third set of data, Fig. 2.7, shows the effect of changing the total pressure; the shape is largely unchanged but tends to increase or decrease in accordance with the total pressure as a result of the changing precursor partial pressure. As discussed earlier, this effect is somewhat less than would be expected without considering the effect of pressure on the precursor vaporization rate. In all three sets of data, the model was found to conform quite well with our experimental results.

2.4.4 Crystal Structure and Morphology

2.4.4.1 X-Ray Diffraction Study

XRD was used to determine the crystal structure of the films. In every case, regardless of oxygen partial pressure, only the monoxide form of lead, PbO, was observed; litharge (tetragonal α-PbO) was found to be deposited at the lower temperatures while a mixture of litharge and massicot (orthorhombic β-PbO) was deposited at the higher temperatures. Metastable massicot was found in detectable amounts on substrates deposited at temperatures as low as 420 ^{0}C despite the fact that the equilibrium temperature for the α and β forms to coexist is 550 ^{0}C. Also, based on the total intensity of the XRD peaks for each phase, it was sometimes found that the proportion of orthorhombic PbO was found to actually decrease for substrates coated at higher temperatures. Also, the proportion of phases deposited was found to depend on the deposition rate (or film thickness) as well as the temperature. The XRD patterns for the three different temperature profiles used are given in Figs. 2.8, 2.9, and 2.10.

PbO was also deposited on sapphire disks (oriented within a 30 degree cone of the sapphire c-axis) which was found to promote a preferential [100] orientation in the orthorhombic PbO; on some occasions only the [200] XRD peak could be observed; while for the PbO deposited on the alumina the relative peak height ratios were close to those predicted from structure factor calculations. The XRD patterns on sapphire showing this preferred orientation is shown in Fig. 2.11.

One possible explanation which was considered for the apparently greater proportion of tetragonal PbO at higher temperatures is the fact that the transformation kinetics for the transformation from the high temperature orthorhombic phase to the low temperature tetragonal phase might occur faster at a higher temperature and might

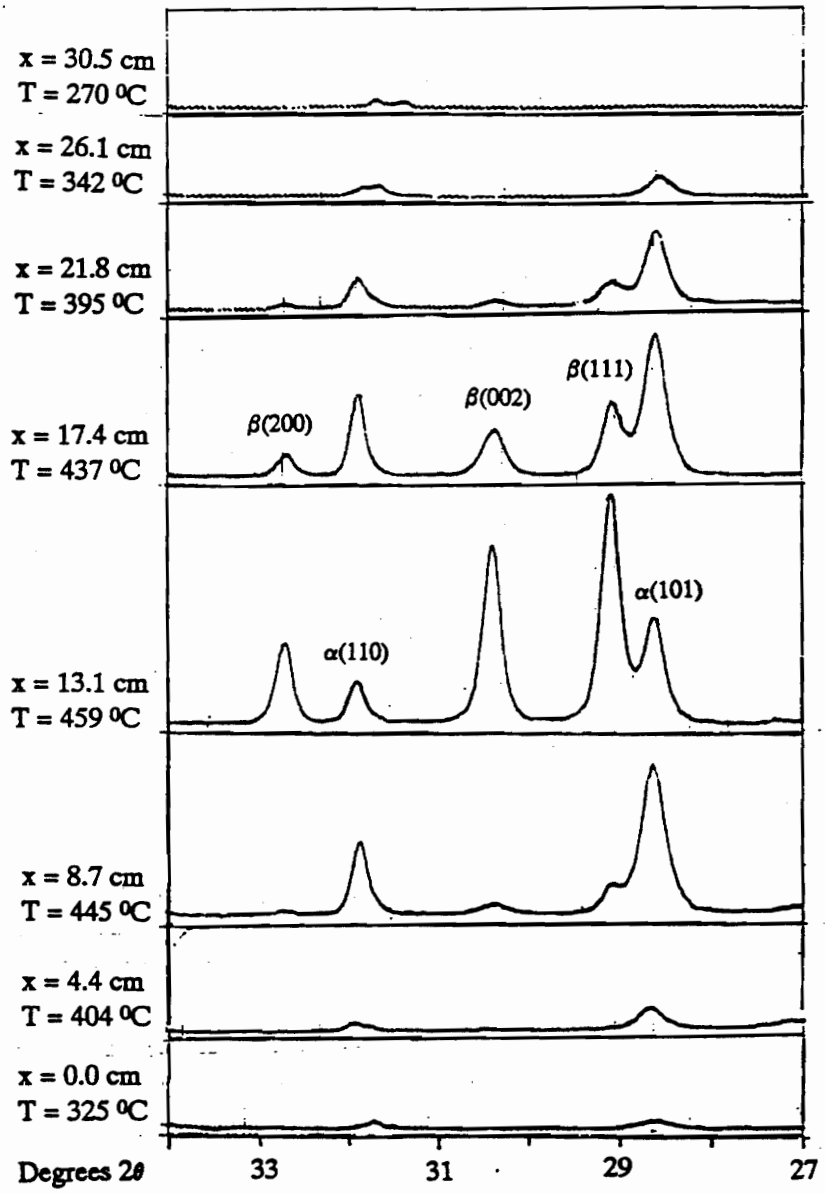

Figure 2.8: XRD results for PbO on polycrystalline alumina deposited at $T_d = 450\ ^{o}C$

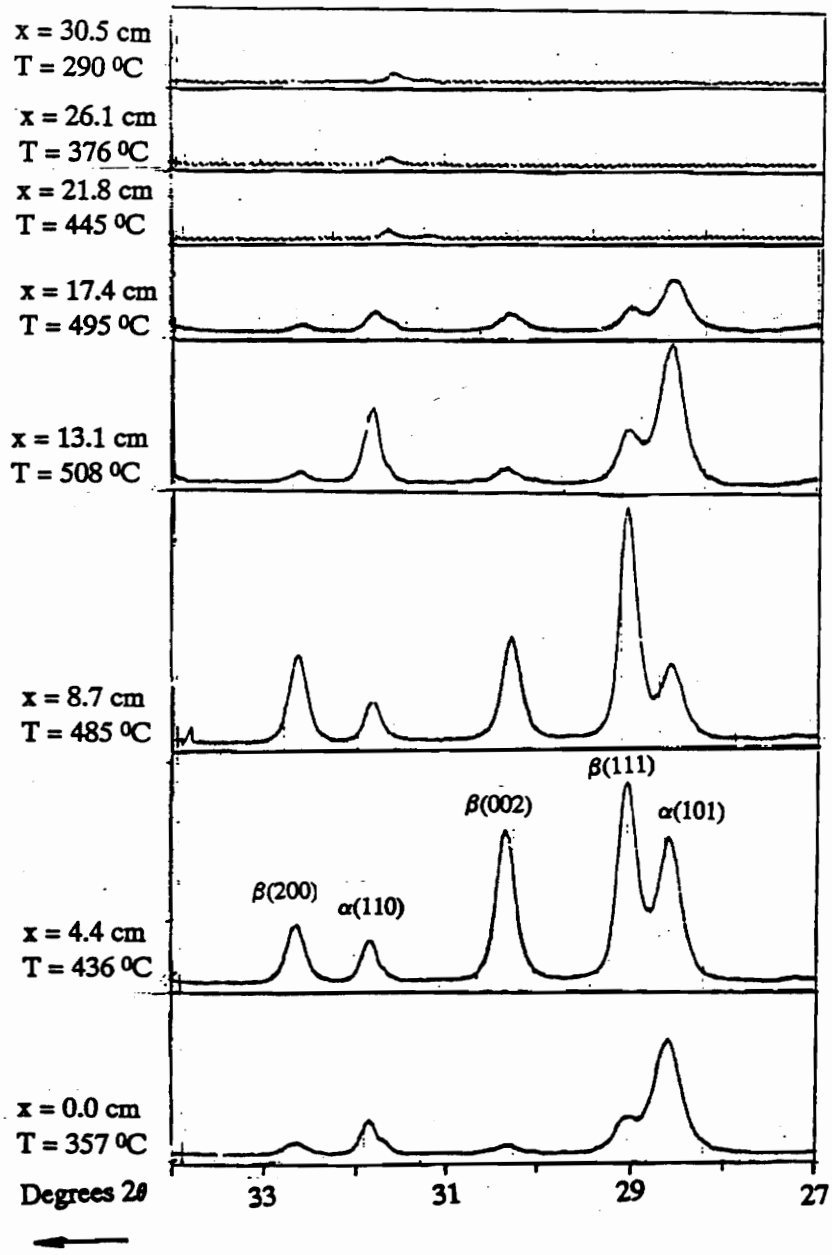

Figure 2.9: XRD results for PbO on polycrystalline alumina deposited at T_d = 500 °C

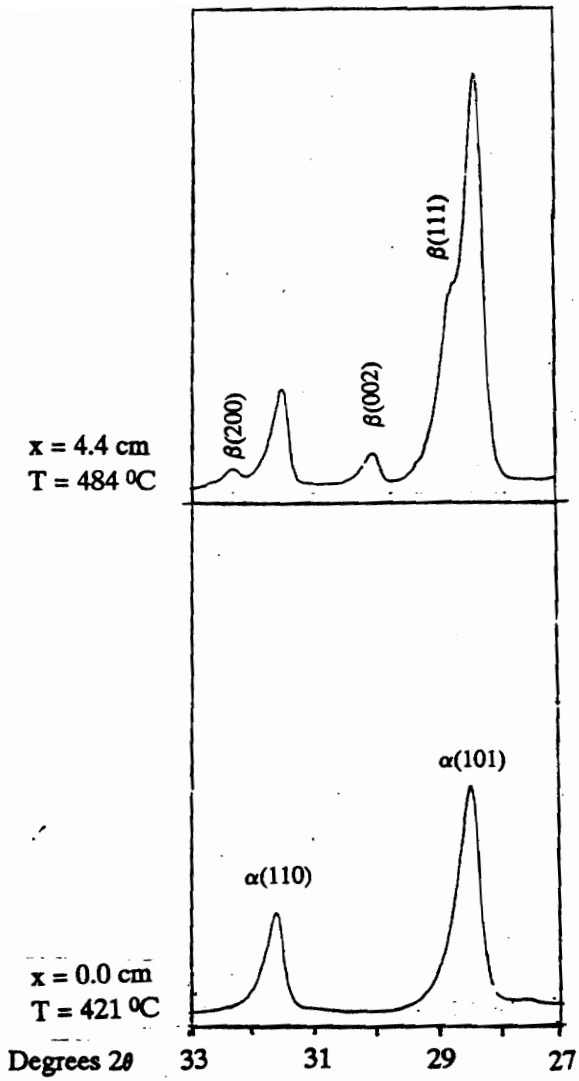

Figure 2.10: XRD results for PbO on polycrystalline alumina deposited at T_d = 550 °C

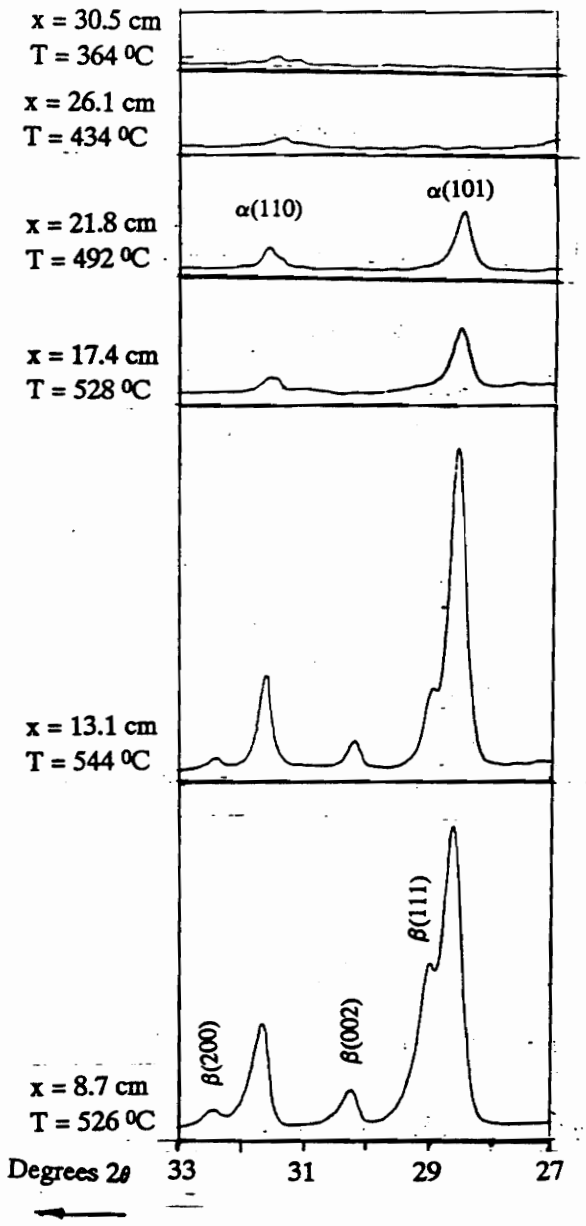

Figure 2.10: (Continued)

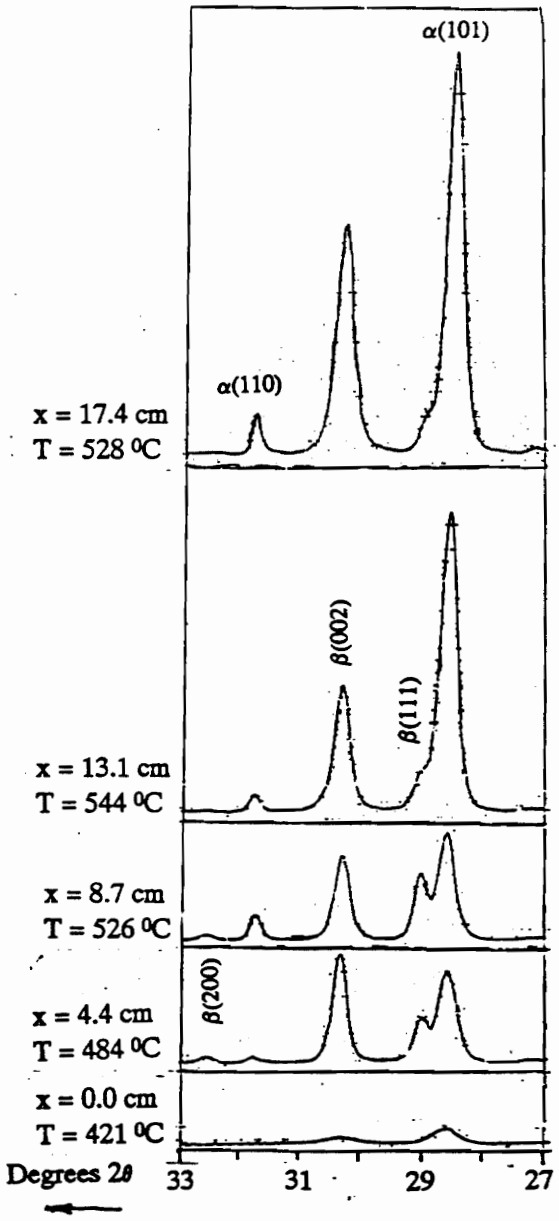

Figure 2.11: XRD results for PbO on sapphire deposited at T_d = 550 °C

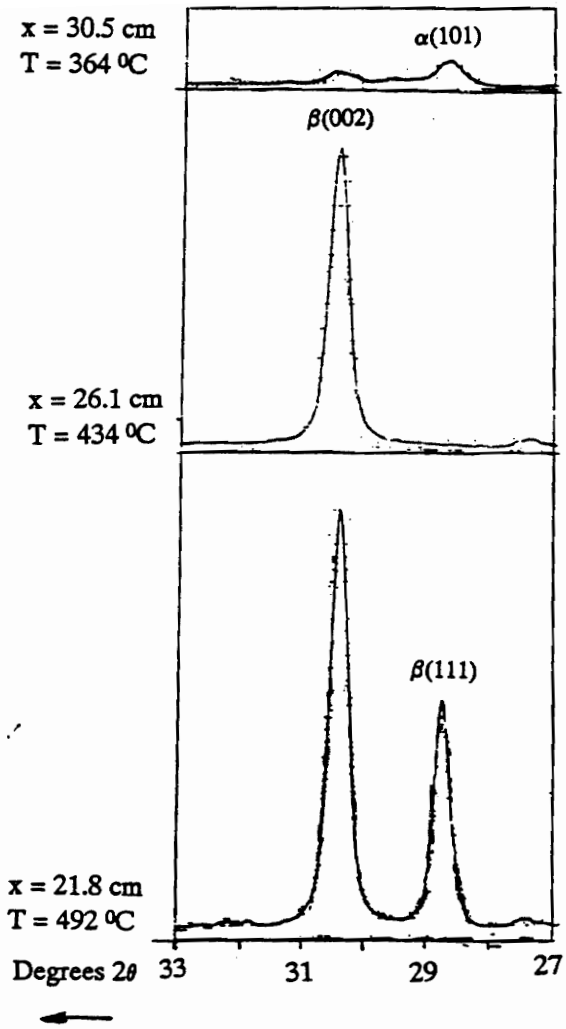

Figure 2.11: (Continued)

account for the anomalous behavior observed even if equivalent proportions of the two phases were deposited at each temperature. However, after four alumina substrates coated with a mixture of tetragonal and orthorhombic lead oxide were heat-treated at 450 ^{0}C for 2 hours then allowed to furnace cool, no change in the XRD pattern was observed (Fig. 2.12). This is consistent with other sources which report that the orthorhombic to tetragonal transformation of PbO does not occur except under special conditions [4]. These results also imply that at temperatures below the α-to-β transition temperature, the phases which were found to be present at the end of a deposition are determined by the kinetics of the deposition process and do not undergo any crystal structure change after being deposited. Thus, since more tetragonal PbO was found in some cases as the temperature was increased, we can conclude that the kinetics of the CVD process itself rather than thermodynamics is the controlling factor in determining the resulting crystal structure.

2.4.4.2 Surface Morphology Using Scanning Electron Microscopy (SEM)

The morphology of the deposited PbO was studied using Scanning Electron Microscopy (SEM) on sapphire and are shown for four different reactor positions from a single run in Fig. 2.13. The morphology was found to be dependent on the temperature and deposition rate. A smooth film was observed only for very low deposition rates; as the deposition rate became higher a structure consisting of randomly oriented platelets was found to occur. These platelets became significantly larger in diameter as the temperature and deposition rate was increased. The presence of these platelet-shaped crystals is indicative of a large anisotropy in growth rate kinetics with respect to crystallographic orientation. Interestingly, for position #7, the substrate shows a relatively

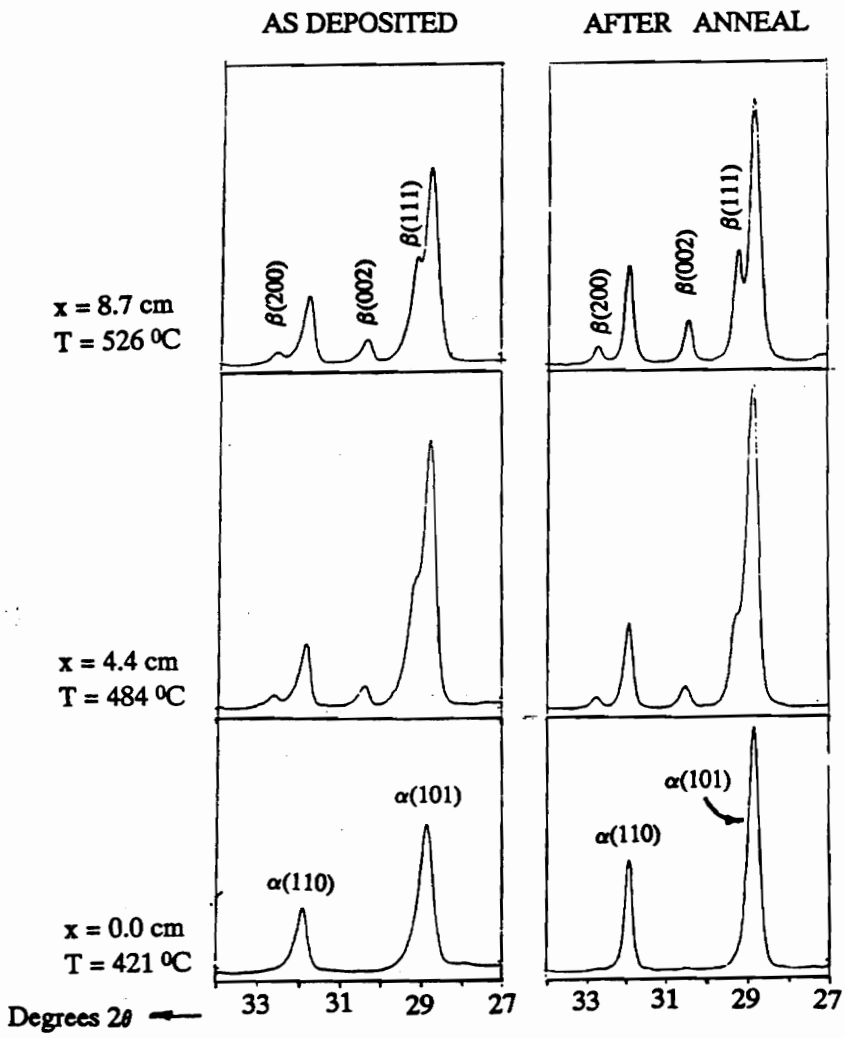

Figure 2.12: XRD results of PbO from Fig. 2.11 before and after 2 hr. anneal at 450 °C

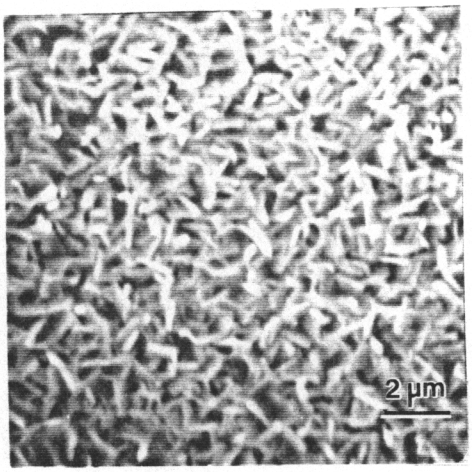

x = 0.0 cm
T = 421 ^{0}C

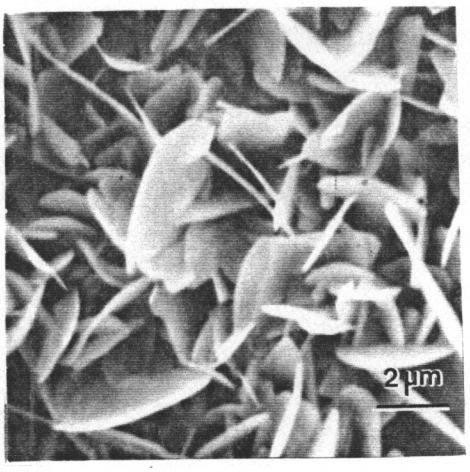

x = 8.7 cm
T = 526 ^{0}C

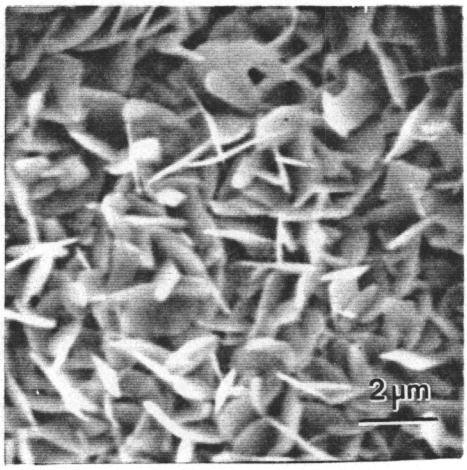

x = 17.4 cm
T = 528 ^{0}C

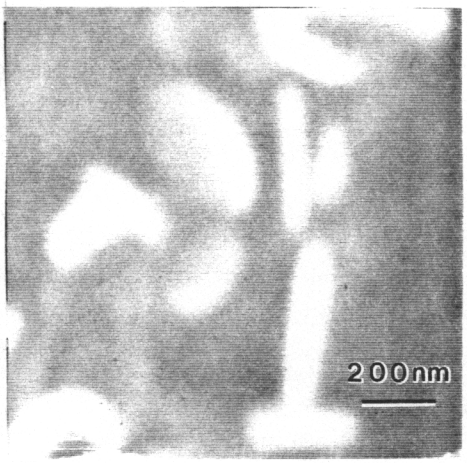

x = 26.1 cm
T = 434 ^{0}C

Figure 2.13: SEM micrographs of PbO on sapphire for four different positions of the same run shown in Fig. 2.11

smooth film with only a few very small platelets; only [100] oriented orthorhombic PbO was detected in the XRD pattern. This seems to suggest that the platelike morphology is characteristic of the tetragonal phase rather than the orthorhombic phase; this may provide an explanation for the apparently anomalous temperature behavior of the relative proportion of the two phases.

As can be seen from the experimental results, tetragonal PbO is generally favored at the higher deposition rates. In addition to the fact that the amount of time available for surface diffusion and the attainment of equilibrium is more limited at the higher deposition rates, the growth of tetragonal platelets from the surface may effectively shield the underlying orthorhombic phase, thus enhancing the growth of the tetragonal phase at the expense of the orthorhombic phase.

In general, the formation of well defined crystal planes during the growth of a crystal is indicative of substantially slower growth rates in the direction of these planes. Thermodynamically, the equilibrium shape of a crystal may be easily determined from the surface energies associated with each of the crystallographic planes; high energy planes have the fastest growth rates leaving surfaces of low energy planes [18]. Thus, the formation of plates signifies the fact that a single crystallographic direction has a much slower growth rate than the other directions, and as a consequence, only those faces normal to this slow growth direction remains. Based on the crystal structure of tetragonal PbO in Fig. 2.14 it can be seen that there are strongly bonded sheets in the (001) planes separated by a large gap. These layers are in turn bonded to one another by weak van der Waals forces operating between adjacent layers. Thus, thermodynamically, we would predict the (001) planes to have the lowest surface energy and thus determine the crystal habit for this crystal. For crystals grown hydrothermally, several investigators have reported this to be the case [5, 6, 7].

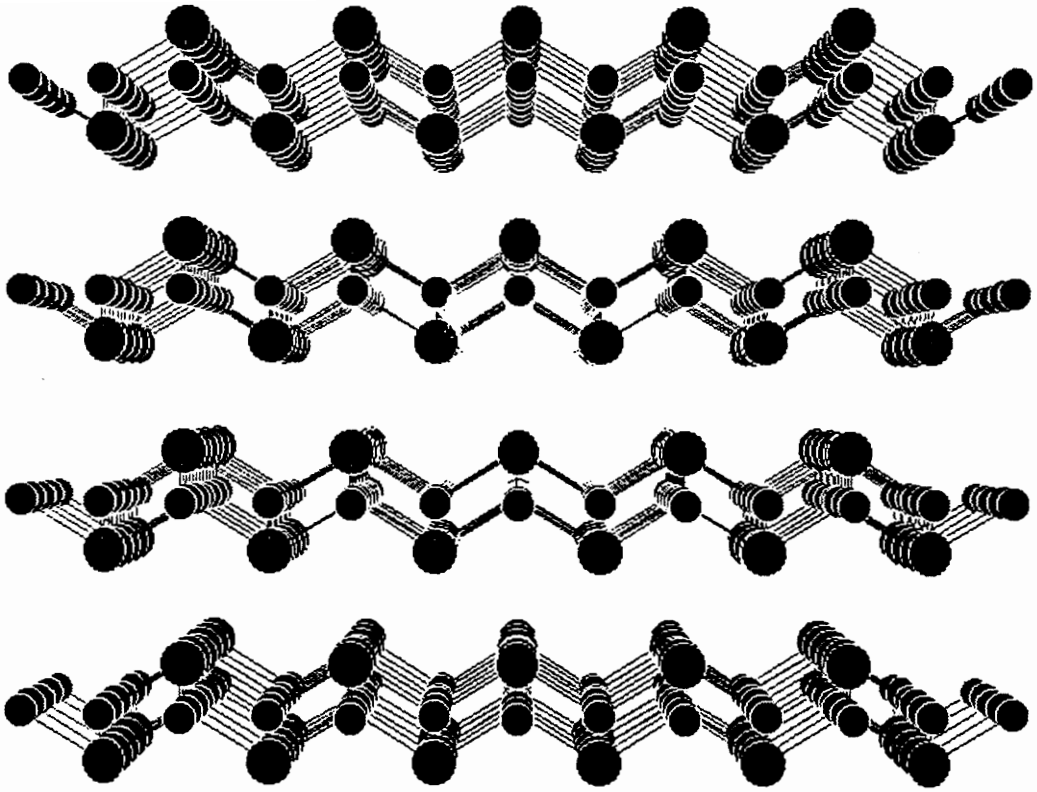

Figure 2.14: Simulated crystal structure of α-PbO looking along the a-axis

2.4.4.3 Transmission Electron Microscopy (TEM) Study

To determine the orientation of the plates grown in this experiment, the coating from one of the sapphire substrates which was found to consist of large PbO plates was scraped free and prepared for Transmission Electron Microscopy (TEM) investigation. Since the thickness of these plates was generally about 100 angstroms or less, it was possible to examine the plates without the usual thinning process that is often necessary for TEM investigation. Electron diffraction patterns were obtained for several platelets; in all cases, the phase of the platelets was tetragonal and the orientation was found to be normal to the <201> family of zones. The existence of these faceted plates is direct evidence of a deposition process which is controlled by surface kinetics, which had been assumed in the FEM model. Electron diffraction patterns and corresponding bright-field and dark-field photographs are given for two different platelets in Figs. 2.15(a), (b), and (c). The pattern appears at first to exhibit six-fold symmetry with four of the closest diffraction spots coming from the <112> family of directions, the other two coming from the <020> family. On closer inspection, however, it can be seen that the distance and corresponding reciprocal lattice vector for the <020> spots are actually about 6% larger than that of the <112> spots, which is consistent with the pattern that would be calculated based on the respective d-spacings. Regions of alternating dark and light bands seen in the bright-field image are most likely due to stacking faults. To confirm that the <201> choice of zone axis for the electron diffraction image of Fig. 2.15(b) was correct, the zone normal to the plane of the platelet was rotated a total of 21 degrees so that it was possible to obtain a second electron diffraction pattern shown in Fig. 2.16; this pattern was found to originate from the <100> zone with the nearest two spots corresponding to <020> directions. There

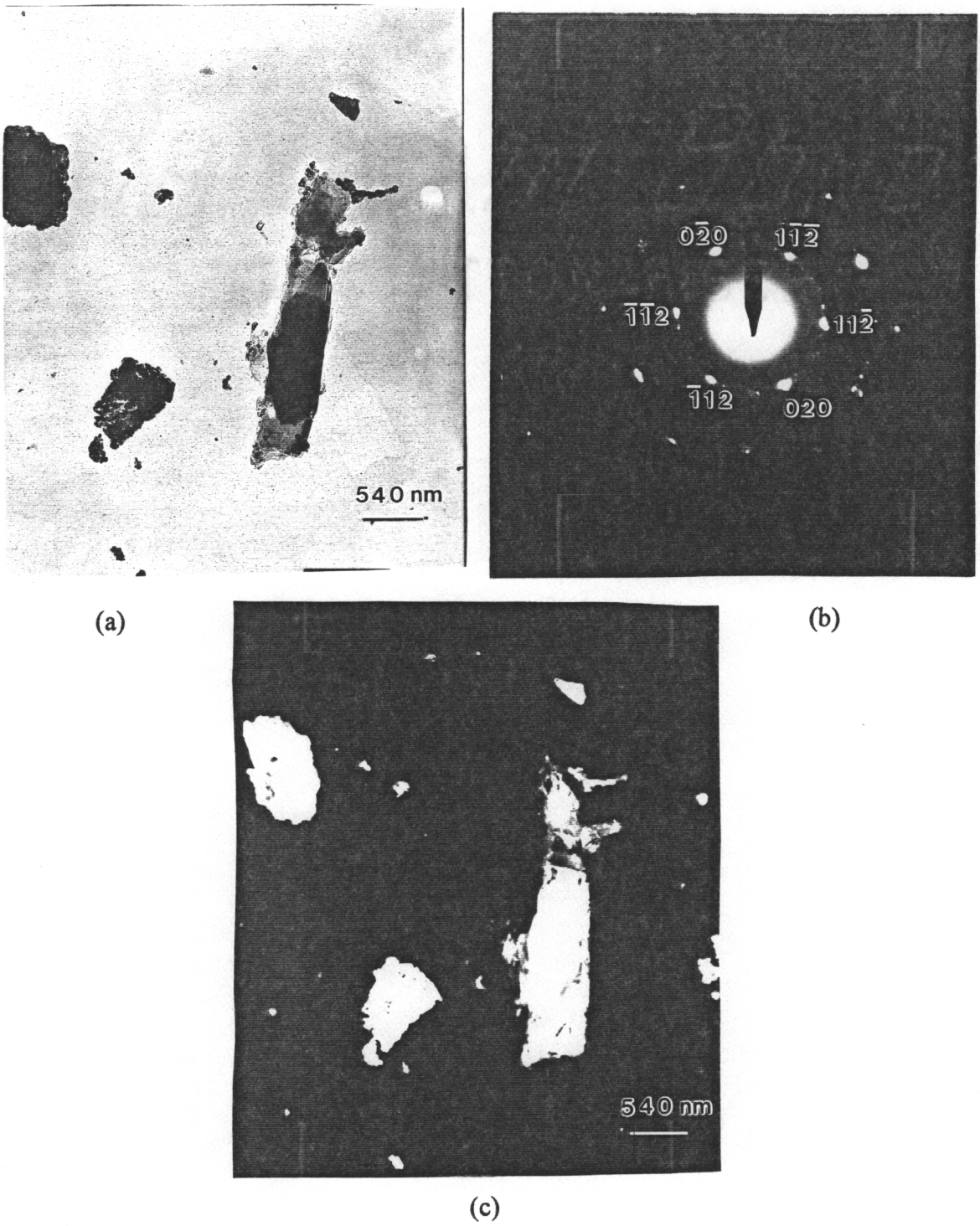

(a) (b) (c)

Figure 2.15: (a) Bright-field TEM micrograph of α-PbO platelets; (b) SADP of <201> zone of same platelet viewed normal to the plane of platelet; (c) Dark-field micrograph

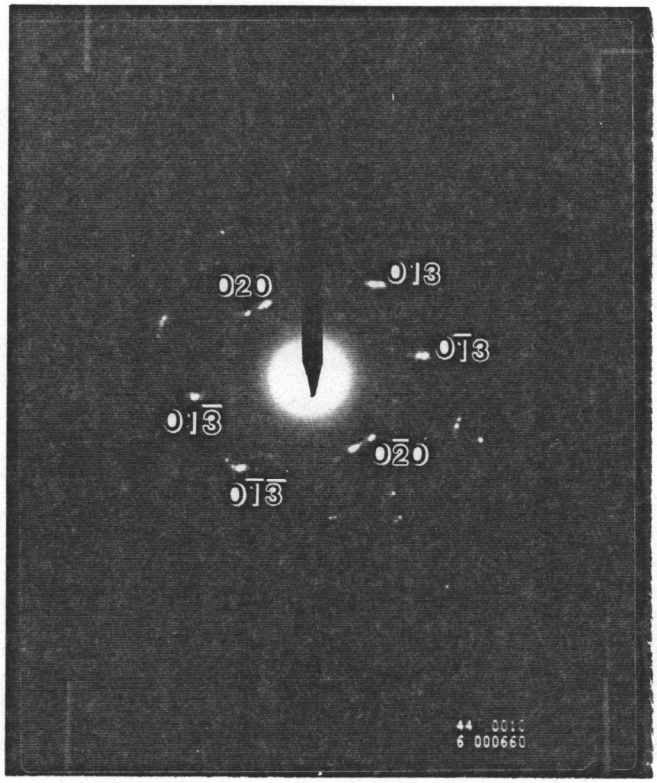

Figure 2.16: SADP of <100> zone of platelet in Fig. 2.15 obtained by rotating the stage

are two pairs of spots at a larger distance which correspond to the <013> family of directions.

While <201> is probably not the thermodynamically favored orientation for teragonal PbO platelets, it seems that in the particular CVD process studied here this growth morphology was favored from a kinetic standpoint. Interestingly, <201> oriented islands were also reported by Matthews et. al. [19] for the growth of α-PbO islands grown on the (111) surface of lead metal. A simulated view of the atomic structure of the crystal viewed down the <201> zone axis is given in Fig. 2.17 and shows the apparent six-fold symmetry which was also seen in the TEM electron diffraction patterns.

2.5 Summary and Conclusions

$Pb(thd)_2$ precursor was used to deposit PbO over a range of experimental conditions; the deposition rate profiles were found to conform well to the Finite Element Model that had been proposed for the process; the preexponential rate constant was determined to be 33 $g/cm^2/min$ (0.15 $mol/cm^2/min$) while the activation energy was found to be 82 kJ/mol. The films deposited on sapphire and alumina were found from XRD to consist of a mixture of tetragonal and orthorhombic lead oxide, the proportion of which depended on both the deposition temperature and the deposition rate. Using SEM, it was observed that the tetragonal form of PbO tends to grow in the form of platelets randomly oriented with respect to the substrate which were about 1 micron in diameter and about 100 angstroms or less in thickness. The orientation of each individual platelet was confirmed by TEM electron diffraction patterns to be the plane normal to the <201> zone.

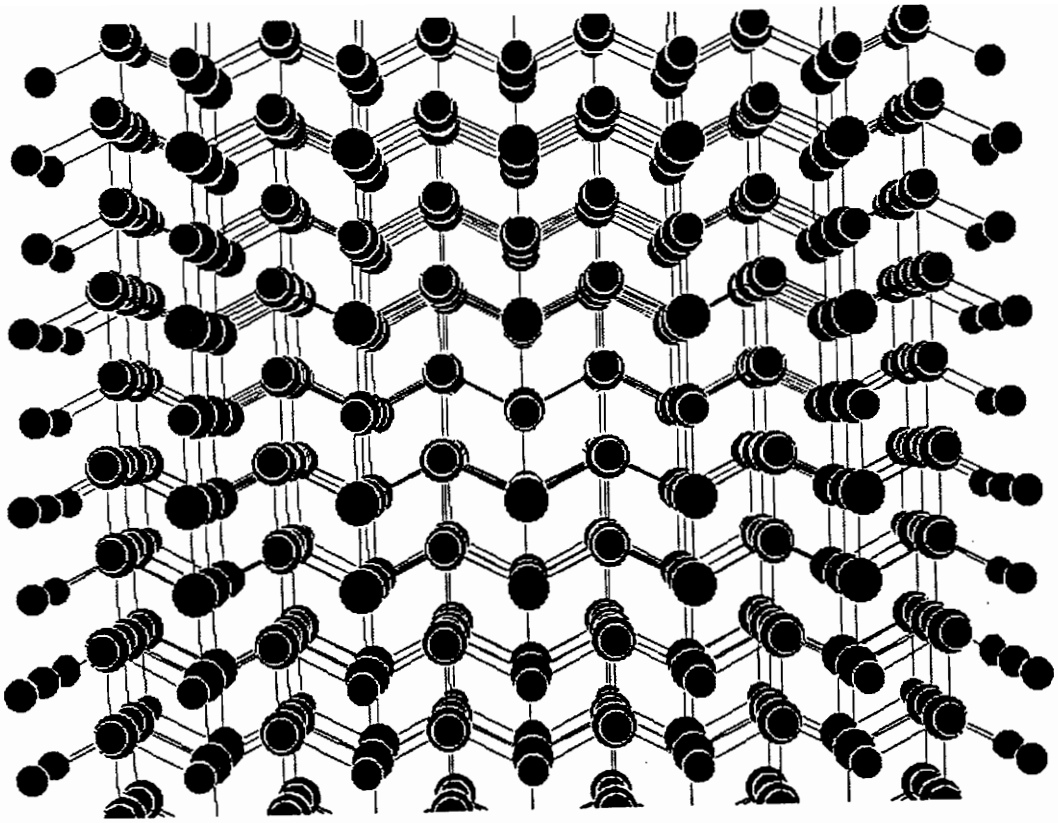

Figure 2.17: Simulated crystal structure of α-PbO looking in the direction of the <201> zone axis

CHAPTER 3: METALLORGANIC CHEMICAL VAPOR DEPOSITION OF LEAD TITANATE ($PbTiO_3$)

3.1 Introduction

Lead titanate (PbTiO3) based ceramics have been well known for their interesting piezoelectric, pyroelectric, ferroelectric, and electro-optic properties. In recent years, the thin film forms of $PbTiO_3$ (PT) and PT derived materials such as PZT and PLZT have generated considerable interest due to their potential application in nonvolatile ferroelectric RAMs (FRAMs). Undoped lead titanate thin films also find applications in optoelectronic devices, sensors and transducers.

While many processing techniques are available to synthesize lead titanate thin films, metallorganic chemical vapor deposition (MOCVD) is a promising technique for several reasons: the equipment is relatively simple (i. e. no high vacuum equipment or plasma generators are necessary), step-coverage is superior to all other processes, compositional control is extremely flexible and the process can be incorporated into large-scale industrial processing.

In this study, the deposition behavior of lead titanate was studied using the metallorganic precursor, lead bis-tetramethylheptadionate ($Pb(thd)_2$), described in chapter 2, and titanium ethoxide, a metal alkoxide formed by dissolving titanium oxide in ethanol. The structure, composition and thickness of the resulting films was studied using XRD, SEM, and EDX and was correlated with the experimental processing parameters. Optical and electrical properties were also obtained for the lead titanate films on sapphire and platinum-coated silicon, respectively. Several important processing issues are also addressed including the effect of post-deposition annealing, the existence of a high

temperature self-limiting reaction regime for high reproducibility of film stoichiometry, and also the stability of ruthenium oxide-coated silicon substrates in the MOCVD process environment.

3.2 Equipment and MOCVD Experimental Procedure

3.2.1 Precursors

The metallorganic precursors chosen for the MOCVD of lead titanate were lead bis-tetramethylheptadionate ($Pb(thd)_2$) for the lead source, and titanium ethoxide ($Ti(OEt)_4$) for the titanium source; both were obtained from Strem Chemicals, Inc. Titanium ethoxide belongs to a class of metallorganic compounds referred to as metal alkoxides. Metal alkoxides are generally used in liquid form and are formed by dissolving a metal oxide (titanium oxide, in this case) in an alcohol (ethyl alcohol) [20]. Titanium isoproxide ($Ti(OPr^i)_4$ is the most commonly used precursor in the literature [11, 12, 13, 14], but from other results obtained in our lab we have shown that titanium ethoxide is also a viable titanium source being easily vaporized and decomposed without any resulting film contamination as determined by Auger Electron Spectroscopy (AES) depth profiling [21]. Titanium ethoxide has a very high vapor pressure at relatively low temperatures also; its boiling point at 1 atmosphere is 122 ^{0}C [22].

3.2.2 Substrate Materials

The substrates used in this study included sapphire, as well as multilayer structures on silicon consisting of $Pt/Ti/SiO_2/Si$ and $RuO_2/SiO_2/Si$, which will be referred to

hereafter as platinum (Pt) and ruthenium oxide (RuO_2) substrates, respectively. The single-crystal sapphire (Al_2O_3) substrates used were obtained from the Swiss Jewel Company and were oriented within a 30 degree cone of the c-axis. Sapphire is a very useful substrate for investigating the properties of the deposited films, especially optical properties, since it is transparent over the entire visible spectrum and part of the ultraviolet region, with the absorption cutoff occurring at about 200 nm. Also, sapphire is extremely inert in the CVD environment and generally gives very clean x-ray diffraction (XRD) patterns except for an occasional (0001) peak.

The platinum and ruthenium oxide substrates were investigated also because these are typical conductive electrode materials used for ferroelectric thin films. Platinum is the conventional choice that has been traditionally used for electrodes; these substrates were obtained from Sharp, Inc. in Japan. Ruthenium oxide, on the other hand, has recently gained recognition as exhibiting superior properties to platinum electrodes, especially regarding the fatigue behavior of ferroelectric thin films [23]. The fatigue mechanism is believed to be related to the trapping of oxygen vacancies at the space charge region that forms near the electrode interface [24]. By using a conductive oxide rather than a metal electrode, this space charge region is considerably reduced [24]. Ruthenium oxide was processed in-house by oxidizing silicon wafers (both (100) and (111) oriented) at 950 ^{0}C in a wet oxygen environment, followed by sputter coating the ruthenium oxide using a ruthenium target in a reactive oxygen atmosphere. Finally, the substrates are annealed in air for one hour at 600 ^{0}C to relieve residual stress and complete the oxidation of the films..

3.2.3 MOCVD Equipment

The hot-walled reactor used consisted of a 2" (5.08 cm) diameter stainless steel tube which was put inside a resistively heated tube furnace resulting in a 30.5 cm heated zone, illustrated in Fig. 3.1. The temperature profiles for the temperature setpoints used in the deposition of lead titanate is also given in the figure. Since these films must be deposited at a reduced pressure and controlled atmosphere, a vacuum pump is employed; a liquid nitrogen cooled cold trap is used midway between the vacuum pump and reactor chamber in order to condense harmful by-products and unreacted precursor that would otherwise damage the pump.

The precursors are stored in stainless steel vacuum-sealed bubblers 1" in diameter. There are two stainless steel tubes extending from the bubbler which allow for the input of carrier gas and the output of the precursor vapor and carrier gas mixture. Dry nitrogen was used as the carrier gas and was monitored and controlled using microprocessor-controlled mass flow controllers (MFCs). Thus a constant molar flow rate of gas can be passed through the bubbler regardless of the pressure in the bubbler or reactor. The precursor is heated inside the bubbler by a custom-designed mantle heater which surrounds the entire bubbler; using microprocessor controlled temperature controllers and a thermocouple placed between the bubbler and the bubbler heater, the bubbler temperature could be maintained within 0.5 ^{0}C of the setpoint over time. The temperature inside the bubbler was determined to differ from this thermocouple reading by less than 1 ^{0}C once a steady state thermal profile develops between the bubbler and bubbler heater. The lack of thermal gradients inside the bubbler heater is a result of the excellent thermal insulating abilities of the mantle heaters.

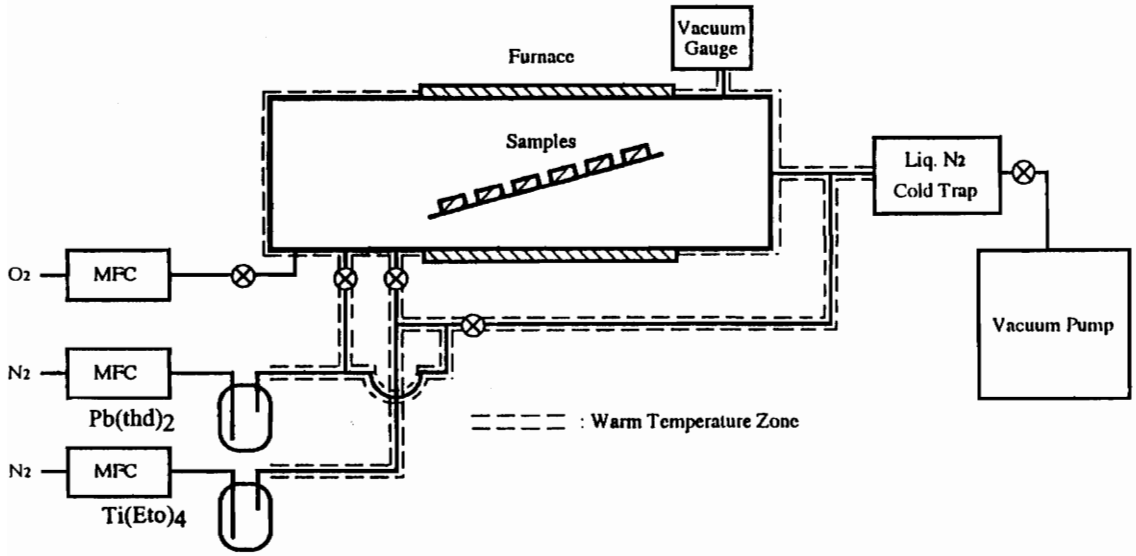

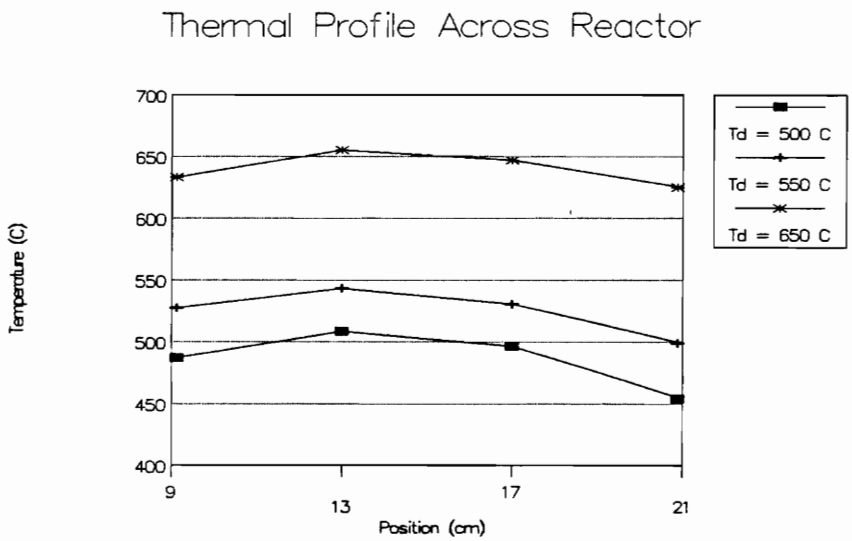

Figure 3.1: MOCVD apparatus and thermal profile for the deposition of $PbTiO_3$

Once the vapors are created inside the bubbler and transported by the carrier gas through the tubing connecting the bubblers with the reactor, it is extremely important to prevent any of the precursor from condensing before reaching the reactor. This is especially important in systems such as the one used in this investigation where the precursor partial pressures are indirectly inferred from the temperature, pressure and carrier gas flow rate inside the bubblers. For this reason, all of the tubing carrying precursor vapors and all exposed parts of the bubblers were wrapped with electric heating cords such that these parts were maintained at about 200 ^{0}C. Even a small cold spot in the tubing which results in some condensation of the precursor could have disastrous effects on the precursor partial pressure in the reactor.

In addition to tubes which deliver the precursor to the reactor for deposition, there were additional tubes installed to bypass the reactor and allow the precursor to flow directly to the cold trap. The bypass was used to allow the precursors and bubblers to reach a steady state behavior before beginning the deposition process. This has been shown to improve the compositional uniformity through the thickness of the deposited films [2].

Dry oxygen was used as the diluent gas which serves to dilute the precursor vapors as well as provide a sufficient flow velocity inside the reactor; it also serves the purpose of providing an oxidizing atmosphere thus insuring the proper oxygen stoichiometry of the films. Oxygen was monitored and controlled by means of an MFC as was the case for the carrier gases. The total pressure inside the reactor was monitored with an MKS Baratron pressure sensor and was controlled using a valve installed between the vacuum pump and the cold trap.

3.2.4 MOCVD Experimental Procedure

The MOCVD process is initiated by placing the substrates which are to be coated on an inconel susceptor and positioning the susceptor in the center of the furnace while it is still cold. The system is closed off from the atmosphere as well as the bubblers prior to pumping down the reactor to the base pressure which was typically about 0.01 to 0.02 torr. Approximately 0.85 g of fresh $Pb(thd)_2$ was then placed inside one of the bubblers and closed off from the atmosphere; it can then be opened up to the system using the bypass valve in order to remove any air and moisture from the bubbler and insure the absence of any leaks. After reclosing the valve, the same steps are repeated with the bubbler containing the titanium ethoxide. Typically, titanium ethoxide may be left inside the bubbler for ten to twenty CVD runs as long as it is always stored under vacuum; significant vapor pressures may be obtained for many runs beyond this number but the volatility and hence the vapor partial pressure obtained may not be consistent as the precursor slowly degrades. Also, it was found that prior to using the titanium ethoxide the first time it is placed in the bubbler it is necessary to allow the precursor to outgas for several hours at about 110 ^{0}C in order to remove residual ethyl alcohol in the precursor that had been used in the synthesis. All experiments were conducted with a sufficient amount of titanium ethoxide in the bubbler such that the carrier gas is always bubbling directly through the liquid. Using these precautions, it is reasonable to assume that for the given experimental arrangement, the entrance vapor partial pressures of the respective precursors are functions only of the following experimentally controlled parameters:

*Bubbler temperature

*Carrier gas flow rate

*Reactor pressure

*Dilute gas flow rate

The effects of the above parameters were discussed previously for the deposition of PbO from $Pb(thd)_2$ (see section 2.4.2). The effects of these parameters on the partial pressure of titanium ethoxide should be relatively similar to that of $Pb(thd)_2$, however, it seems that the titanium ethoxide responds much differently to changes in pressure, which will be discussed in section 3.3.1.1.

Once the titanium precursor has been allowed to outgas and has been resealed, the heating cords are turned on and liquid nitrogen is placed in the cold trap. The oxygen dilute gas is now sent through the reactor and the pressure is increased to the working pressure using the pump valve in order to maintain an oxygen environment while the substrates are being heated. The furnace is heated to the deposition temperature using a microprocessor controlled temperature controller; the thermocouple is placed between the reactor tube and the furnace; the experimental apparatus and thermal profile is given in Fig. 3.1. Substrates were placed on a tilted susceptor at positions of 9.0, 13.0, 17.0, and 21.0 cm which will be referred to subsequently as reactor position #2, #3, #4, and #5, respectively. While the furnace is heating up, the bubblers are allowed to heat up and stabilize at their respective setpoints.

Once each of the temperature setpoints have stabilized (the reactor and each of the bubblers), the MFCs controlling the individual carrier gas flow rates are turned on and the bypass valves are opened to allow the precursor vapors and carrier gas mixture to flow through the bypass. Approximately three minutes were allowed for the conditions inside the reactor and each bubbler to reach a steady state before opening the valves to the reactor and simultaneously closing the valves to the bypass.

At this point, precursor vapors are entering the beginning of the reactor tube where they are free to mix before entering the heated zone of the reactor. Upon entering

the heated zone, the precursor molecules are adsorbed and thermally decomposed on the substrate surface by a chemical process called pyrolysis; the metal or metal oxide product of the reaction is then free to migrate along the surface of the substrate or film until it forms a stable nucleus or until it can join an already existing nucleus or grain and contribute to the growth process. It is not clear at what point the oxygen is incorporated into the film, whether in the gas phase or on the surface.

Deposition was allowed to continue for 30 minutes in all experiments after which the bubblers were closed off from the reactor and the carrier gas flow was halted. All temperature controllers were turned off at this point and the oxygen dilute gas was allowed to flow for about five minutes to flush out the reactor of any residual species. Finally the dilute gas flow was shut off and the pump valve closed such that the pressure in the reactor was about 6 torr of pure oxygen. The reactor was then allowed to cool below 100 ^{0}C before removing the susceptor and coated substrates.

In order to determine the resulting thickness of the deposited films, the substrates were weighed both before and after deposition; since the films were not always transparent, it was not possible to use an optical method. A Mettler microbalance with a precision of 0.00001 g was used for the measurements. For each substrate used, a correlation factor was determined relating the surface area to the weight of the uncoated substrate assuming the thickness and density of the substrates is relatively uniform. With this information it is possible to calculate the mass flux deposition rate (g/cm^2/min) which can be converted into a thickness deposition rate (nm/min) and total film thickness (nm) assuming the density of the films is about 90%. This value for packing density turns out to be reasonable as optical properties have revealed (see section 3.3.4).

X-ray diffraction using Cu-Kα radiation was performed on all of the samples deposited in order to determine the phases present and the crystal structure of the phases.

Scanning Electron Microscopy (SEM) was used to investigate the surface morphology and Energy Dispersive Spectroscopy (EDS) was used to determine the Pb/Ti ratio of the deposited films. Optical properties of the films on sapphire were studied using reflectance and transmittance spectrophotometer on a Perkin-Elmer UV-VIS-NIR spectrophotometer.

Electrical properties on the Pt/Si and RuO_2 substrates were investigated using standard Radiant Technologies RT-66A test equipment. In order to determine electrical properties it was first necessary to sputter deposit an array of top electrodes composed of ruthenium oxide. These "top" electrodes consist of small circular areas of ruthenium oxide approximately 0.016 cm in diameter and 300 to 400 nm thick. By scratching through the film it is then possible to attach probes to both the top and bottom electrodes for making measurements.

3.3 Results and Discussion

3.3.1 Effect of Process Parameters on Film Structure, Thickness and Composition

3.3.1.1 Thickness, Composition, and XRD Results

By a largely trial and error process, it was found that reproducible lead titanate films of excellent composition and structure which were optically specular and transparent could be produced using a deposition temperature, T_d, of 550 ^{0}C and the following experimental parameters:

TABLE 3.1: Optimum $PbTiO_3$ MOCVD Parameters for T_d = 550 ^{0}C

Total Pressure, p	6 torr
Dilute Gas Flow Rate, f_{o2}	550 sccm
Ti Bubbler Temp., $T_{b,\ TiO2}$	114 ^{0}C
Pb Bubbler Temp., $T_{b,\ Pb}$	140 ^{0}C
Pb Carrier Gas Flow Rate, $f_{N2,\ Pb}$	50 sccm
Ti Carrier Gas Flow Rate, $f_{N2,\ Ti}$	5 sccm

However, once these guidelines were established I intended to examine how important and what effects result from slight changes in the various experimental parameters regarding the composition, deposition rate (thickness) and crystal structure. Consequently, I will treat each parameter that has been examined separately and discuss the effect of that parameter on the structure and composition together.

Figures 3.2 and 3.3 show the composition profile and thickness profiles at four different positions in the reactor for lead bubbler temperatures of 136 ^{0}C and 140 ^{0}C, respectively; the titanium bubbler temperature is 98 ^{0}C for both sets of data; all other deposition parameters are the same and are given within the figure. As can be seen in the figures, the composition profile goes from being uniformly stoichiometric across the entire hot zone to extremely Pb-rich, especially close to the entrance. The XRD patterns for the corresponding films are given in Figs. 3.4 and 3.5. It is interesting to note that although EDS measurements show that the films deposited with $T_{b,\ Pb}$ = 136 ^{0}C are nearly perfectly stoichiometric, the XRD patterns reveal the presence of some unreacted lead oxide in the from of massicot, which is especially noticeable on the sample deposited in position #2 (Fig. 3.4). This was typically found to be the case for samples placed at this

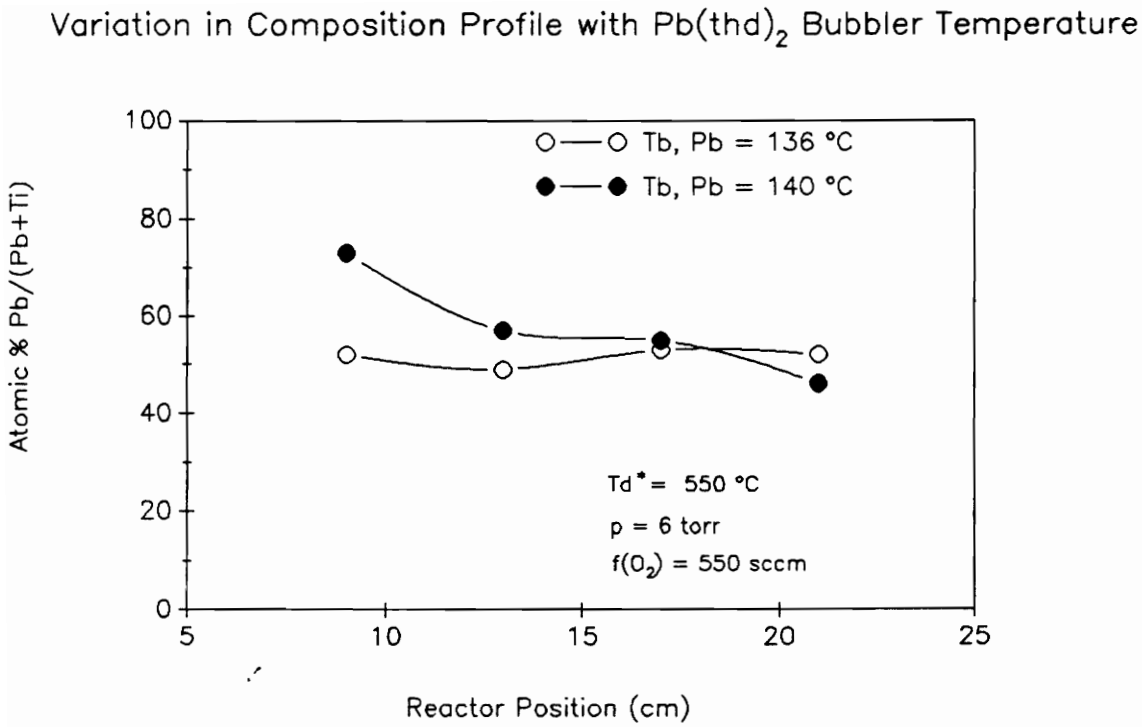

Figure 3.2: Variation in the composition profile with the lead bubbler temperature; the titanium bubbler temperature is fixed at 98 ^{0}C

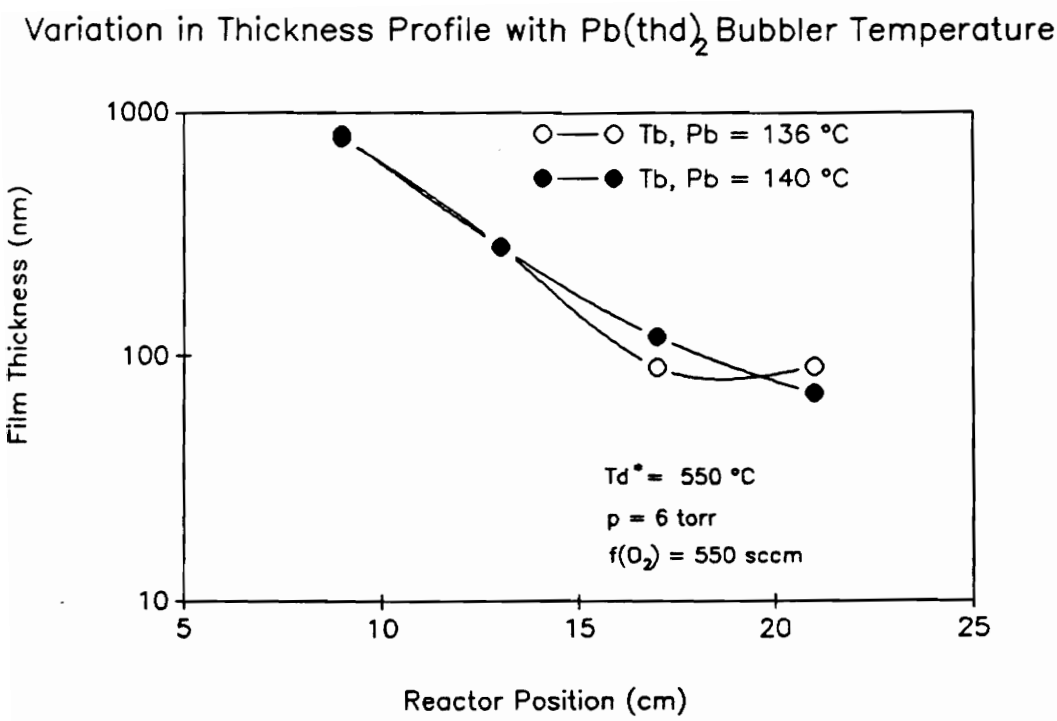

Figure 3.3: Variation in the thickness profile with the lead bubbler temperature; the titanium bubbler temperature is fixed at 98 ^{0}C

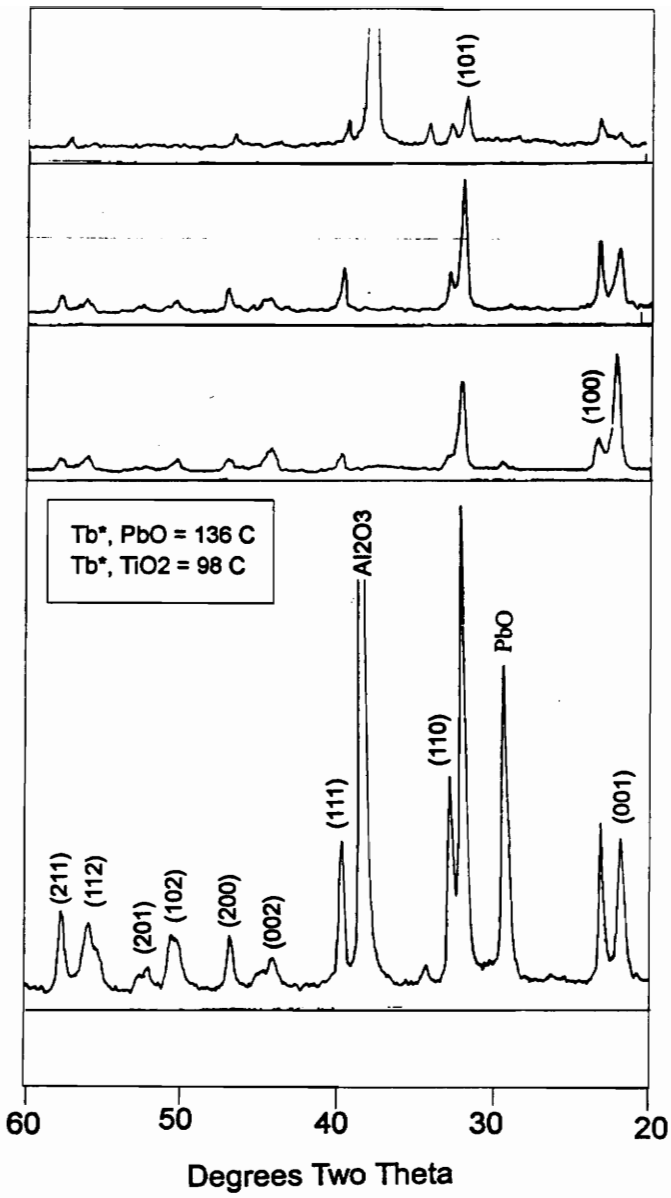

Figure 3.4: XRD pattern for $T_{b,\ Pb}$ = 136 ^{0}C in Figs. 3.2 and 3.3

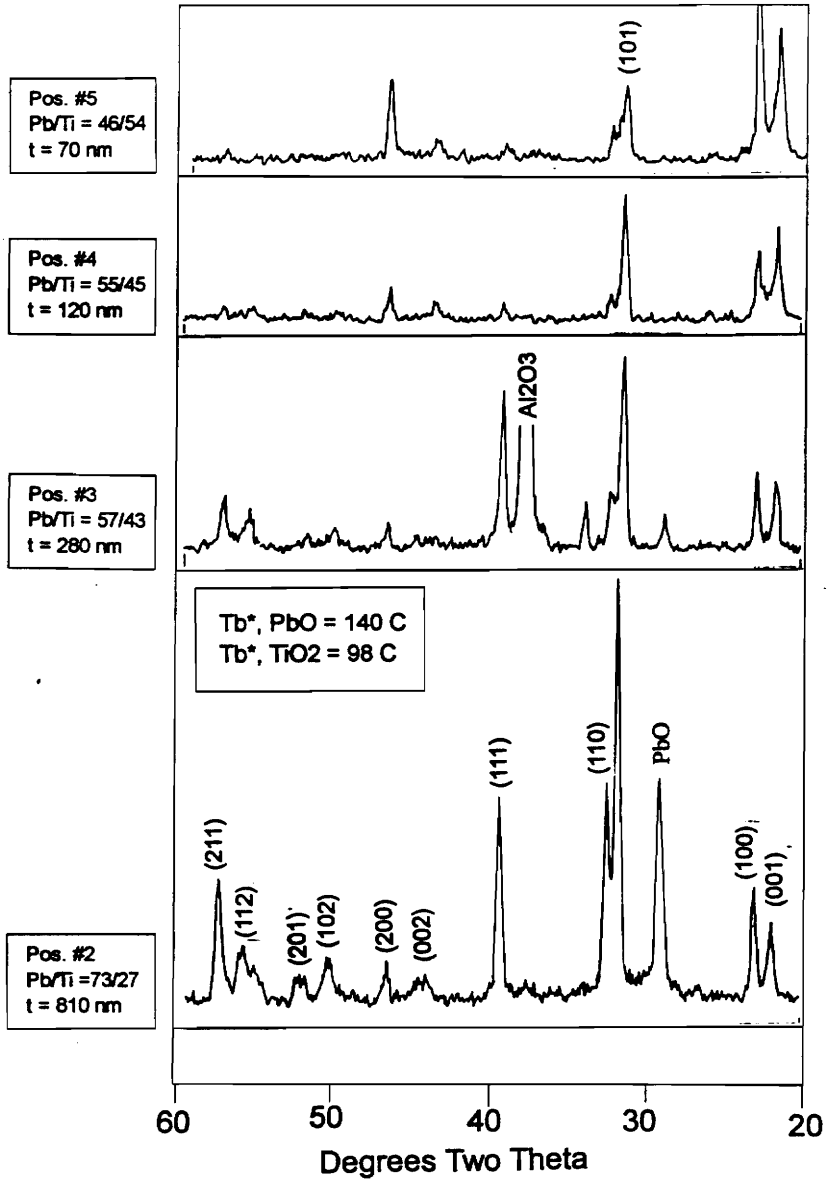

Figure 3.5: XRD pattern for $T_{b,\,Pb}$ = 140 ^{0}C in Figs. 3.2 and 3.3

position in the reactor where the local deposition rate can exceed 30 nm/min. Samples at positions further along in the reactor were generally fully reacted since the deposition rate in those regions was generally less than 20 nm/min. The existence of unreacted PbO in films that are stoichiometric overall provides evidence that the individual oxides, PbO and TiO_2 are deposited separately and subsequently react on the substrate surface to produce $PbTiO_3$. Hence, at very high deposition rates of the individual oxides, the formation rate of lead titanate is limited by the reaction rate of the constituent oxides:

$$PbO + TiO_2 \rightarrow PbTiO_3$$

In Figures 3.6 and 3.7 the variation in deposition rate profile and composition profile are examined for three different titanium bubbler temperatures. XRD patterns are given in Figs. 3.8, 3.9, 3.10, and 3.11. It is interesting to note that by varying the titanium bubbler temperature by only 4 ^{0}C we can change the average overall film composition by between 5 and 10 total % which corresponds to a change in the deposition rate of any single component by as much as 50%. Clearly, the titanium bubbler temperature is more important than any other single factor in controlling the film composition at the temperature studied. Using a titanium bubbler temperature of 112 ^{0}C gives the best composition profile but unfortunately there is still considerable unreacted PbO for the sample in position #2. For this reason it is suggested that at the deposition temperature, T_d, of 550 ^{0}C the deposition rate should probably be restricted to 20 nm/min or less. When $T_{b,\ TiO2}$ is raised to 114 ^{0}C, no excess PbO is observed regardless of the deposition rate. By raising the bubbler temperature only two more degrees to 116 ^{0}C the films were found to be completely amorphous as evidenced by the lack of XRD peaks; instead a very broad region of scattered x-rays occurs between $2\Theta = 25^0$ to 33^0. The composition of

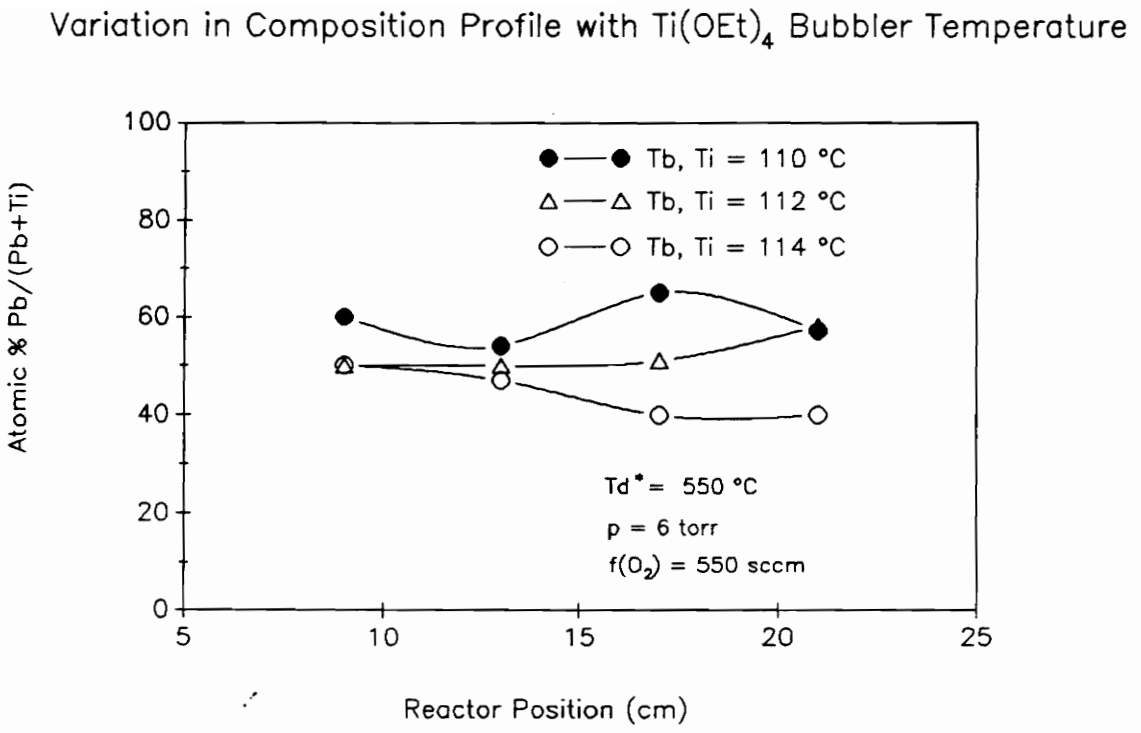

Figure 3.6: Variation in the composition profile with the titanium bubbler temperature; the lead bubbler temperature is fixed at 140 ^{0}C

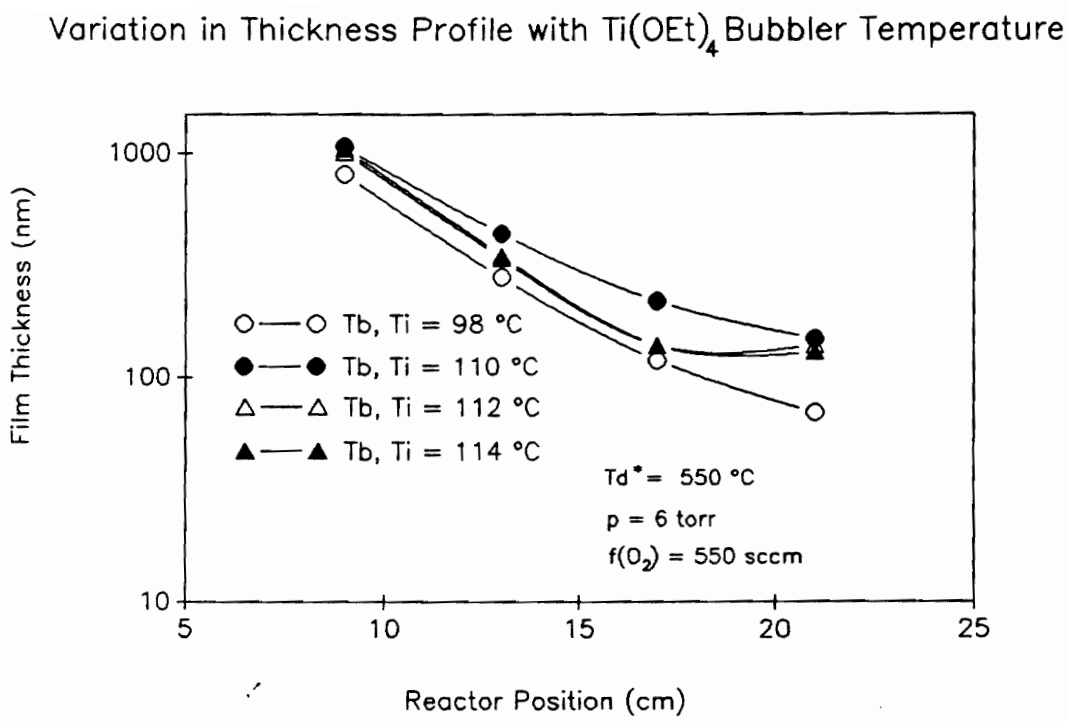

Figure 3.7: Variation in the thickness profile with the titanium bubbler temperature; the lead bubbler temperature is fixed at 140 ^{0}C

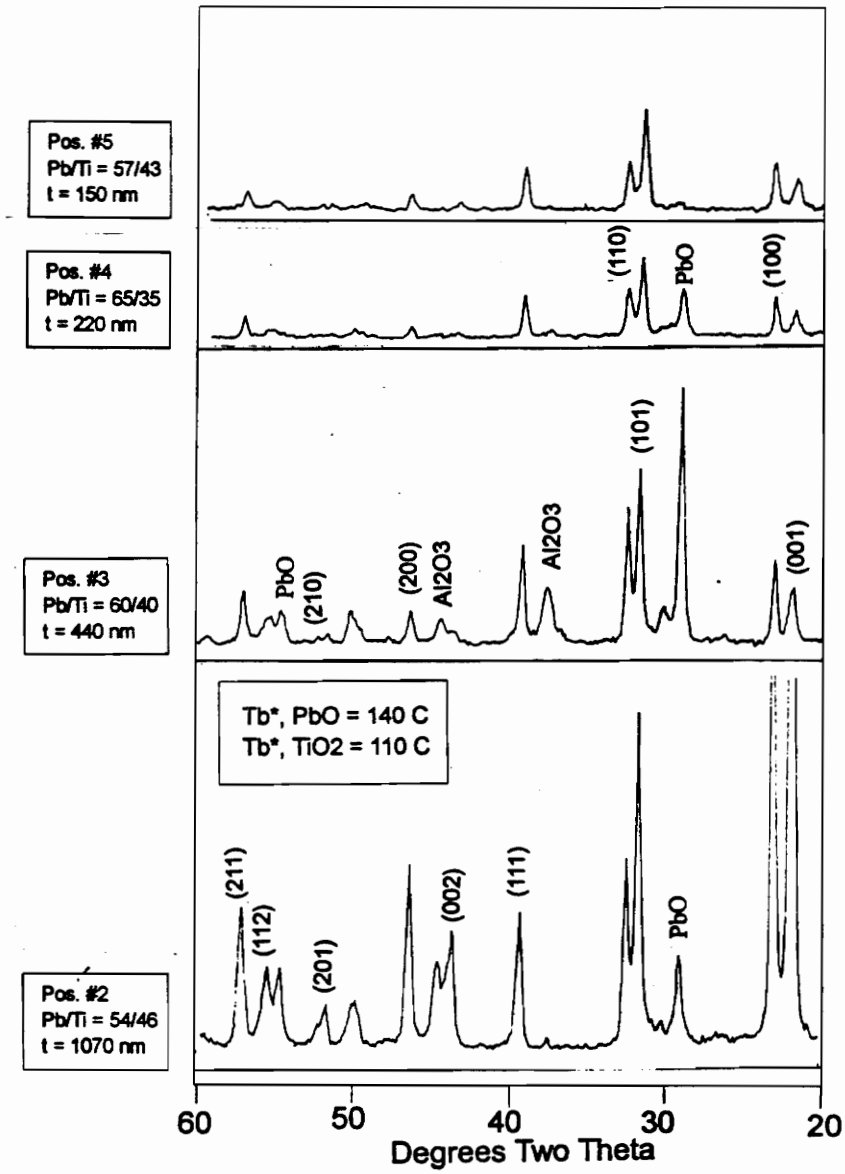

Figure 3.8: XRD pattern for $T_{b,\ Ti}$ = 110 ^{0}C in Figs. 3.6 and 3.7

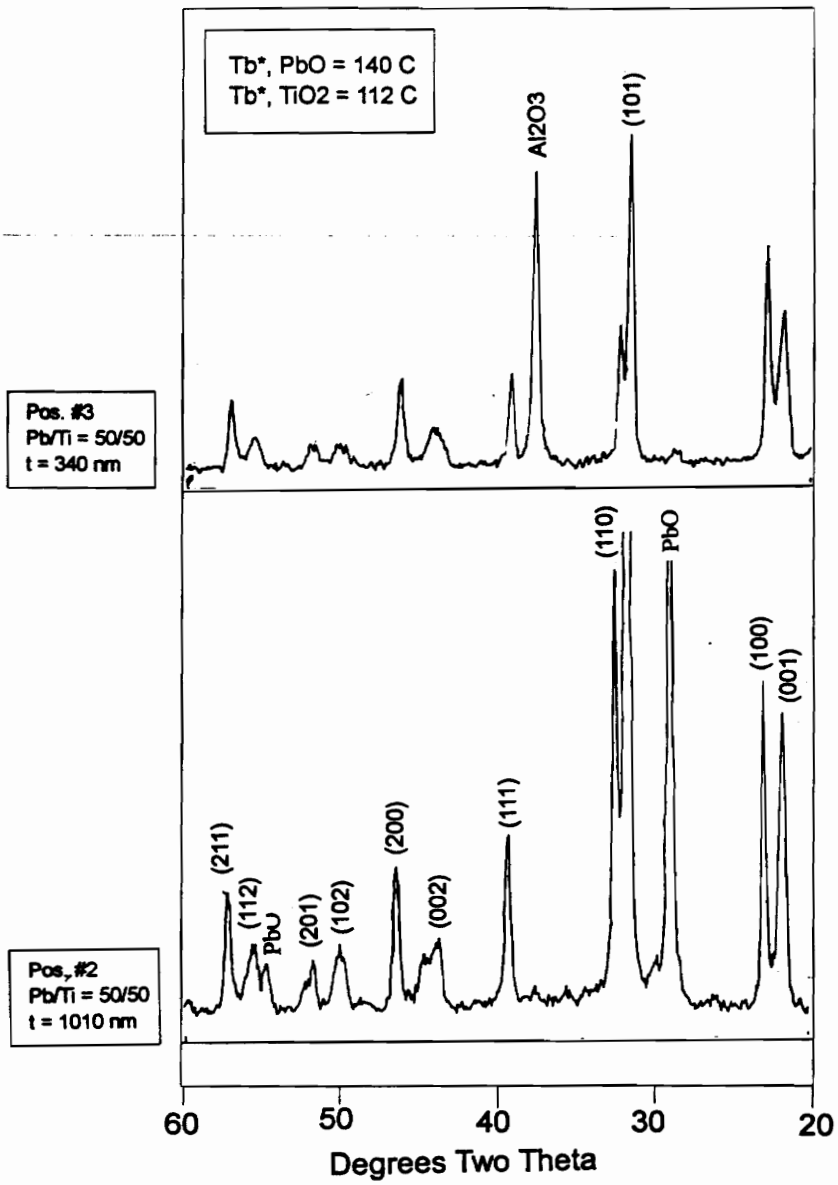

Figure 3.9: XRD pattern for $T_{b,\ Ti}$ = 112 ^{0}C in Figs. 3.6 and 3.7

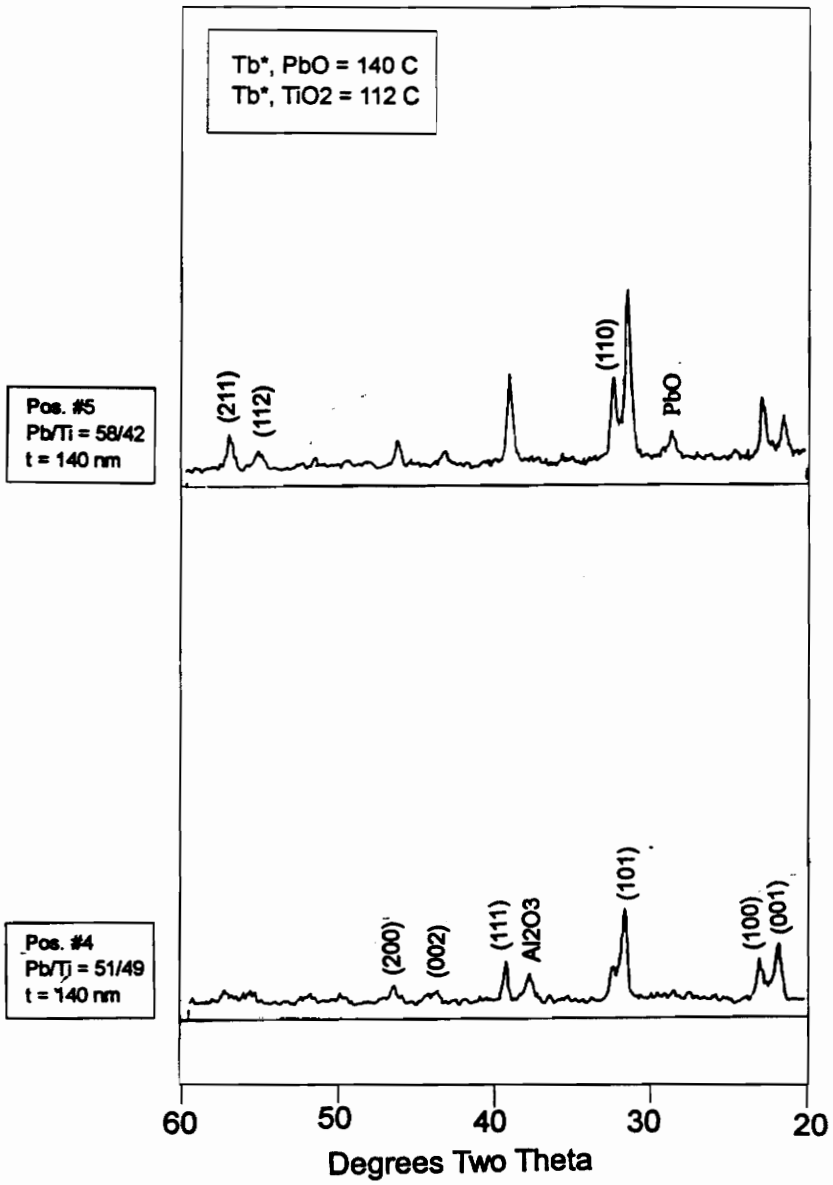

Figure 3.9: (Continued)

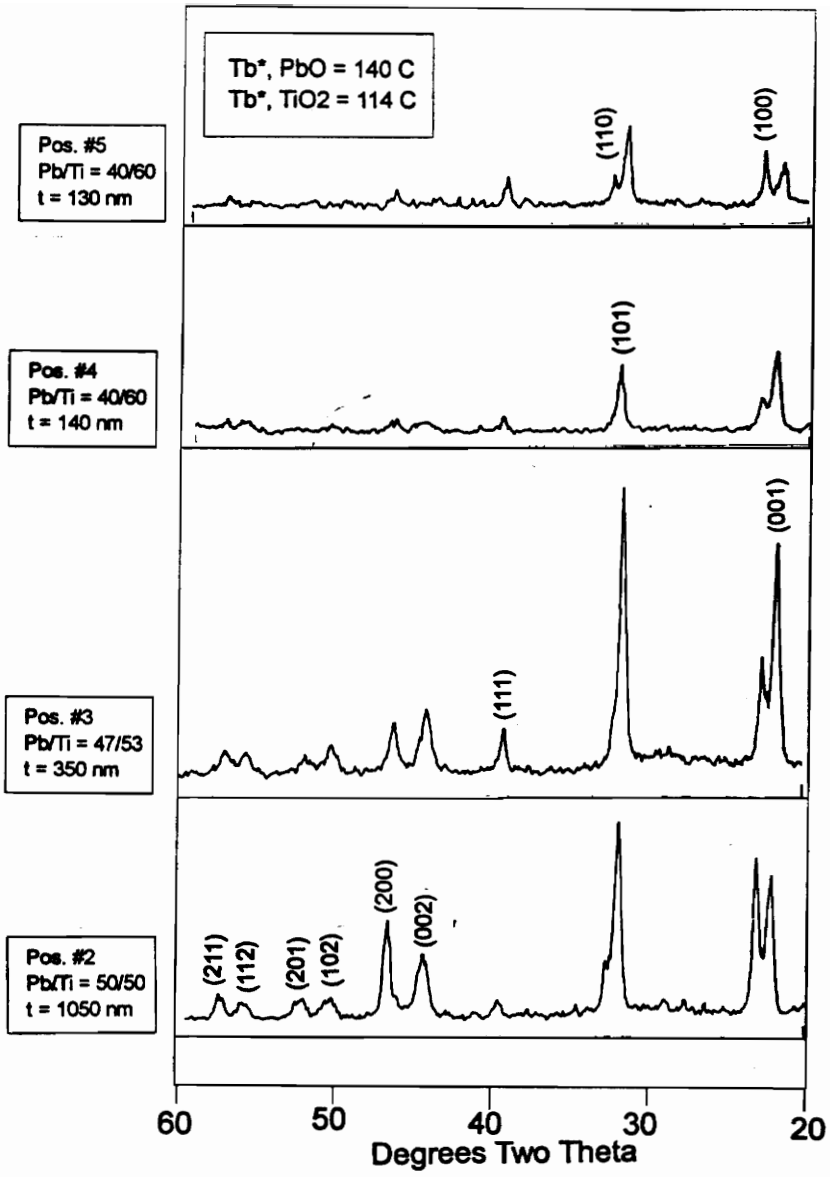

Figure 3.10: XRD pattern for $T_{b,\ Ti}$ = 114 ^{0}C in Figs. 3.6 and 3.7

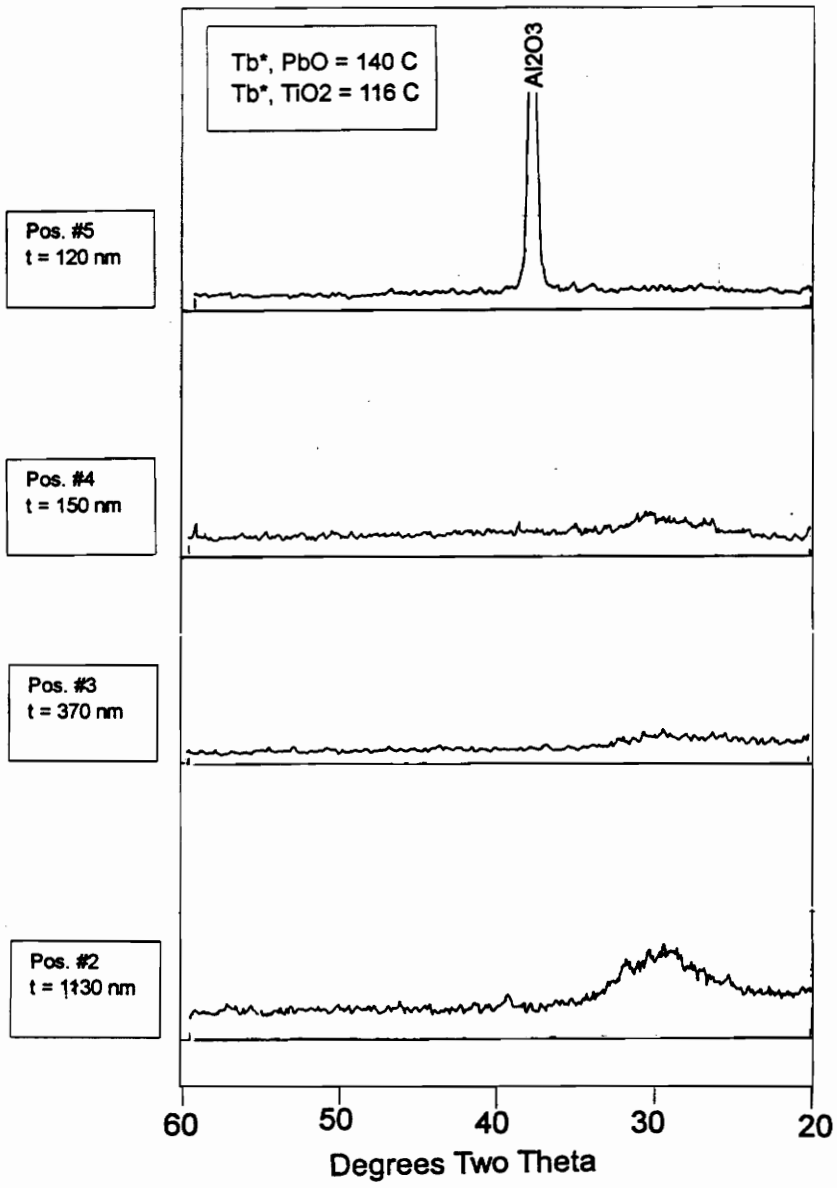

Figure 3.11: XRD pattern for $T_{b,\ Ti}$ = 116 ^{0}C in Figs. 3.6 and 3.7

these film was found to lie between 30% and 40% lead. Typically, any film which was found to have less than about 40% PbO was found to be completely amorphous. At PbO percentages between 40% and 50% $PbTiO_3$ perovskite peaks could be observed but were considerably reduced in intensity indicating that the film may contain regions of amorphous material. Only very rarely could small rutile (TiO_2) peaks be observed.

While the depositions described previously were all conducted at a total pressure of 6 torr, the effect of total pressure was investigated by depositing at p = 4 torr and p = 8 torr using conditions for which favorable results were obtained at 6 torr. These results are given for the composition profile, thickness profile and various XRD patterns in Figures 3.12, 3.13, 3.14, and 3.15. The deposition rate was strongly affected, as expected, but the trend was in the opposite direction to what would have been expected intuitively. The deposition rate was found to increase by as much as four times by decreasing the pressure from 8 torr to 4 torr, with the deposition rate profiles for 6 torr intermediate between the other two. The clue to explaining this behavior lies in the XRD and composition profiles for each set of data. On going from 4 torr to 6 torr and then 8 torr, the composition goes from being Ti-rich to stoichiometric and finally becomes Ti-deficient. Thus, the titanium deposition rate seems to be controlling the overall deposition rate to a large degree. The most probable explanation is the fact that the titanium vaporization rate is extremely sensitive to the total pressure in the bubbler which is generally quite close to the total pressure in the reactor. This is not surprising since 114 ^{0}C is quite close to the boiling point of 122 ^{0}C for titanium ethoxide.

For the samples deposited at 4 torr, the titanium oxide deposition rate was extremely high; typically films with such a high titanium deposition rate become dark black or brown in color which is indicative of the monoxide form of titanium (TiO), as was the case for these samples. In such regimes, the titanium ethoxide decomposition

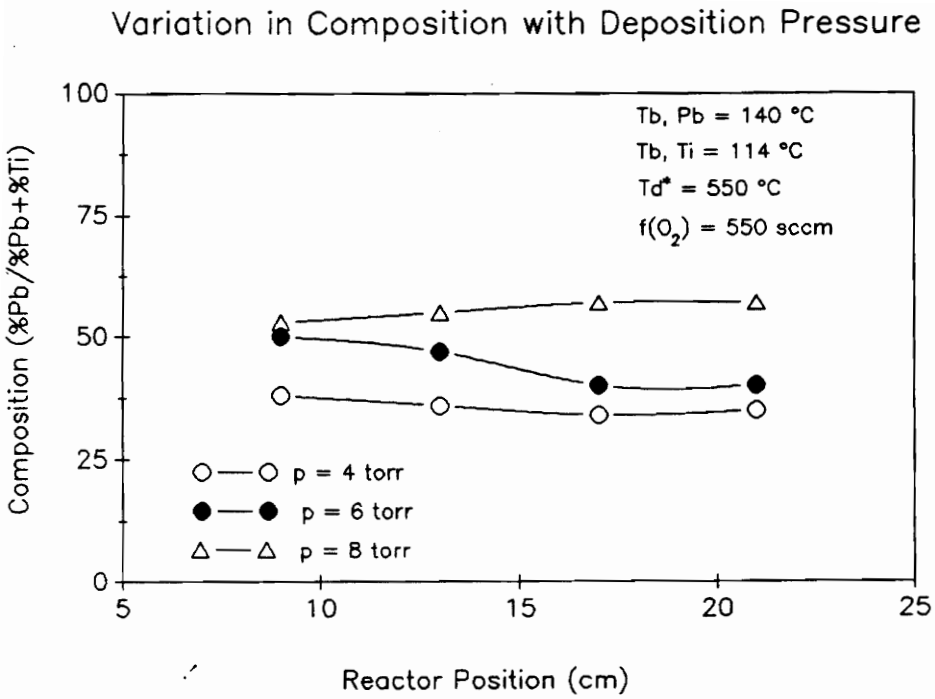

Figure 3.12: Variation in the composition profile with the deposition pressure

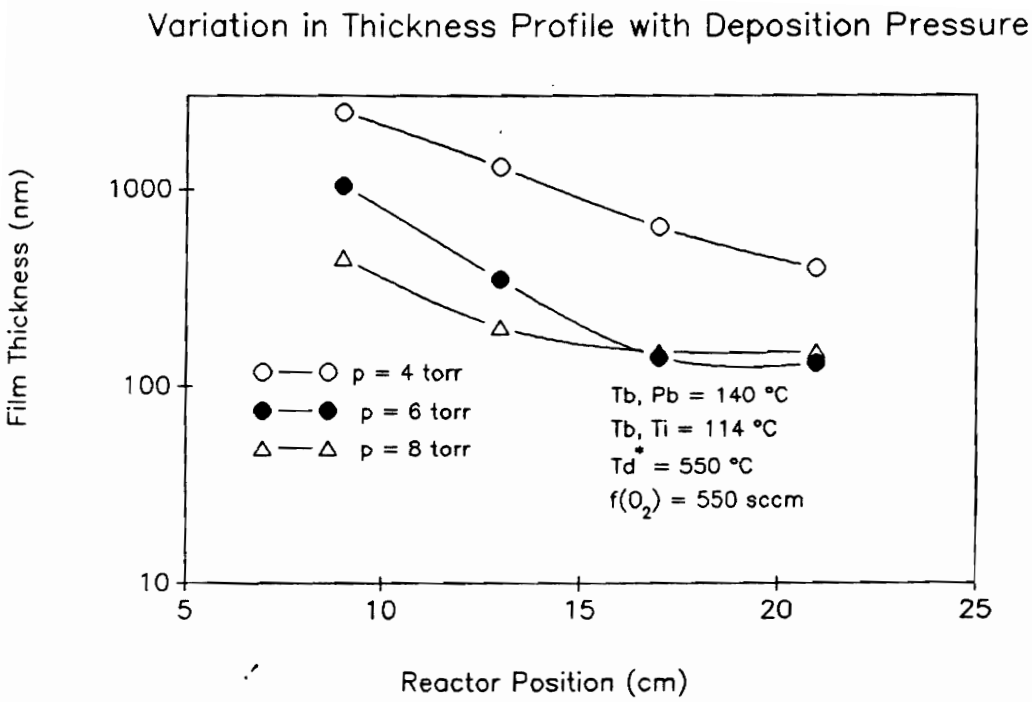

Figure 3.13: Variation in the thickness profile with the deposition pressure

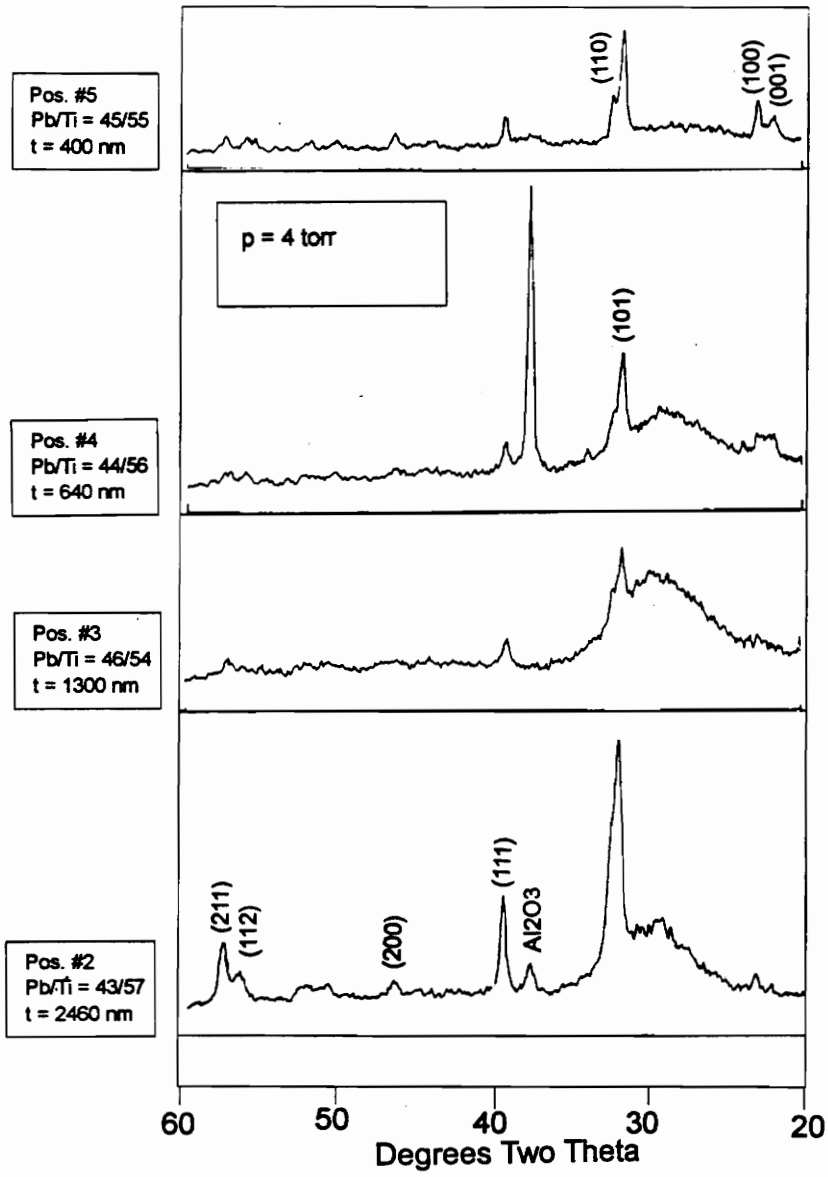

Figure 3.14: XRD pattern for p = 4 torr in Figs. 3.12 and 3.13

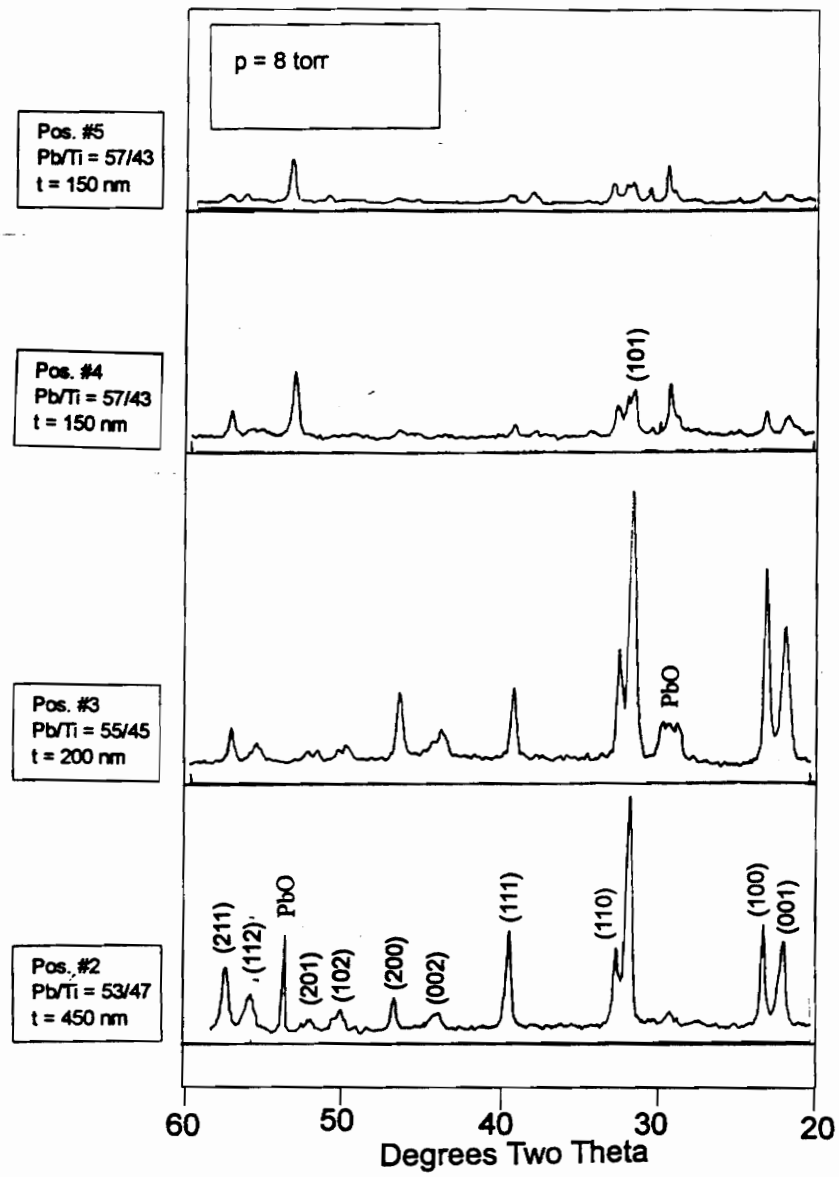

Figure 3.15: XRD pattern for p = 8 torr in Figs. 3.12 and 3.13

product which is not completely oxidized, perhaps TiO, deposits at a rate faster than the oxidation rate which consequently makes it the rate limiting step:

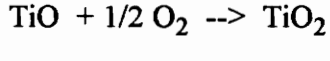

$$TiO + 1/2\ O_2 \rightarrow TiO_2$$

3.3.1.2 Surface Morphology

Typical surface morphologies for $PbTiO_3$ films grown on sapphire and ruthenium oxide are given in Figs. 3.16 and 3.17 deposited according to the conditions in Table 3.1. The films deposited at this temperature (550 ^{0}C) are generally smooth and fine grained and appeared mirror-like and transparent to the eye. The microstructure of the lead titanate on platinum (not shown) was found to be nearly identical to that of ruthenium oxide, but a slight amount of faceting can be observed in the micrograph of the film on sapphire for position #2 (Fig. 3.16).

3.3.1.3 Use of High Temperature Deposition Regime for Improved Composition Control

It was previously shown that the deposition behavior, especially regarding the composition of the films, is extremely sensitive to the experimental parameters at a deposition temperature of 550 ^{0}C as a consequence of the resulting variability of the composition of the gas stream. However, in a paper by de Keijser, et al., 1991 [25], it was shown that for the MOCVD of lead zirconate titanate (PZT), as the deposition temperature is increased to 600 ^{0}C, a process window develops where a range of gas stream compositions will result in stoichiometric PZT. For PZT, stoichiometric is defined

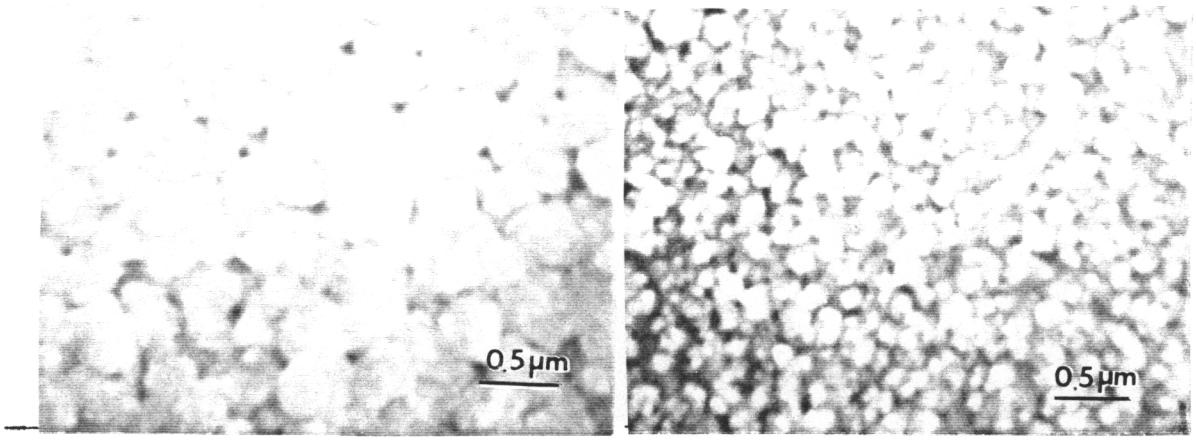

x = 9.0 cm

x = 13.0 cm

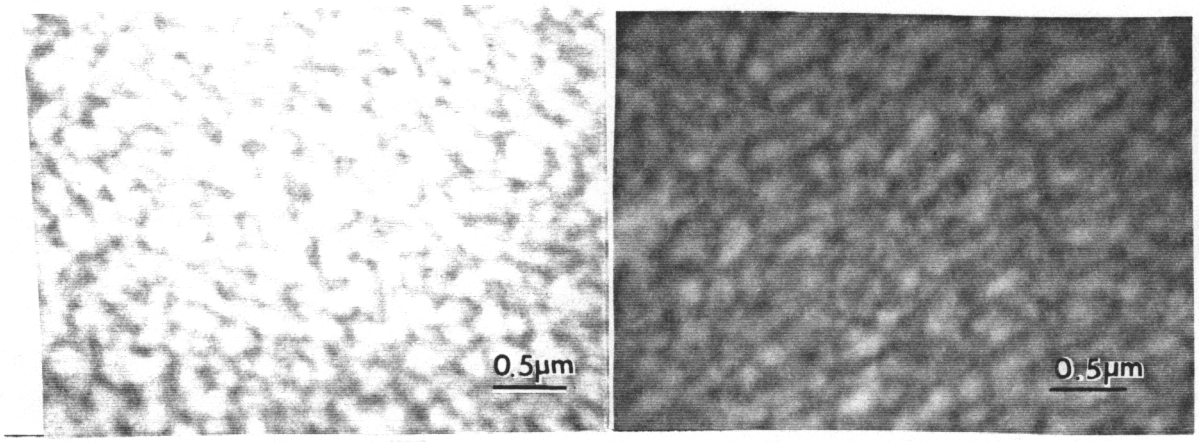

x = 17.0 cm

x = 21.0 cm

Figure 3.16: SEM micrographs of $PbTiO_3$ on sapphire for $T_d = 550\ ^0C$

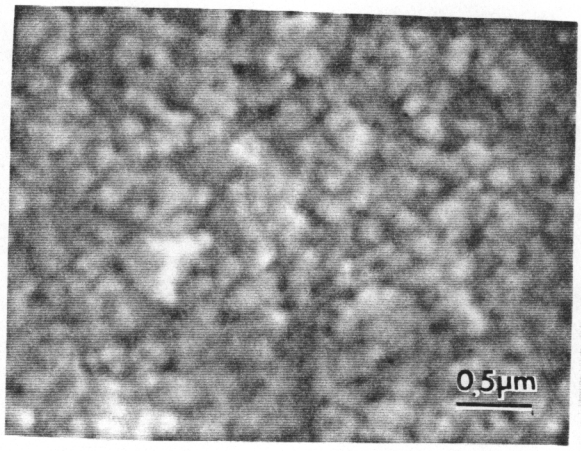

x = 9.0 cm

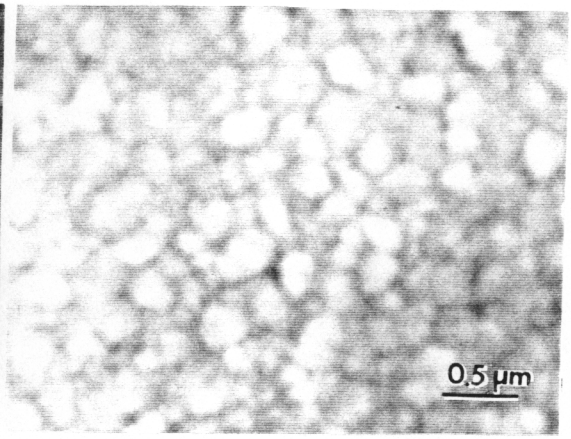

x = 13.0 cm

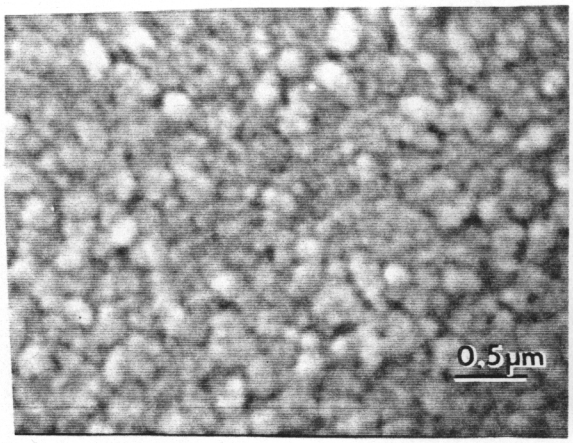

x = 17.0 cm

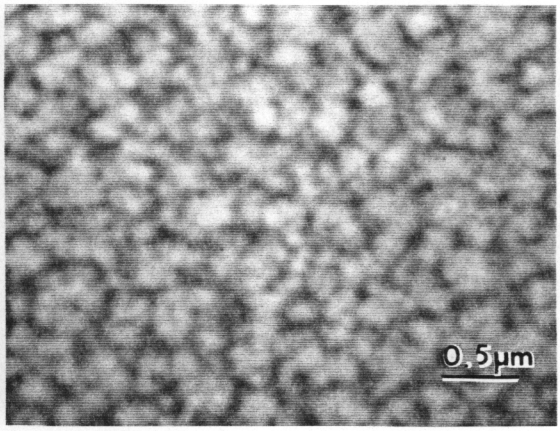

x = 21.0 cm

Figure 3.17: SEM micrographs of $PbTiO_3$ on RuO_2 for $T_d = 550\ ^0C$

as having the ratio of A-site cations to B-site cations equal to 1:1; in other words, the films are 50 mol% PbO; oxygen is assumed to exist in the proper ratio as is generally the case for reasonably low deposition rates. As the deposition temperature was increased, the width of the process window was found to increase, i.e. the sensitivity to gas stream composition is considerably reduced.

The existence of a process window was confirmed for lead titanate also in the hot-walled reactor used in this study. $PbTiO_3$ was deposited on sapphire using a lead bubbler temperature of 150 ^{0}C and a titanium bubbler temperature of 115 ^{0}C. The reactor temperature was increased to 650 ^{0}C and the oxygen diluent gas flow rate was increased to 850 sccm to account for the higher depletion rate at the higher temperature. Each of the three samples were placed in the reactor at different positions and hence different temperatures, yet each was found to contain exactly 50% PbO and 50% TiO_2 within the experimental accuracy of the EDS detector as can be seen in Fig. 3.18. The only effect, which can be seen in Fig. 3.19, is a substantial increase in the deposition rate. To confirm that the process is insensitive to disturbances in the experimental conditions, the titanium bubbler temperature was increased to 120 ^{0}C, an increase of 5 ^{0}C, which is more than the entire range of titanium bubbler temperatures studied previously; these films were also found to be nearly stoichiometric as was seen in Fig. 3.18. Consequently, it can be concluded that the main effect of increasing the titanium ethoxide partial pressure by increasing the titanium bubbler temperature is to increase the overall deposition rate while leaving the composition unchanged. The XRD patterns for these films deposited at the high temperature are given in Figs. 3.20, 3.21, and 3.22. Only in position #2, where the temperature is relatively low and the deposition rate is very high was any excess PbO phase observed in the XRD patterns.

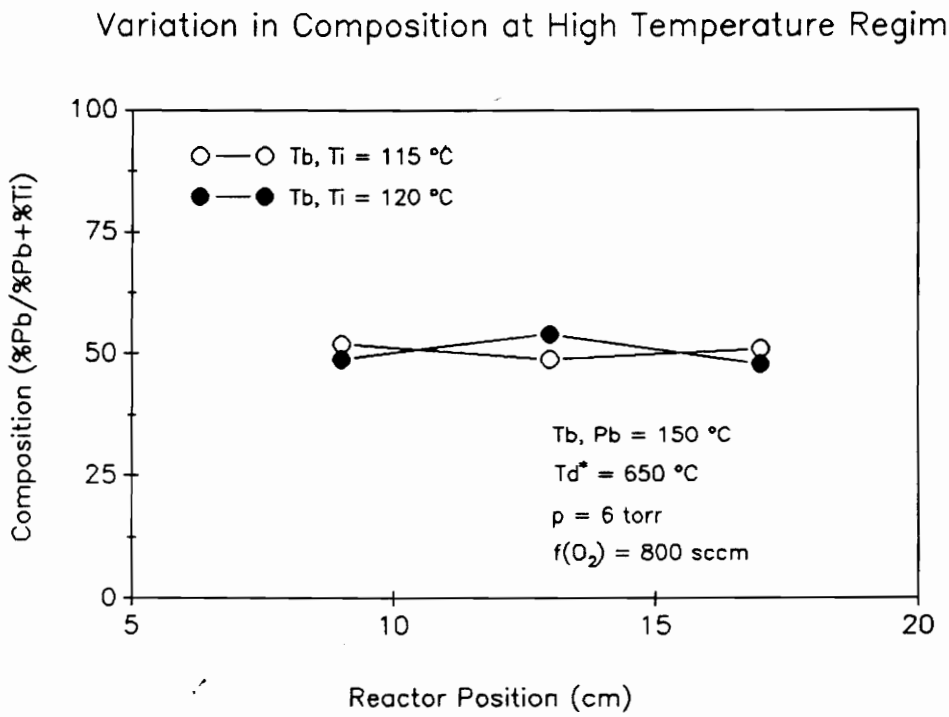

Figure 3.18: Variation in the composition profile at the high temperature regime

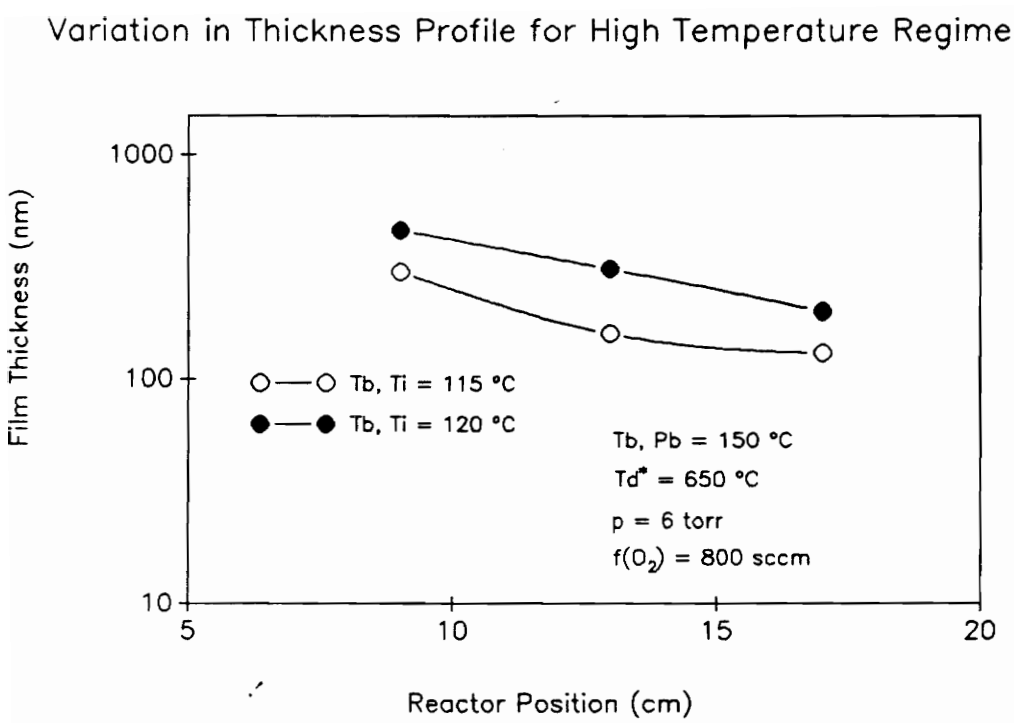

Figure 3.19: Variation in the thickness profile at the high temperature regime

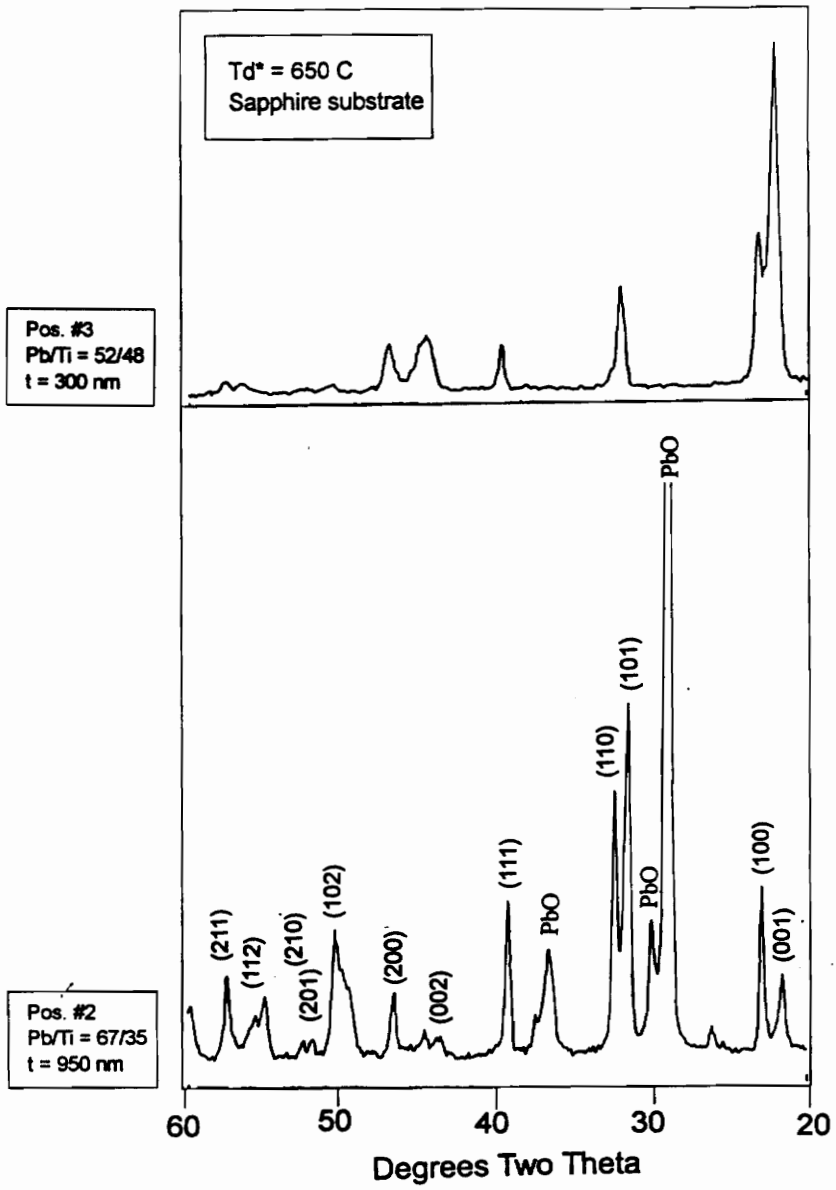

Figure 3.20: XRD pattern for $T_{b,\ Ti}$ = 115 ^{0}C, $T_{b,\ Pb}$ = 150 ^{0}C deposited at T_d = 650 ^{0}C on sapphire

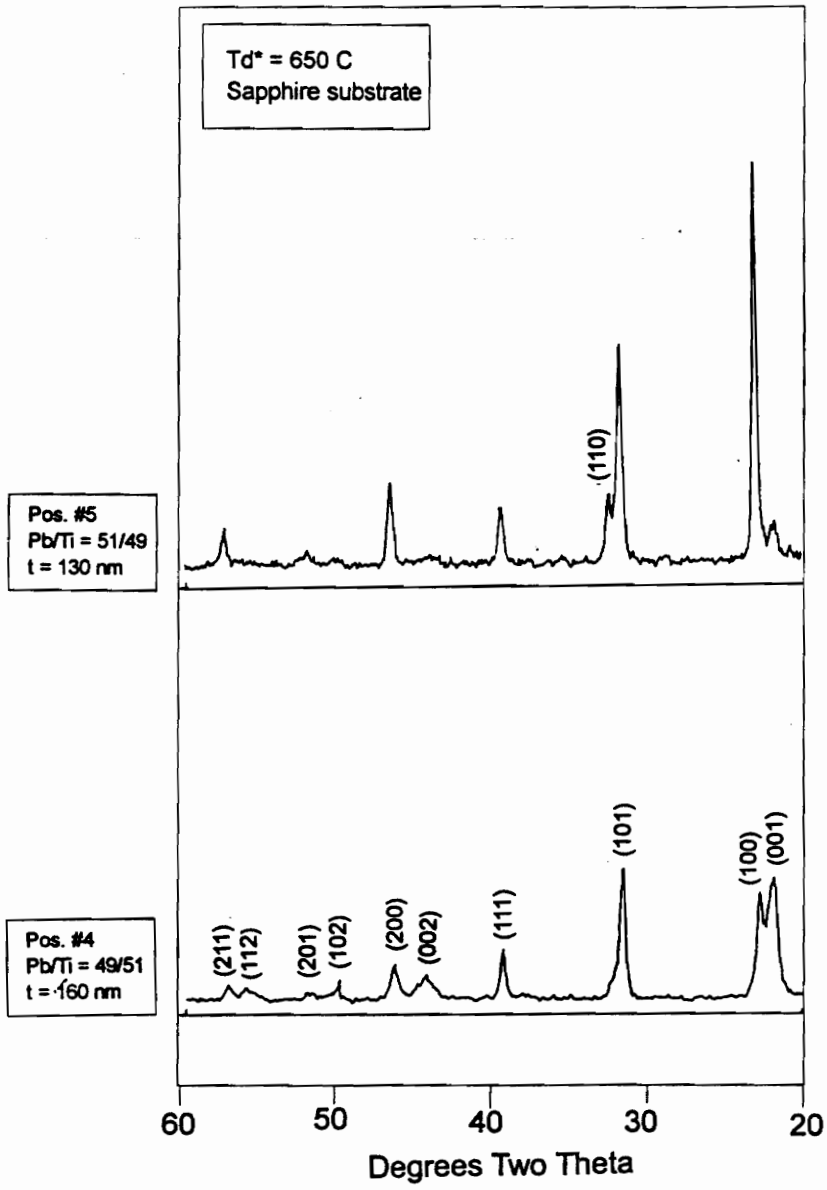

Figure 3.20: (Continued)

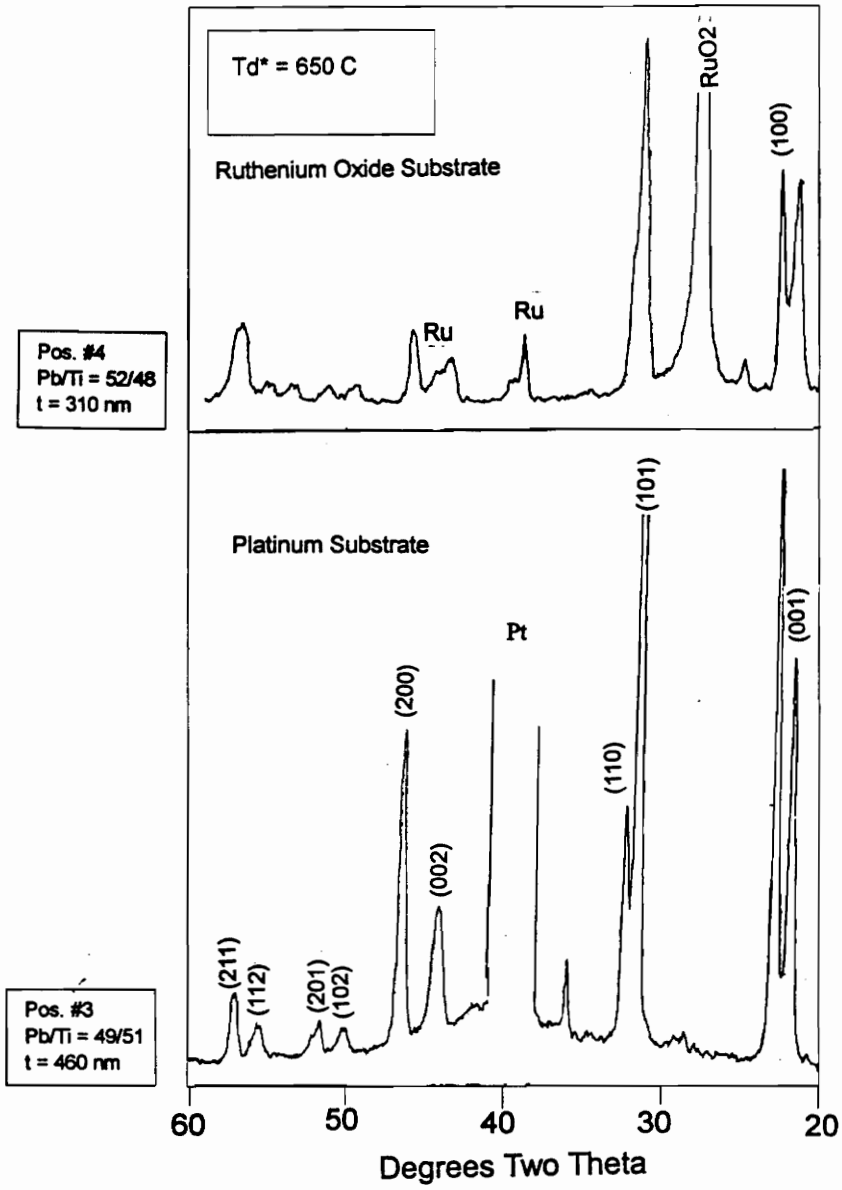

Figure 3.21: XRD pattern for $T_{b,\,Ti}$ = 120 ^{0}C, $T_{b,\,Pb}$ = 150 ^{0}C deposited at T_d = 650 ^{0}C on RuO_2 and Pt

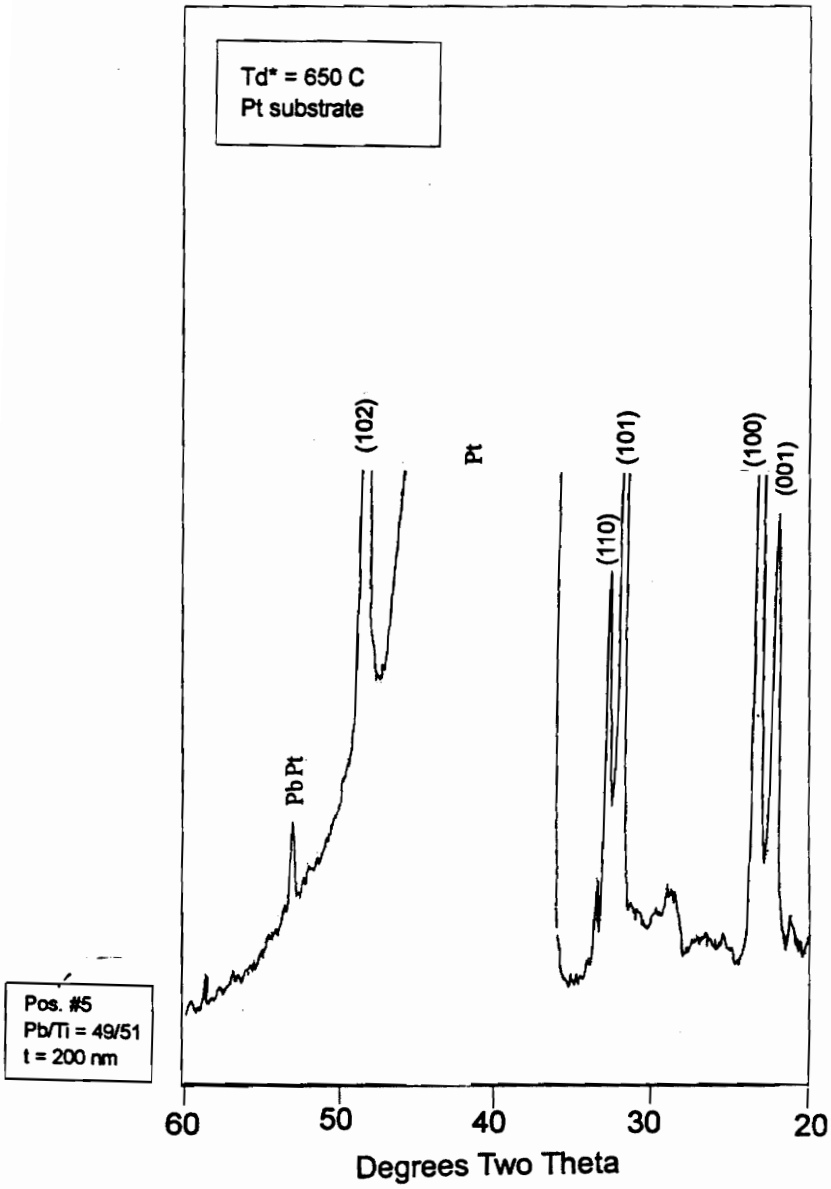

Figure 3.21: (Continued)

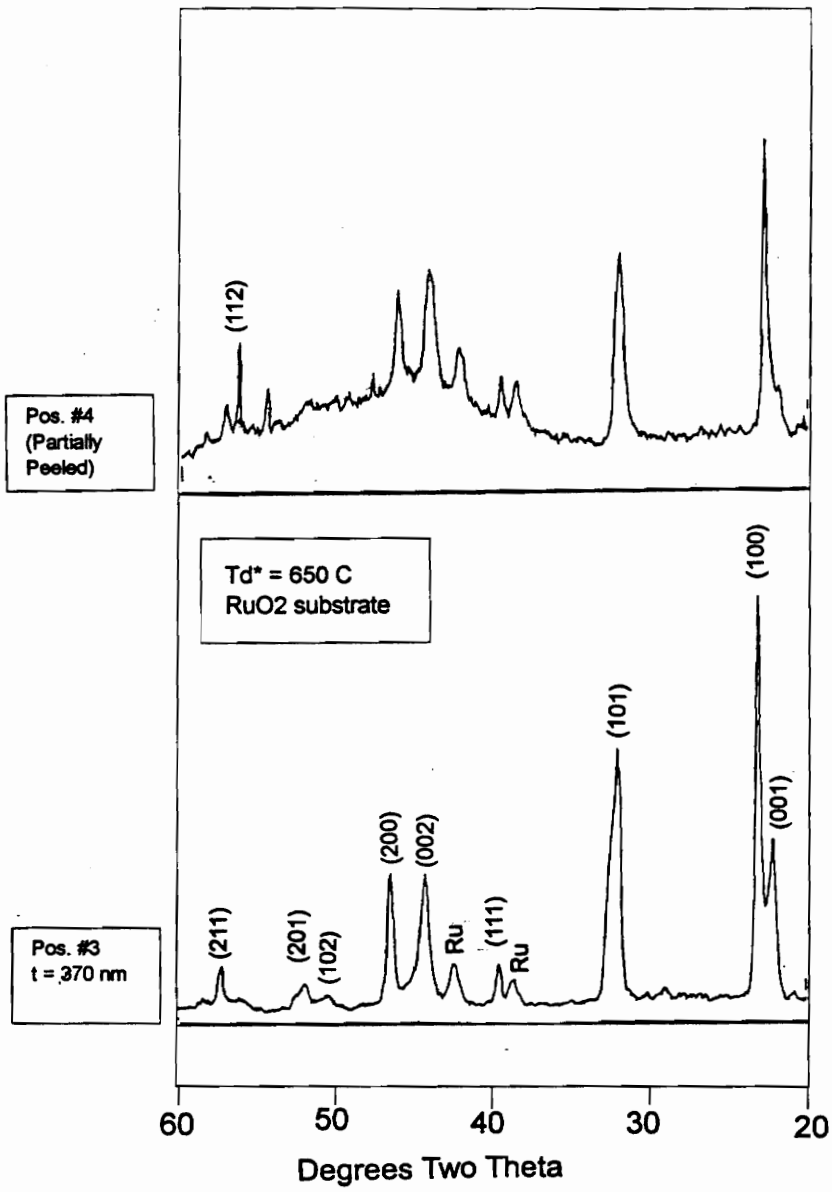

Figure 3.22: XRD pattern for $T_{b,\ Ti}$ = 120 ^{0}C, $T_{b,\ Pb}$ = 150 ^{0}C deposited at T_d = 650 ^{0}C on RuO_2

The surface morphology of the films deposited at this temperature shows an extremely fine-grained microstructure characteristic of a high nucleation rate resulting from the increased deposition temperature (Fig. 3.23). In addition, UV-VIS-NIR spectrophotometry was used in specular transmission mode and specular reflectance mode to obtain the spectra shown in Fig. 3.24. Although these films are too thin to accurately obtain optical constants, the extremely close approach of the maxima in the interference fringes on the transmission spectra to the transmission spectra of the uncoated sapphire is strong evidence of the highly transparent, specular and non-absorbing nature of these films deposited at 650 ^{0}C. The fact that the scattering from these films is so low is probably a result of the extremely fine grain structure of the films which are two small to effectively scatter in the visible range of wavelengths.

The process window exists for the CVD of these lead-based compounds because PbO is much more volatile than the lead titanate or PZT, especially as the temperature exceeds 600 ^{0}C as can be seen in Fig. 3.25. As long as a sufficient quantity of lead precursor is available such that PbO deposits in excess of that required to form the stoichiometric compound, any excess PbO that is deposited is desorbed before it can be incorporated into the film. Thus, only the PbO that actually reacts with the TiO_2 to form $PbTiO_3$ will actually be incorporated into the film. Although it has not been shown, it is suspected that this self-limiting behavior will not occur for extremely high deposition rates as the PbO will not have sufficient time to desorb before the film begins to grow over it.

3.3.2 Post-Deposition Annealing Behavior

For processes which are to be integrated into the overall microelectronics fabrication process, it is generally desirable that the maximum processing temperature be

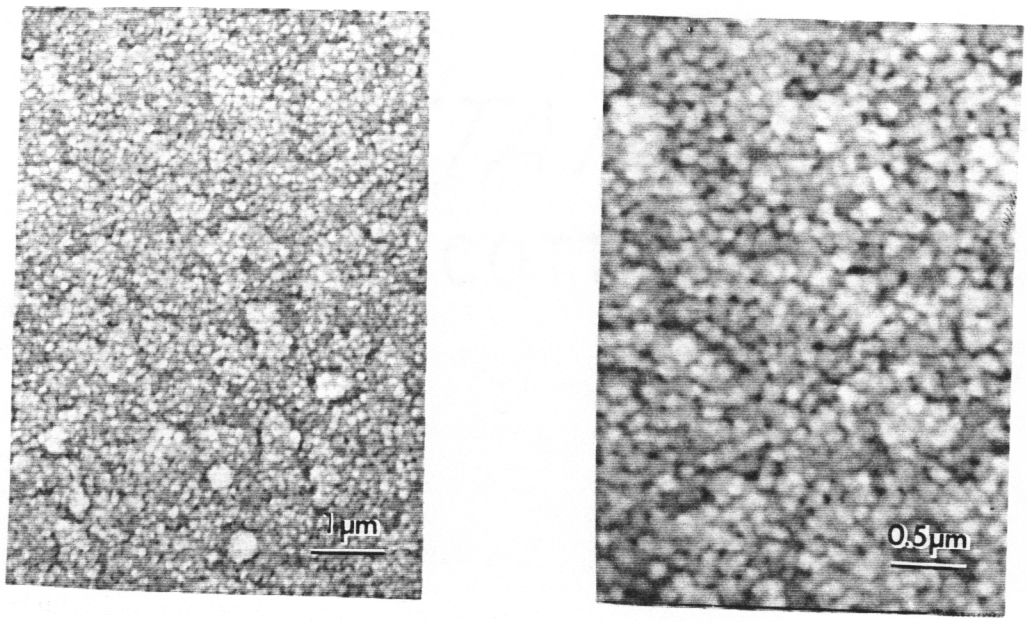

Figure 3.23: SEM micrograph of $PbTiO_3$ films deposited on Pt at 650 ^0C

(a)

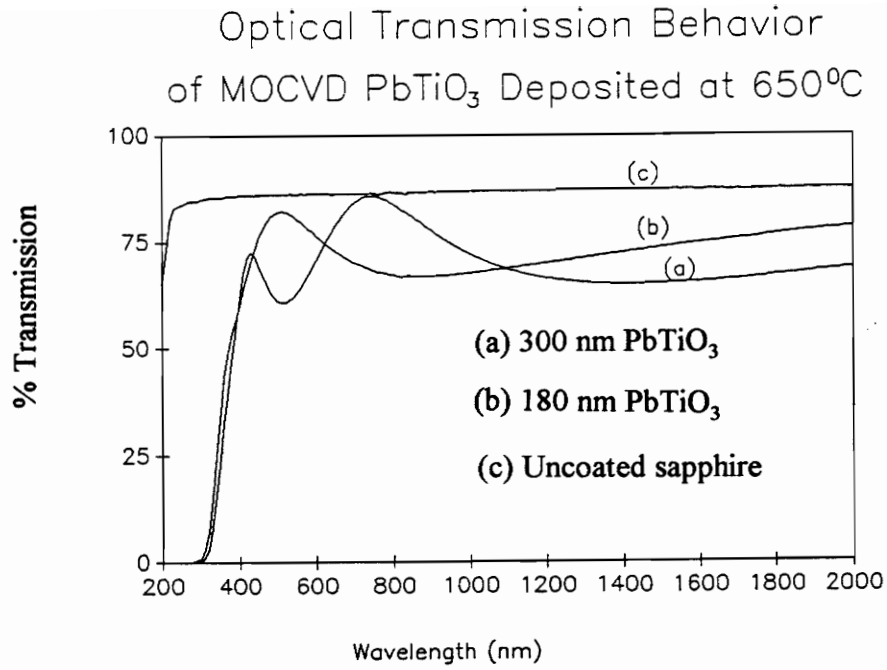

(b)

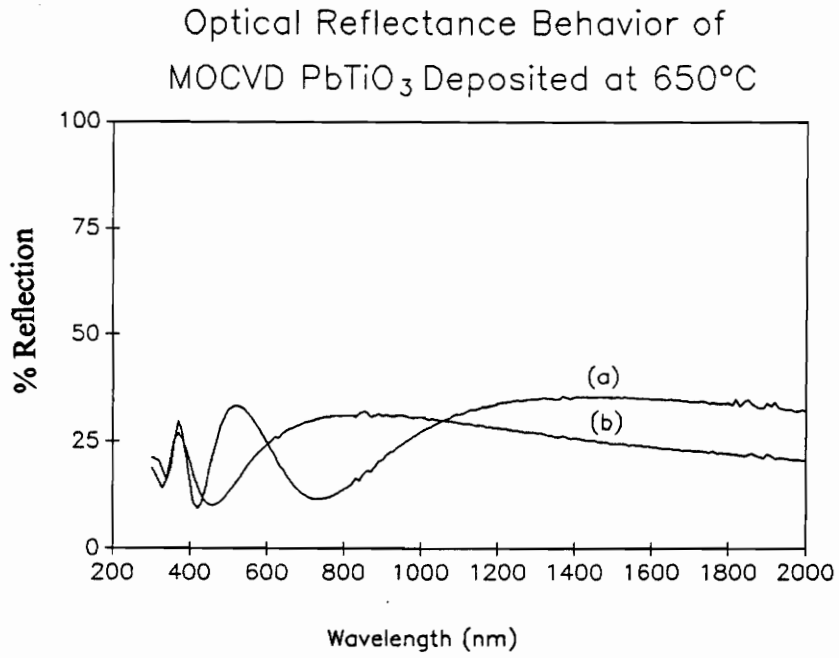

Figure 3.24: (a) Specular transmittance spectrum and (b) specular reflectance spectrum for $PbTiO_3$ deposited at 650 ^0C

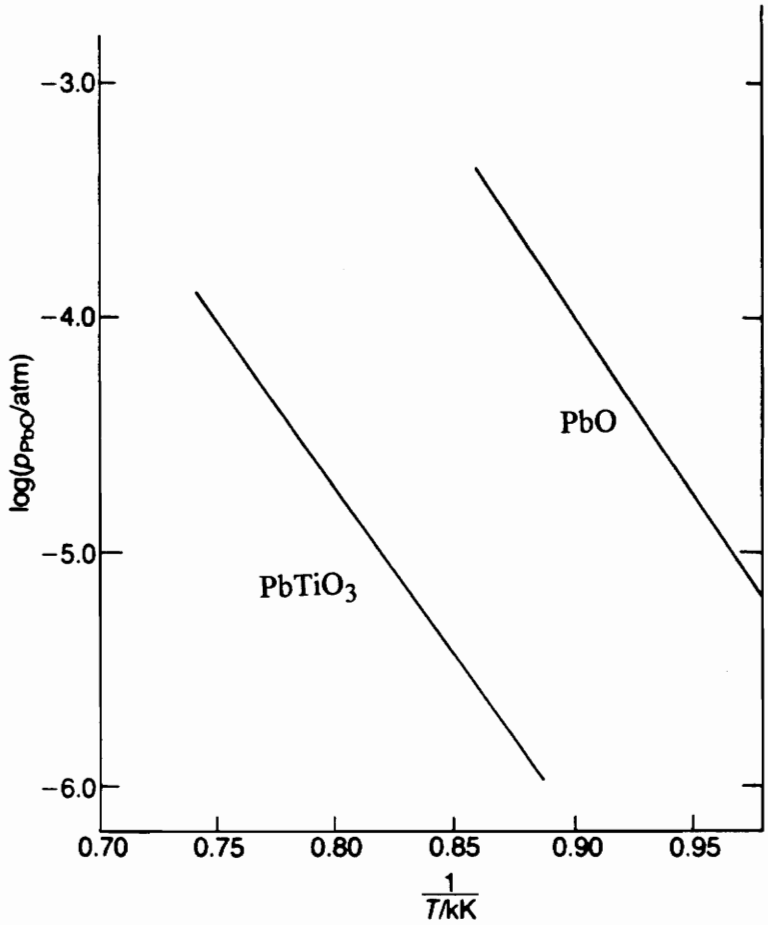

Figure 3.25: Vapor pressure of PbO over PbO and over $PbTiO_3$

as low as possible in order to reduce interdiffusion in the existing semiconductor films [2]. Consequently, there is sometimes an advantage to be gained if the films can be deposited at a relatively low temperature and then later annealed for a short time to obtain the desired structural properties. As an example, $PbTiO_3$ was deposited on Pt at the low temperature of 500 ^{0}C. The films were found to consist only of the perovskite phase but the topology was extremely rough with large hillocks, as can be observed in Figs. 3.26 and 3.27. After annealing different pieces of this sample in air for one hour at 500 ^{0}C and 600 ^{0}C, respectively, there is some evidence of a secondary growth that seems to be thermally activated as evidenced by the larger size of the secondary growth structures at 600 ^{0}C (see Fig. 3.27). XRD confirmed that the perovskite peaks had increased in intensity; thus, it seems likely that the secondary growth is actually the nucleation and growth of small perovskite grains in a matrix that is partially amorphous or microcrystalline. However, the topology is still very uneven due to the presence of the hillocks and so deposition temperatures as low as 500 ^{0}C should probably be avoided.

A post-deposition annealing was also performed on films that had been deposited on ruthenium oxide at 550 ^{0}C. These films were generally much smoother and fine grained and no hillocks were observed. However, after annealing these samples at 600 ^{0}C, the main structural differences that could be observed in the SEM micrograph (see Fig. 3.28) was that the grain size had increased tremendously, especially for the thickest films. Interestingly, the average grain size seen in the micrographs was found to be very close to the original film thickness which suggests that the film thickness may control the maximum amount of grain growth possible by requiring that the shape of the grains be approximately spherical; there is no driving force for grain growth beyond this point. Grain growth is generally undesirable from the standpoint of properties since smaller grained films tend to scatter less light as well as have superior electrical properties [2].

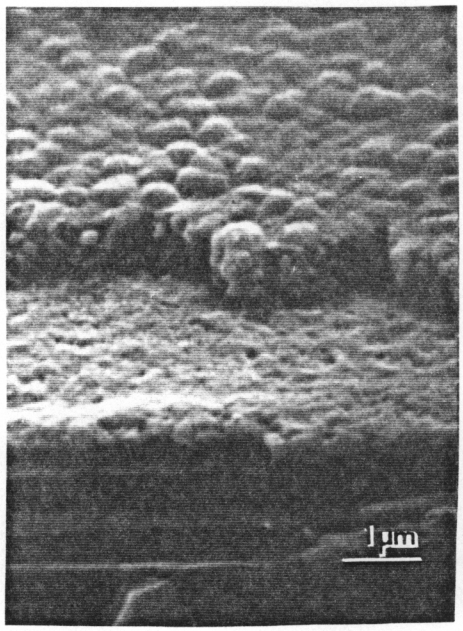

(a)

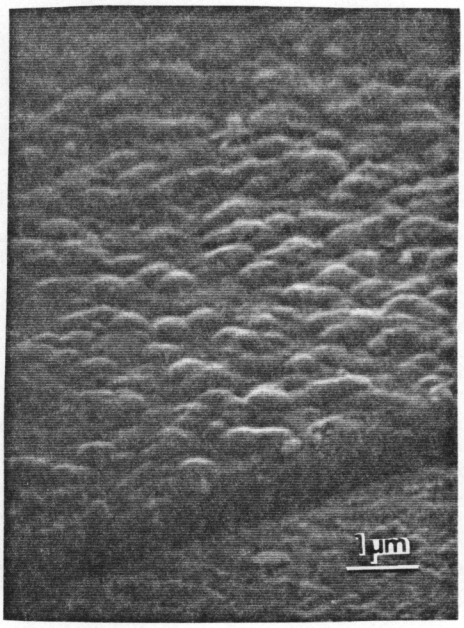

(b)

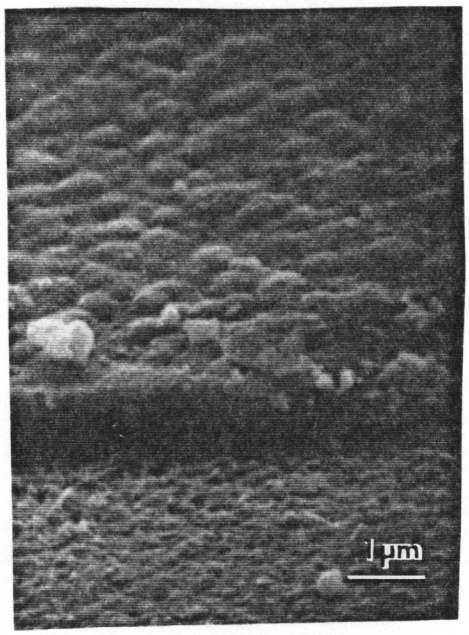

(c)

Figure 3.26: SEM micrographs of $PbTiO_3$ deposited on Pt at 500 ^{0}C in cross-section for (a) as-deposited film; (b) annealed at 500 ^{0}C for 1 hr. and (c) annealed at 600 ^{0}C for 1 hr.

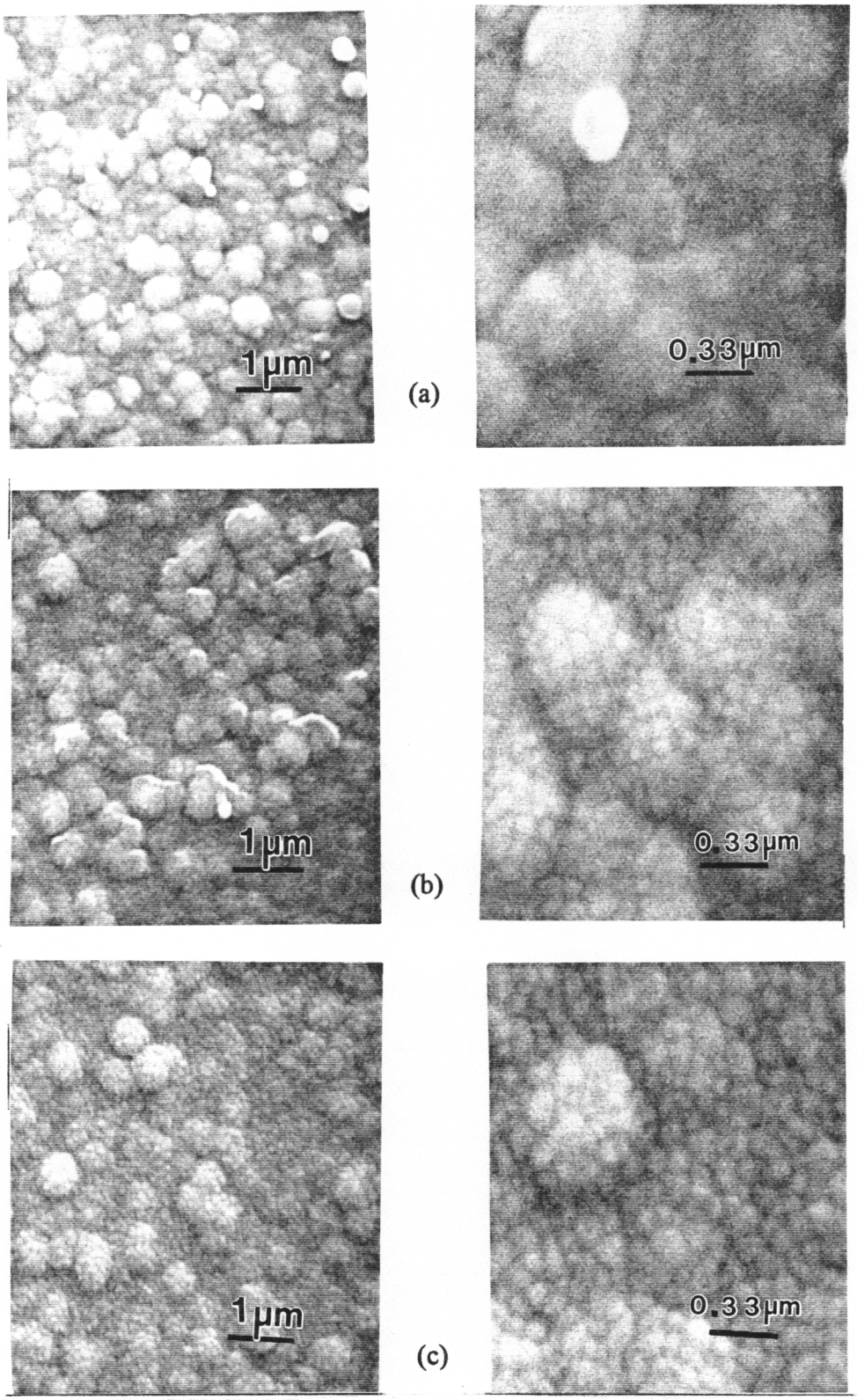

Figure 3.27: SEM micrographs of $PbTiO_3$ deposited on Pt at 500 ^{0}C for (a) as-deposited film; (b) annealed at 500 ^{0}C for 1 hr. and (c) annealed at 600 ^{0}C for 1 hr.

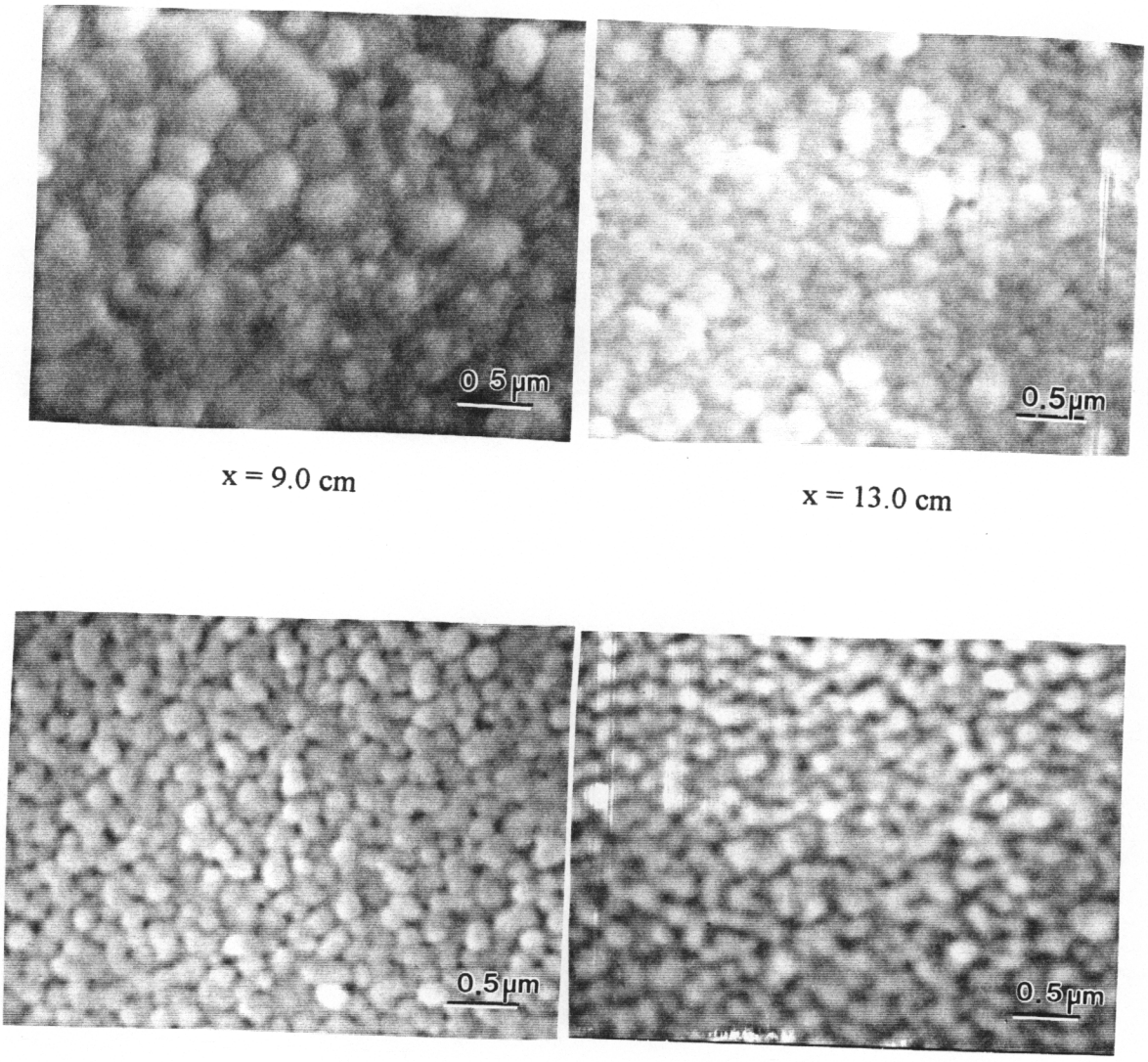

Figure 3.28: SEM micrographs of $PbTiO_3$ deposited on RuO_2 at 550 ^0C and annealed at 600 ^0C for 1 hr.

The effect of the composition and crystal structure before and after the heat treatment were also studied; the results from the composition study are given in Figs. 3.29 and 3.30, respectively. Each of these films was slightly Pb-rich before annealing (approx. 56%) but the amount of lead loss after the annealing process was only appreciable for those films which clearly showed excess PbO in the XRD pattern (see Figs. 3.31 and 3.32). This may be related to the fact that the PbO partial pressure over PbO is significantly higher than over $PbTiO_3$ (see Fig. 3.25). At 600 ^{0}C, the lead loss from $PbTiO_3$ is negligible, yet is quite significant for PbO. There is little change observed in the XRD patterns however, except that the peaks have intensified somewhat and what lead oxide remains has transformed to the high temperature massicot phase. The XRD patterns for a second set of samples with slightly different starting compositions are given in Figs. 3.32 and 3.33.

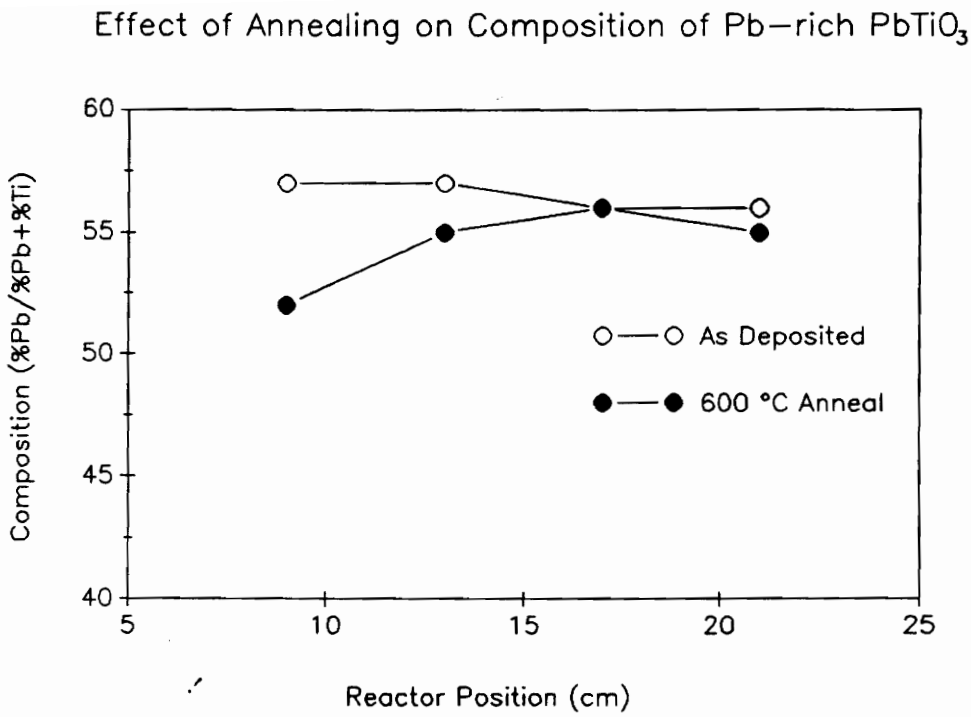

Figure 3.29: Effect of post-deposition annealing on composition of Pb-rich $PbTiO_3$

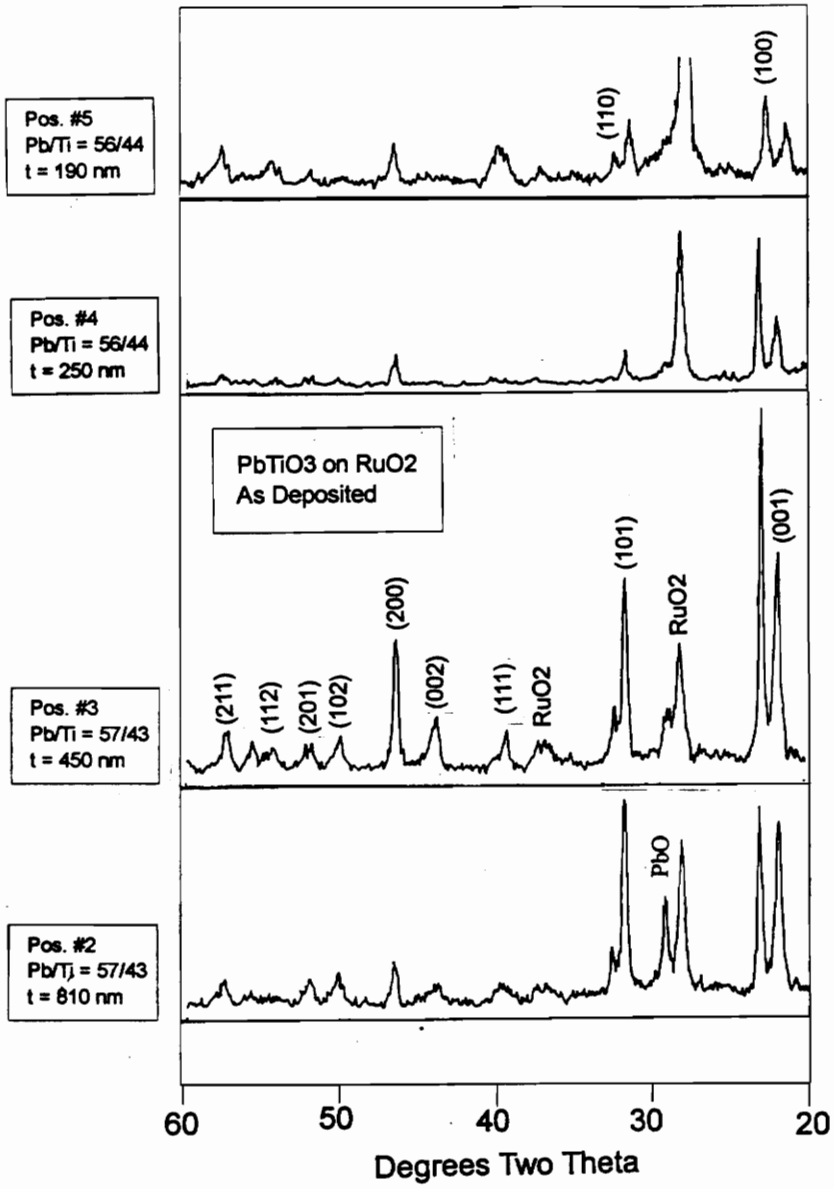

Figure 3.30: XRD of $PbTiO_3$ on RuO_2 at 550 ^0C (As Deposited)

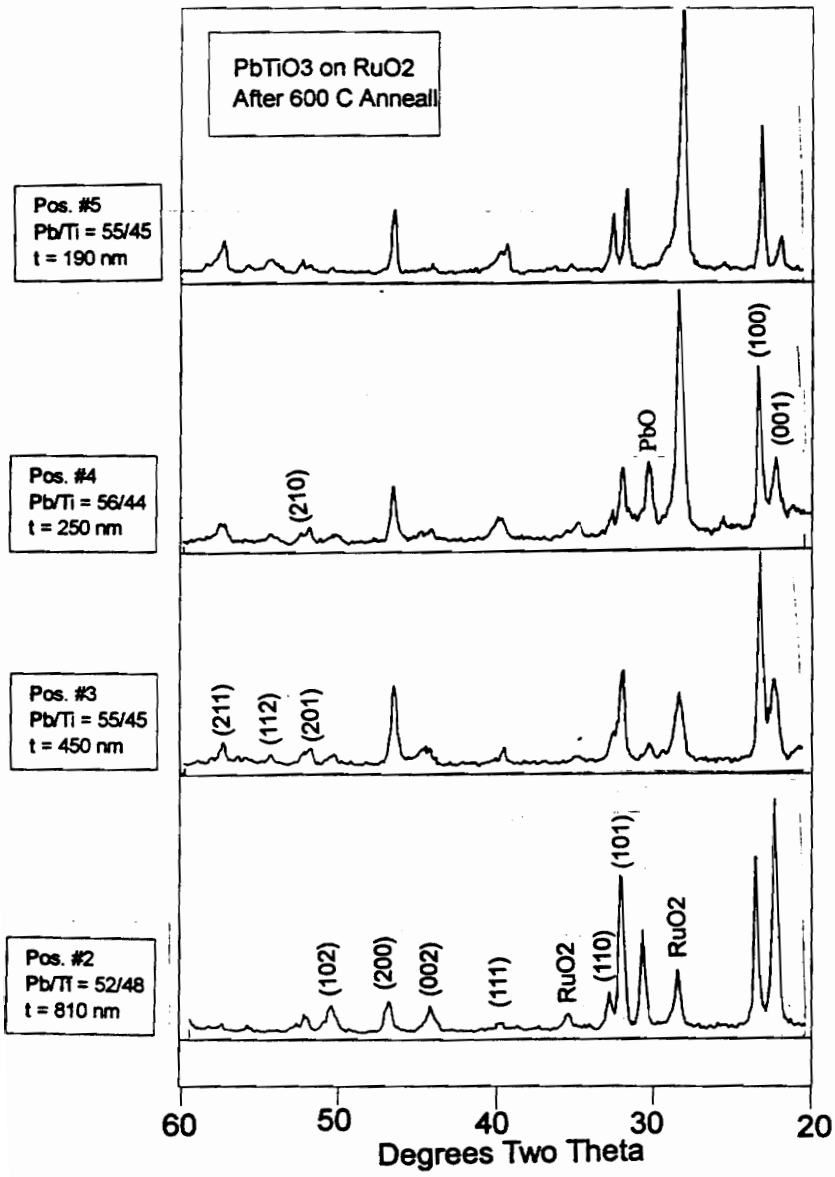

Figure 3.31: XRD of $PbTiO_3$ on RuO_2 at 550 ^{0}C (After 600 ^{0}C Anneal)

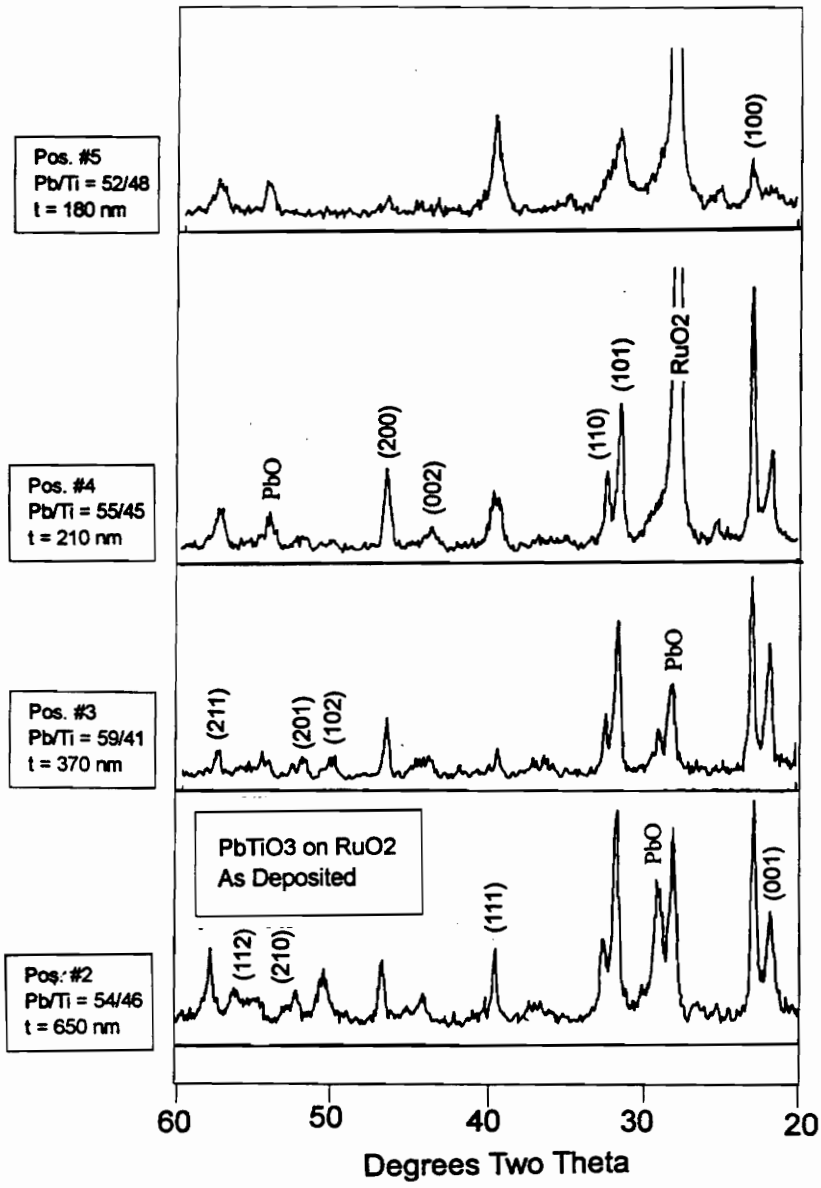

Figure 3.32: XRD of $PbTiO_3$ on RuO_2 at 550 ^0C (As Deposited)

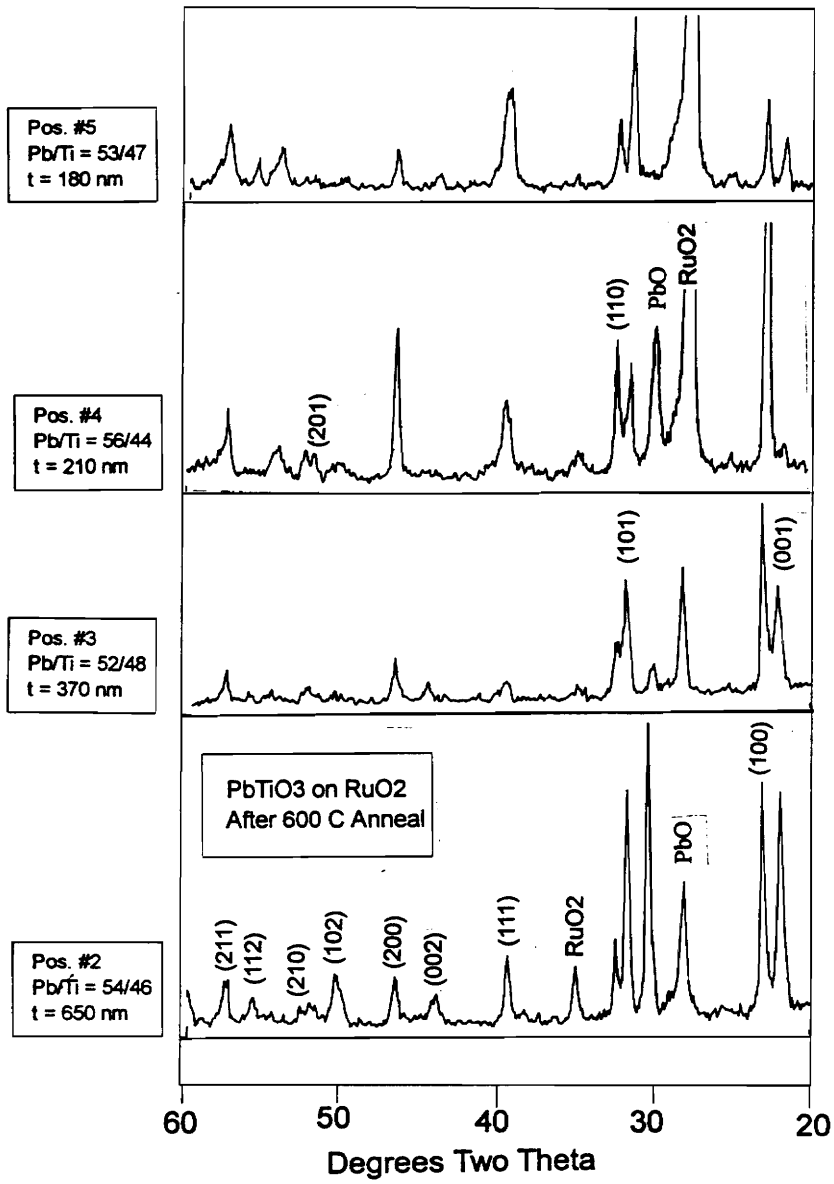

Figure 3.33: XRD of $PbTiO_3$ on RuO_2 at 550 ^0C (After 600 ^0C Anneal)

3.3.3 Stability of RuO_2-coated Substrates During the Deposition Process

While successful $PbTiO_3$ films were deposited on ruthenium oxide for temperatures as high as 550 ^{0}C, at 650 ^{0}C significant problems had occurred with the film peeling. Film peeling generally occurs when the stress generated in the film exceeds the strength of the material. Thus, the problem is to identify the cause of this stress. For some wafers, this was even a problem at low temperatures (550 ^{0}C). Several observations were made at this time: (1) the properties of substrates cut from the same wafer were generally consistent from one CVD run to the next; (2) film peeling was generally found to occur between the RuO_2 layer and the SiO_2 layer which could be confirmed by the metallic luster of the underside of the peels; (3) the XRD pattern of peeled and partially peeled films showed the existence of either ruthenium metal and no ruthenium oxide or a mixture of ruthenium metal and ruthenium oxide. Observation #3 was especially noteworthy because in no case was ruthenium metal observed for a film that had not peeled or cracked.

Based on the XRD patterns, it seems that the cause of the film stress is the chemical reduction of the ruthenium oxide electrode material. This is very surprising since ruthenium oxide is the stable phase at the temperature and oxygen partial pressures that are used in the MOCVD system [26, 27]. Ruthenium oxide can be transformed to ruthenium metal by two different reactions depending on the atmospheric conditions. In an oxidizing atmosphere, disproportionation is preferred which proceeds as follows [27]:

$$2RuO_2 \text{ --> } Ru + RuO_4 \text{ (gas)}$$

In a nonoxidizing atmosphere, reduction is preferred [27]:

$$RuO_2 \rightarrow Ru + O_2$$

It is not clear which reaction is operating in this case but for either case there is a large decrease in volume associated with each and consequently a large tensile stress that would be generated in the ruthenium/ruthenium oxide film.

To determine the influence of the CVD process on the reduction reaction, the CVD run was performed with the ruthenium oxide substrates as usual but without sending precursor vapors, and hence no film formation resulted. These substrates were completely untransformed after removing them from the reactor; this suggests that either the presence of the film or the reactive species in the CVD gas stream play a role in the ruthenium formation reaction. However, using a nitrogen atmosphere of 6 torr at 550 ^{0}C, it was possible to form the Ru even in the absence of precursor species or film.

3.3.3.1 Morphology Using Optical Microscopy

Optical microscopy was used at relatively low magnification to show the cracked and pock-marked surface of the lead titanate coated substrate that had been reduced during processing, seen in Fig. 3.34(a). In addition, the microstructure of the ruthenium oxide film which had been reduced in a nitrogen atmosphere is shown in Fig. 3.34(b). The micrographs show large fissures and cracks which are consistent with the theories mentioned above.

(a)

(b)

Figure 3.34: Optical micrograph (reflected polarized light) of (a) RuO_2 on (111) Si after being deposited with $PbTiO_3$ film at 550 ^0C and (b) RuO_2 on (111) Si after being annealed in 6 torr of N_2 at 600 ^0C

3.3.3.2 Influence of Silicon Substrate Crystal Orientation

There has been some noticeable difference in the peeling behavior between ruthenium oxide that had been deposited on (100) oriented silicon wafer and that deposited on (111) oriented silicon wafer, with the (100) Si seeming to be vastly superior. At first, it did not seem possible that the crystallographic orientation could have such an influence on the ruthenium oxide layer since they are separated by an amorphous layer of SiO_2. However, the difference may lie in the properties of the SiO_2 upon which the RuO_2 is deposited. Studies have shown that for the thermal oxidation of Si, the growth rate of the oxide is very sensitive to the silicon crystalline orientation with growth rate constants at similar temperatures larger by a factor of two for (111) compared to (100) [34]. As a result of the higher growth rate, it has also been shown that the oxide films are actually oxygen deficient SiO_{2-x}, the degree of nonstoichiometry depending on the growth conditions.

As a result of the oxygen deficiency in the SiO_2 layers it seems plausible that at high temperatures, oxygen might actually diffuse out of the RuO_2 lattice and into the SiO_2 in order to fully oxidize the SiO_2. Also, in the absence of a film, the ruthenium oxide should be able to reincorporate oxygen from the surroundings to maintain stoichiometry; if a film is grown on the surface of the ruthenium oxide, however, it may act as a diffusion barrier in preventing the incorporation of oxygen from the surroundings. This would explain the apparent disparity in behavior between the (111) and (100) orientations of Si as well as the reason why the existence of a film has an effect on the behavior.

3.3.4 Optical Properties Using UV-VIS-NIR Spectrometry

Optical properties were obtained from a $PbTiO_3$ sample prepared on sapphire at 500 ^{0}C. UV-VIS-NIR specular transmittance and specular reflectance spectra appear in Fig. 3.35. The transmission properties of the film revealed a highly specular, non-absorbing film as evidenced by the fact that the maxima in the interference fringes approach the transmitted intensities of the uncoated sapphire wafer at the higher wavelengths.

The dispersion relationship for the refractive index, n, and the behavior of the absorption coefficient with photon energy were both determined using the envelope method [2], as was the film thickness which was found to be 325 nm. The dispersion relationship and absorption behavior are given in Fig. 3.36. Using the curve for the absorption behavior with photon energy, it is possible to extrapolate the linear portion of the curve to zero absorption coefficient, α. The point at which this linear extrapolation crosses the x-axis determines the band gap of the film, which was found to be 3.67 eV, slightly larger than the 3.6 eV reported for the bulk solid [28]. For a wavelength of 632.8 nm, the refractive index was found to be 2.47 which is somewhat less than the literature value for the bulk of 2.67 [29]. Using an effective medium approximation, the film packing density was estimated to be about 89%. The effect medium technique is described in detail in Ref. 2 (Peng, 1992).

3.3.5 Ferroelectric Properties

The electrical properties of most films were generally found to be quite poor owing to very high film conductivities ($\rho = 10^6$ to 10^8 ohm cm); however, hysteresis

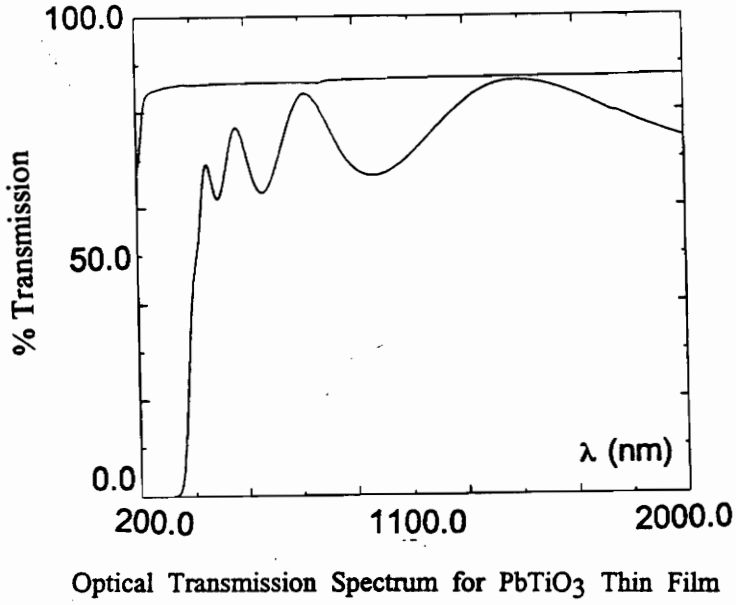

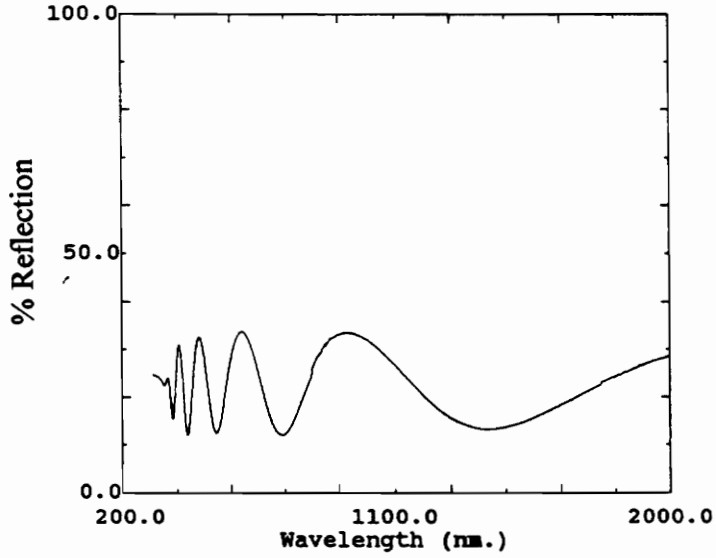

Figure 3.35: Optical transmission and reflectance spectra for $PbTiO_3$ film deposited at 550 ^0C on sapphire

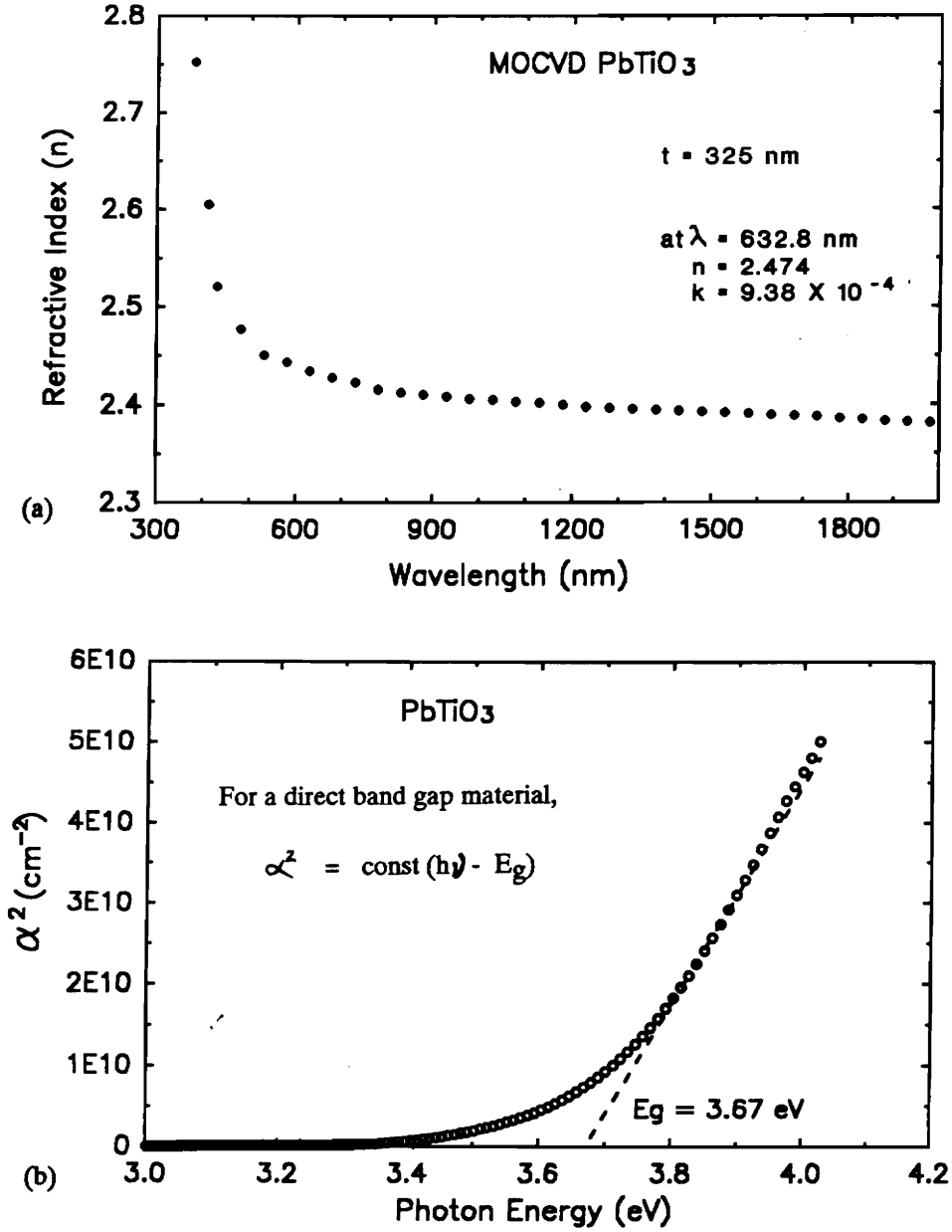

Figure 3.36: Optical properties of film determined from results in Fig. 3.35

behavior could sometimes be observed as shown in Fig. 3.37 with P_r = 1.1 μC/cm^2 and E_c = 45 kV/cm. The loop does not appear to be fully saturated, probably due to the conductivity. Lead titanate is notorious in the literature for being very conductive when synthesized in thin film form, whether the process used is MOCVD or other techniques including sol-gel and sputtering. MOCVD typically gives films with remnant polarizations less than 0.2 μC/cm^2. One likely cause is the large volume change for $PbTiO_3$ that occurs when ever the material passes through the Curie point (490 ^{0}C) and transforms between the non-ferroelectric cubic phase (high temperature) and the ferroelectric tetragonal phase (low temperature) which is difficult to avoid in most processes [8]. The volume change generates considerable stress and may cause microcracking. These microcracks may then be filled in by the conductive top electrode material and effectively "short circuit" the ferroelectric. The use of PZT can significantly reduce the volume change and anisotropy and this is part of the reason for the popularity of PZT [8]. MOCVD PZT films have been reported with excellent ferroelectric properties with P_r as high as 11 mC/cm^2 with E_c = 70 kV/cm [2]

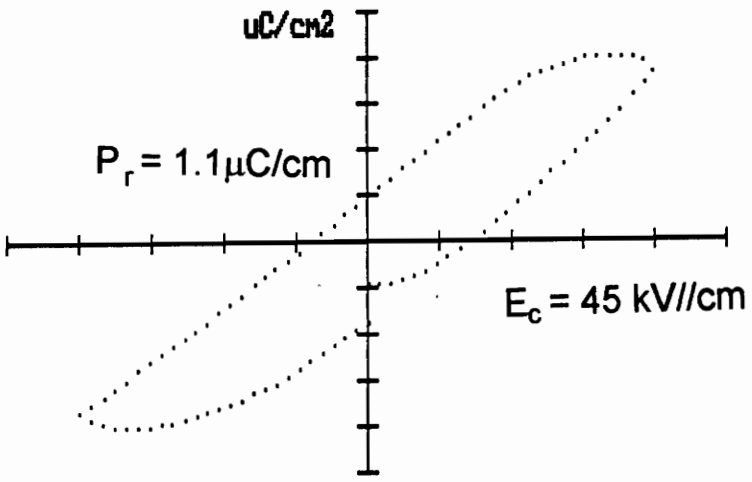

Figure 3.37: Ferroelectric hysteresis loop for $PbTiO_3$ on platinum deposited at 550 ^{0}C

3.4 Summary and Conclusions

Lead titanate was successfully deposited using a hot-walled MOCVD process with lead tetramethylheptadionate $Pb(thd)_2$ as the precursor for the lead source and titanium ethoxide $Ti(OEt)_4$ as the precursor for the titanium source. The films were deposited under a variety of conditions; the composition of the films was found to be extremely sensitive to the source gas composition at the low temperatures (550 ^{0}C and below), while at the higher temperatures (greater than 600 ^{0}C) it was found that the composition was extremely insensitive to experimental parameters. XRD was used to study the constituent phases in the material and was found to depend on the deposition rate as well as on the composition. The effects of post-deposition annealing on the composition, crystal structure and surface morphology was also studied. Lead loss was found to be negligible at 600 ^{0}C except for films which had excess PbO phase evident in the XRD pattern. Some problems were encountered with the peeling of the ruthenium oxide substrates in the MOCVD environment; this problem is caused by the formation of ruthenium metal from the ruthenium oxide and the large tensile stress associated with the transformation.

Appendix A: FORTRAN Code for MOCVD of PbO Simulation

```
C-----------------------------------------------------------------C
      SUBROUTINE SHAPE (XI,H,NPE)
      IMPLICIT REAL*8 (A-H,O-Z)
      COMMON/SHP/SF(2),GDSF(2),GJ
      DIMENSION DSF(2)
      SF(1) = 0.5*(1.0-XI)
      SF(2) = 0.5*(1.0+XI)
      DSF(1) = -0.5
      DSF(2) = 0.5
      GJ =  H*0.5
      DO 10 I = 1,NPE
10     GDSF(I) = DSF(I)/GJ
      RETURN
      END
C-----------------------------------------------------------------C
      SUBROUTINE STIFF
(NDF,NPE,IKNU,CK0,CK1,FLOW,DB,DK,RAD,AL,TREF)
      IMPLICIT REAL*8 (A-H,O-Z)
      COMMON/STF/ELK(2,2),ELF(2),ELX(2),ELT(2)
      COMMON/SHP/SF(2),GDSF(2),GJ
      DIMENSION GAUSS(4,4),WT(4,4)
      DATA GAUSS/4*0.0D0,-.57735027D0,.57735027D0,2*0.0D0,-.77459667D0,
     *  0.0D0,.77459667D0,0.0D0,-.86113631D0,
     *  -.33998104D0,.33998104D0,.86113631D0/
      DATA WT/2.0D0,3*0.0D0,2*1.0D0,2*0.0D0,.55555555D0,.88888888D0,
     *  .55555555D0,0.0D0,.34785485D0,2*.65214515D0,.34785485D0/
      RGAS1 = 1.987
      NN = NPE * NDF
      NGP = 4
      HELEM = ELX(NPE)-ELX(1)
      RAD1 = RAD
      DO 10 I=1,NN
      ELF(I) = 0.0
      DO 10 J=1,NN
10     ELK(I,J)=0.0
      DO 30 K=1,NGP
      X = GAUSS(K,NGP)
      CALL SHAPE(X,HELEM,NPE)
      CONST = GJ*WT(K,NGP)
```

```
      TT = 0.0
      DO 15 I=1,NPE
15     TT = TT + SF(I)*ELT(I)
      IF (IKNU .EQ. 0) THEN
        FU1 = DB*(TT**1.5)
      ELSE
        DB1 = DB*(TT**1.5)
        DK1 = DK*(TT**0.5)
        FU1 = DB1*DK1/(DB1+DK1)
      ENDIF
      AREA = 2.0/RAD1
      FLOW1 = FLOW*TT
      DO 20 I=1,NPE
      DO 20 J=1,NPE
      ELK(I,J) = ELK(I,J) + CONST*(FU1*GDSF(I)*GDSF(J) + FLOW1*AL*SF(I)*
     *         GDSF(J) + AREA*AL*AL*CK0*DEXP(-CK1/4.184/RGAS1/TT/TREF)
     *        *SF(I)*SF(J))/TT
20    CONTINUE
30    CONTINUE
      RETURN
      END
C-----------------------------------------------------------------------C
C     EQUATION SOLVER FOR NON-SYMMETRIC SYSTEM OF
C     EQUATIONS. SOLUTION IS STORED IN A(N,2*ITERM)
C-----------------------------------------------------------------------C
      SUBROUTINE SOLVE(A,NRMAX,NCMAX,N,ITERM)
      IMPLICIT REAL*8(A-H,O-Z)
      DIMENSION A(NRMAX,NCMAX)
      CERO = 1.D-8
      PARE = CERO**2
      NBND=2*ITERM
      NBM = NBND - 1
C     BEGINS ELIMINATION OF THE LOWER LEFT
      DO 1000 I=1, N
      IF (DABS(A(I,ITERM))  .LT.  CERO)  GO TO 410
      GO TO 430
  410 IF (DABS(A(I,ITERM))  .LT.  PARE)   GO TO 1600
  430 JLAST = MIN0(I+ITERM-1, N)
      L = ITERM + 1
      DO 500 J=I, JLAST
      L = L - 1
      IF (DABS(A(J,L))  .LT.  PARE)  GO TO 500
      B = A(J,L)
```

```
      DO 450 K=L, NBND
  450 A(J,K) = A(J,K) / B
      IF (I  .EQ.  N)  GO TO 1200
  500 CONTINUE
      L=0
      JFIRST = I + 1
      IF (JLAST  .LE.  I)  GO TO 1000
      DO 900 J= JFIRST, JLAST
      L=L+1
      IF (DABS(A(J,ITERM-L))  .LT.  PARE)  GO TO 900
      DO 600 K=ITERM, NBM
  600 A(J,K-L) = A(J-L,K) - A(J,K-L)
      A(J,NBND) = A(J-L,NBND) - A(J,NBND)
      IF (I  .GE.  N-ITERM+1)  GO TO 900
      DO 800 K=1, L
  800 A(J,NBND-K) = -A(J,NBND-K)
  900 CONTINUE
 1000 CONTINUE
 1200 L = ITERM - 1
      DO 1500 I=2, N
      DO 1500 J=1, L
      IF (N+1-I+J  .GT.  N)  GO TO 1500
      A(N+1-I,NBND) = A(N+1-I,NBND) - A(N+1-I+J,NBND)*A(N+1-I,ITERM+J)
 1500 CONTINUE
      RETURN
 1600 WRITE(*,1601)
 1601 FORMAT (' COMPUTATION STOPPED IN BNDEQ BECAUSE ZERO
APPEARED ON
     1MAIN DIAGONAL.   THE MATRIX FOLLOWS.')
      WRITE(*,1602)I,A(I,ITERM)
 1602 FORMAT(10X,I5,E12.4)
      STOP
      END
C-----------------------------------------------------------------C
C-----              MAIN PROGRAM                    -------C
C-----            HOT WALL CVD PROCESS                -------C
C-----------------------------------------------------------------C
      PROGRAM CVD
      IMPLICIT REAL*8 (A-H,O-Z)
      DIMENSION GK(100,4),IBDY(5),VBDY(5),X(100),NOD(100,2),
     * SOLU(100),TEMP(100),DEPO(100)
      COMMON/STF/ELK(2,2),ELF(2),ELX(2),ELT(2)
      DATA NRMAX,NCMAX,RGAS1,RGAS2/100,4,1.987,82.05/
```

```
      OPEN(7,FILE='CVD1.IN',STATUS='OLD')
      OPEN(8,FILE='CVD1.OUT',STATUS='OLD')
      PI = DACOS(-1.0D+0)
C
C--   BEGIN OF INPUT DATA
C--   UNIT: LENGTH-CM, TEMP-K, PRESSURE-TORR
C
      READ(7,*) NEM1
      NPE = 2
      NDF = 1
      IKNU = 1
      NBDY = 1
      IBDY(1) = 1
      NEM = NEM1 -1
      TREF = 298.0
      PREF = 1.0
      VBDY(1) = 1.0
      READ(7,*) WMAS1,WMAS2,DEN,RADIUS,ALENG
C-----------------------------------------------------------C
C--   DIFF: DIFFUSION CONSTANT OF PRECURSOR          --C
C--         (AT T=TREF, P=PREF)                      --C
C--   WMAS1: MOLECULAR WEIGHT OF PRECURSOR           --C
C--   WMAS2: MOLECULAR WEIGHT OF THIN SOLID FILMS    --C
C--   DEN: DENSITY OF THIN SOLID FILMS               --C
C--   RGAS1,RGAS2: GAS LAW CONSTANT (1.987 AND 82.05) --C
C--   TREF: REFERENCE TEMPEARTURE                    --C
C--   PREF: REFERENCE PRESSURE                       --C
C--   PTOT: TOTAL INLET PRESSURE                     --C
C--   PIN: INLET PRECURSOR PRESSURE                  --C
C--   FLOW: TOTAL INLET VOLUME RATE (SCCM)           --C
C--   CC1: ADJUSTING FACTOR FOR FLOW CALCULATION     --C
C--      (CONSTANT FOR ONE CVD REACTOR)              --C
C--   TIME: TOTAL DEPOSITION TIME (MIN)              --C
C--   RADIUS: RADIUS OF THE CVD REACTOR              --C
C--   ALENG: HEATING LENGTH OF THE CVD REACTOR       --C
C--   CK0: PRE-EXPONENTIAL FACTOR OF THE KINETIC DATA (CM/SEC)
C--   CK1: ACTIVATION ENERGY THE KINETIC DATA J/MOL  --C
C-----------------------------------------------------------C
      READ(7,*) (TEMP(I),I=1,NEM1)
      READ(7,*) DIFF,PTOT,PIN,FLOW,CC1,TIME
      READ(7,*) CK0,CK1
      DO 1 I=1,NEM1
1     TEMP(I) = TEMP(I) + 000.0
```

```
      FLOW = FLOW/PI/RADIUS/RADIUS/60.0
      DB = DIFF*PREF/PTOT
      DK = 9700.0*RADIUS*DSQRT(TREF/WMAS1)
      FLOW = FLOW*(760.0/PTOT)*CC1
      NHBW = NPE*NDF
      NNM = NEM*(NPE-1)+1
      NEQ = NNM*NDF
      NN = NPE*NDF
      NBW = 2*NHBW
      DO 10 I=1,NPE
10    NOD(1,I)=I
      DO 15 N=2,NEM
      DO 15 I=1,NPE
15    NOD(N,I) = NOD(N-1,I)+NPE-1
      DX=1.0/(NNM-1)
      DO 20 I=1,NNM
20    X(I)=DX*(I-1)
      DO 25 I=1,NEQ
      DO 25 J=1,NBW
25    GK(I,J)=0.0
      DO 45 N = 1, NEM
      DO 30 I=1,NPE
      NI = NOD(N,I)
      ELT(I) = TEMP(NI)/TREF
30    ELX(I)=X(NI)
      CALL STIFF
(NDF,NPE,IKNU,CK0,CK1,FLOW,DB,DK,RADIUS,ALENG,TREF)
C
C--   ASSEMBLE ELEMENT STIFFNESS MATRICES TO GET GLOBAL
STIFFNESS
C
      DO 40 I=1,NPE
      NR=(NOD(N,I)-1)*NDF
      DO 40 II=1,NDF
      NR=NR+1
      L=(I-1)*NDF+II
      GK(NR,NBW) = GK(NR,NBW) + ELF(L)
      DO 40 J=1,NPE
      NCL=(NOD(N,J)-1)*NDF
      DO 40 JJ=1,NDF
      M=(J-1)*NDF+JJ
      NC=NCL+JJ-NR+NHBW
      IF (NC) 40,40,35
```

```
35   GK(NR,NC)=GK(NR,NC)+ELK(L,M)
40   CONTINUE
45   CONTINUE
C
C---  IMPOSE ESSENTIAL BOUNDARY CONDITIONS
C
     DO 55 I=1,NBDY
     IB=IBDY(I)
     VB=VBDY(I)
     DO 50 J=1,NBW
50   GK(IB,J)=0.0
     GK(IB,NHBW)=1.0
55   GK(IB,NBW)=VB
     CALL SOLVE (GK,NRMAX,NCMAX,NEQ,NHBW)
C
C---  THE SOLUTION IS RETURNED IN THE LAST COLUMN OF GK
C
     DO 60 I=1,NEQ
60   SOLU(I)=GK(I,NBW)
C
C--   POST PROCESSING
C
     DO 70 I=1,NNM
     CTT = TEMP(I)
     CPP = SOLU(I)*PIN/760.0/RGAS2/CTT
70   DEPO(I)=CK0*DEXP(-
CK1/RGAS1/4.184/CTT)*CPP*(60.0E+07)*WMAS2/DEN
     WRITE(8,*) '-----------------------------------------------------'
     WRITE(8,*) 'UNIT OF DEPOSITION RATES AND THICKNESS:NM/MIN
AND NM'
     WRITE(8,*) '-----------------------------------------------------'
     WRITE(8,*) 'NO     POS      DEPO RATE        DEPO THICK'
     WRITE(8,100) (I,X(I)*ALENG,DEPO(I),DEPO(I)*TIME,I=1,NNM)
100  FORMAT(I3,2X,F6.2,2X,E12.3,5X,E12.3)
     CLOSE(7)
     CLOSE(8)
     STOP
     END
□
```

REFERENCES

1. M. Ohring, ***The Materials Science of Thin Films***, Academic Press, Inc., New York, 1992.

2. Peng, C. H., ***Optical Property Study and Metallorganic Chemical Vapor Deposition of Lead Zirconate Titanate (PZT)***, Ph. D. Thesis, Virginia Polytechnic Institute & State University, Blacksburg, VA, 1992.

3. G. H. Geiger, D. R. Poirier, ***Transport Phenomena in Metallurgy***, Addison-Wesley Pub. Co., Reading, Mass., 1973.

4. R. Clarke and J. E. Greene, "Reactively Evaporated Photoconductive PbO: Phase Transformations Induced by Water Vapor", ***Thin Solid Films***, **66**, 339 (1980).

5. Keezer, R. C., Bowman, D. L., and Becker, J. H., "Electrical and Optical Properties of Lead Oxide Single Crystals", ***Journal of Applied Physics***, **39** (4), 2062 (1968).

6. A. A. Chernov, ***Modern Crystallography III, Crystal Growth***, Springer Verlag, New York, 1984.

7. C. J. M. Rooymans and W. F. Th. Langenhoff, ***Journal of Crystal Growth***, "Hydrothermal Growth of Single Crystals and Phase Width of Tetragonal Lead Monoxide", **3** (4) (1968).

8. A. J. Moulson, ***Electroceramics***, Chapman & Hall, New York, 1990.

9. T. Nakagawa, J. Yamaguchi, M. Okuyama, and Y. Hamakawa, "Preparation of $PbTiO_3$ Ferroelectric Thin Film by Chemical Vapor Deposition", ***Japanese Journal of Applied Physics***, **21**, 655 (1982).

10. M. Okada, S. Takai, M. Amemiya, and K. Tominaga, "Preparation of c-Axis-Oriented $PbTiO_3$ Thin Films by MOCVD under Reduced Pressure", ***Japanese Journal of Applied Physics***, **28** (6), 1030 (1989).

11. B. S. Kwak, E. P. Boyd, and A. Erbil, "Metalorganic chemical vapor deposition of $PbTiO_3$ thin films", ***Applied Physics Letters***, **53** (18), 1702 (1988).

12. S. L. Swartz, D. A. Seifert, and G. T. Noel, "Characterization of MOCVD $PbTiO_3$ Thin Films", ***Ferroelectrics***, **93**, 37 (1989).

13. M. Shimizu, T. Katayama, M. Fujimoto, and T. Shiosaki, "Growth of $PbTiO_3$ films by photo-MOCVD", ***SPIE International Conference on Thin Film Physics and Applications***, **1519**, 122 (1991).

14. Y. Gao, G. Bai, K. L. Merkle, Y. Shi, H. L. M. Chang, Z. Shen, and D. J. Lam, "Microstructure of $PbTiO_3$ thin films deposited on (001) MgO by MOCVD", ***Journal of Materials Research***, **8** (1), 145 (1993).

15. R. C. Mehrotra, R. Bohra and D. P. Gaur, ***Metal Beta-Diketonates and Allied Derivatives***, Academic Press, Inc., London, 1978.

16. Nyman, May D., ***Synthesis and Characterization of Precursors for Chemical Vapor Deposition of Metal Oxide Thin Films***, M. S. Thesis, Virginia Polytechnic Institute & State University, Blacksburg, VA, 1992.

17. Schweitzer, et. al. "The Volatilities of Some Lead beta-Diketonates", ***Analytica Chemica Acta***, **43**, 332-334 (1968).

18. D. A. Porter, K. E. Easterling, ***Phase Transformations in Metals and Alloys***, Van Nostrand Reinhold Co., Ltd., 1981.

19. J. W. Matthews, C. J. Kircher, and R. E. Drake, "Oxides formed on the (111) Surface of Lead II: Red PbO or Litharge", ***Thin Solid Films***, **47**, 95 (1977).

20. M. T. Reetz, ***Organotitanium Reagents in Organic Synthesis***, Springer-Verlag, New York, 1986.

21. W. C. Hendricks, Jie Si, Chien H. Peng, Seshu B. Desu, "Metallorganic Chemical Vapor Deposition (MOCVD) of Titanium-Based Ferroelectric Thin Films", ***Proceedings of the 1992 MRS Conference***, 1992.

22. ***Dictionary of Organic Compounds***, 5 ed., Chapman and Hall, New York, 1982.

23. C. K. Kwok, D. P. Vijay, S. B. Desu, N. R. Parikh, and E. A. Hill, "Conducting Oxide Electrodes for Ferroelectric Thin Films", ***Proceedings of the 4th International Symposium on Integrated Ferroelectrics***, **IEEE**, 412 (1992).

24. I. K. Yoo, S. B. Desu, "Fatigue Modeling of Lead Zirconate Titanate (PZT) Thin FIlms", ***Materials Science and Engineering B***, **13**[4], 319-322 (1992).

25. M. De Keijser, G. J. M. Dormans, P. J. Van Veldhoven, and P. K. Larsen, "High Quality Lead Zirconate Titanate Films Grown by Organometallic Chemical Vapor Deposition", ***Proceedings of the 1992 IEEE ISIF Conference***, 243 (1992).

26. E. A. Seddon and K. R. Seddon, ***Chemistry of Ruthenium***, Elsevier, New York, 1984.

27. V. K. Tagirov, D. M. Chizhikov, E. K. Kazenas, and L. K. Shubochkin, "Thermal Dissociation of Ruthenium Dioxide and Rhodium Sesquioxide", ***Zhurnal Neorganicheskoi Khimii***, **20**, 1135 (1975).

28. Zametin, Phys. Stat. Sol. (B), **124**, 625 (1984).

29. P. D. Thacher, ***Applied Optics***, **16**, 3210 (1977).

30. C. H. Peng and S. B. Desu, "$Pb(Zr_xTi_{1-x})O_3$ Thin Films by Hot-Wall MOCVD", ***Proceedings of the 1992 IEEE ISIF Conference***

31. C. S. Hwang and H. J. Kim, "Deposition and Characterization of $PbTiO_3$ Thin Films on Silicon Wafers Using Metalorganic Sources", ***Journal of Electronic Materials***, **22** (7), 707 (1993).

32. K. Y. Hsieh, S. H. Rou, L. L. H. King, and A. I. Kingon, "Synthesis and Characterization of $PbTiO_3$ Thin Films Grown by Chemical Beam Deposition", ***Materials Research Symposium Proceedings***, **204**, 551 (1991).

33. V. G. Gavrilyachenko, R. I. Spinko, M. A. Martyenko, and E. G. Fesenko, "Spontaneous Polarization and Coercive Field of Lead Titanate", ***Soviet Physics - Solid State***, **12** (5), 1203 (1970).

34. C. L. Claeys, R. F. De Keersmaecker, and G. J. Declerck, "Technology and Kinetics of SiO_2 Growth", from ***The Si-SiO_2 System***, ed. P. Balk, Elsevier, New York, 1988.

35. H. Takeuchi, S. Jyomura, Y. Ishikawa and E. Yamamoto, "A 7.5 MHz Linear Array Ultrasonic Probe Using Modified $PbTiO_3$ Ceramics", ***Proceedings of the 1982 IEEE Ultrasonics Symposium***, IEEE, 849 (1982).

ADDITIONAL BIBLIOGRAPHY

T. Gareth and M. J. Goringe, ***Transmission Electron Microscopy of Materials***, John Wiley & Sons, Inc., New York, 1979.

B. G. Hyde and S. Anderson, S., ***Inorganic Crystal Structures***, John Wiley & Sons, New York, 1989.

W. D. Kingery, H. K. Bowen, D. R. Uhlmann, ***Introduction to Ceramics***, 2nd ed., John Wiley & Sons, New York, 1976.

B. D. Cullity, ***Elements of X-Ray Diffraction***, 2nd ed., Addison Wesley Publishing Company, Inc., Reading, Mass., 1978.

T. Ogawa, A. Senda, and T. Kasanami, "Controlling the Crystal Structure of Lead Titanate Thin Films", ***Japanese Journal of Applied Physics***, **30** (9B), 2145 (1991).

F. W. Ainger, C. J. Brierley, M. D. Hudson, C. Trundle, and R. W. Whatmore, "Ferroelectric Thin Films by Metal Organic Chemical Vapor Deposition", ***Materials Research Society Symposium***, **200**, 37 (1990).

R. A. Roy, K. F. Etzold, and J. J. Cuomo, "Ferroelectric Film Synthesis, Past and Present: A Select Review", ***Materials Research Society Symposium***, **200**, 141 (1990).

M. H. Francombe and S. V. Krishnaswamy, "Ferroelectric Films - Growth, Properties and Applications", ***Materials Research Society Symposium***, **200**, 179 (1990).

C. A. Paz de Araujo, L. D. McMillan, and J. F. Scott, "Processing of Ferroelectric Memories", ***Materials Research Society Symposium***, **230**, 277 (1992).

C. H. J. van den Brekel, "Characterization of Chemical Vapour-Deposition Processes, Part I", ***Philips Reserve Reports***, **32**, 118 (1977).

C. J. Brierley, C. Trundle, L. Considine, R. W. Whatmore, and F. W. Ainger, "The Growth of Ferroelectric Oxides by MOCVD", ***Ferroelectrics***, **91**, 181 (1989).

J. Lu, J. Wang and R. Raj, "Solution precursor chemical vapor deposition of titanium oxide thin films", ***Thin Solid Films***, **204**, L13-L17 (1991).

C. R. Kleijn, "On the modelling of transport phenomena in chemical vapour deposition and its use in reactor design and process optimization", ***Thin Solid Films***, **206**, 47 (1991).

VITA

Warren Charles Hendricks was born in Long Branch, New Jersey, the son of Warren Lee Hendricks and Carol Helen Hendricks in 1969. He grew up in Brick, New Jersey where he attended Brick Township High School and graduated in 1987. He then attended Virginia Polytechnic Institute & State University where he majored in Materials Engineering. During the summer following his junior year he participated in the Student Research Participant (SRP) program at Argonne National Laboratory where he studied the tribological behavior of sputter-coated ceramic materials. After receiving his Bachelor of Science at Virginia Tech in 1991, he remained there in the same department where he pursued a Master of Science degree in Materials Science and Engineering and studied the Metallorganic Chemical Vapor Deposition (MOCVD) process for the deposition of lead oxide (PbO) and lead titanate ($PbTiO_3$). He received his degree in September of 1993. His current plans include taking a short vacation before looking for a job in the thin films or electronics industry; future plans may include the pursuit of a Ph.D.